UNIVERSITY OF CALIFORNIA,
IRVINE

Bacterial Nitric Oxide Synthase Inhibition: Designer Drugs to Fight Bad Bugs

DISSERTATION

submitted in partial satisfaction of the requirements
for the degree of

DOCTOR OF PHILOSOPHY

in Biological Sciences

by

Matthew Chancellor Lewis

Dissertation Committee:
Chair: Professor Thomas Poulos
Associate Professor Naomi Morrissette
Assistant Professor Katrine Whiteson

2020

DEDICATION

To

Kith and Kin

‘Veit ek, at ek hekk vindga meiði á
nætr allar níu, geiri undaðr
ok gefinn Óðni,
sjalfr sjalfum mér,
á þeim meiði, er manngi veit
hvers af rótum renn.

Við hleifi mik
sældu né við hornigi;
nýsta ek niðr, nam ek upp rúnar,
æpandi nam, fell ek aftr þaðan.’

Odihn – Havamal 138-147

‘vae victis’
-Brennus

‘GOOD’
-Jocko

TABLE OF CONTENTS

LIST OF FIGURES

LIST OF TABLES

ACKNOWLEDGMENTS

I would like to express the deepest appreciation to my committee chair, Professor Thomas Poulos, who has the attitude and the mindset of a victor. He welcomed me into his lab and gave me the freedom to pursue research with the utmost zeal. Without his guidance and leadership this dissertation would not have been possible.

I would also like to thank the members, past and present, of the Poulos lab for helping me become a better scientist and person. To Dr. Scott Hollingsworth, thank you for introducing me to UCI and this wonderful space. To Dr. Jeffrey Holden, thank you for teaching me about bNOS and handing off the tools you so graciously built. To Dr. Huiying Li and Dr. Irina Sevrioukova I would like to offer my thanks for your patience and insight in protein purification and characterization.

To my collaborators at Northwestern University in the Silverman laboratory, I would like to thank you for providing the chemical tools necessary to continue this research. Without your efforts, this work would not have been possible.

I would like to thank my committee members, Associate Professor Naomi Morissette and Assistant Professor Katrine Whiteson, who offered guidance outside the realm of structural biology and helped me take this dissertation's work to another level.

I would like to thank my undergraduate research assistant Jenny Kim, without your herculean efforts, the H_2S project would not have made the tremendous progress that it did. I am so proud of you.

In addition, a very special thank you to Dr. Christine Schneider Lewis. No one could ask for a better partner in this thing we call life.

I would also like to thank the Archery Club at UC Irvine and the Brazilian Jiu Jitsu Club at UC Irvine for the friendship and physical outlet needed for a life outside of the lab.

VITAE

Matthew Lewis

Education

University of California, Irvine **2014- 2020**
Ph.D. Molecular Biology and Biochemistry Irvine, CA

Oregon State University **2006- 2011**
B.S. Biochemistry and Biophysics Corvallis, OR
B.S. Chemistry Corvallis, OR

Work and Research Experience

University of California, Irvine **August 2014 – Present**
Ph.D. Candidate **Irvine, CA**
Principal Investigator: Thomas Poulos

- Characterized isoform selective inhibitors for bacterial nitric oxide synthase (bNOS) using x-ray crystallographic and spectroscopic methods, including method troubleshooting and identification of protocol bottlenecks.
- Designed assays for pharmaceutical inhibitor efficacy and selectivity validation *in vitro* and *in vivo*
- Developed protocols for protein purification using affinity, size exclusion, and other chromatography methods.
- Trained undergraduates to comply and execute protocols while minimizing mistakes.
- Discussed outcomes and achievement of project processes and goals with trainees.
- Initiated and received approval from the Institutional Biosafety Committee to begin work with BSL-2 agent methicillin-resistant *Staphylococcus aureus* (MRSA) in our lab, including writing SOPs and risk management statements for agent use. This work includes working closely with EH&S about waste management and regulatory compliance.
- Validated synergistic pathway targets for combination therapy with current bNOS inhibitors

University of New Mexico **April 2014 – July 2014**
Research Assistant **Albuquerque, NM**
Principal Investigator: Pam Hall

- Conducted initial characterization of small molecule virulence inhibitors of BSL-2 agent methicillin-resistant *Staphylococcus aureus* (MRSA) in conjunction with antibiotic therapy in mice.
- Developed molecular biology techniques for testing efficacy of drug delivery using antibody tagged nanoparticles *in vitro* and *in vivo.*
- Tested *in vitro* efficacy of combination therapy for quorum sensing inhibition compounds and antibiotics.
- Purified recombinant proteins for binding studies

Biomedical Research Institute of New Mexico **May 2012 – Feb 2014**
Research Technician **Albuquerque, NM**
Principal Investigator: Hattie Gresham

- Tested efficacy of small molecule inhibition of virulence with BSL-2 agent methicillin-resistant *Staphylococcus aureus* (MRSA)
- Developed and tested models of efficacy in virulence inhibition of MRSA using mice. Trained in subcutaneous infection, I.P. dosing, cutaneous wound infection, necropsy, and use of the IVIS machine for fluorescence imaging.
- Processed tissues for bacterial burden and gene expression changes via qRT-PCR
- Propagated and maintained bacterial stocks. Extensive experience with bacterial dilution and plating techniques and standard microbiology techniques.
- Evaluated quorum sensing using flow cytometry and assessed growth potential of MRSA with quorum sensing inhibitors
- Served as Lab Safety Officer responsible for maintaining chemical inventory and MSDS, safety protocols, safety training documentation, and emergency equipment

Oregon State University **April 2010 – June 2011**
Undergraduate Research Assistant **Corvallis, OR**
Principal Investigator: P. Andrew Karplus

- Optimized analysis using the Protein Geometry Database and the Protein Data Bank
- Organized large datasets in Microsoft Excel into templates for use with machine learning algorithm "CUEVAS"
- Wrote Python and Shell scripts for CUEVAS optimization and data output organization
- Modeled structures using COOT and PyMOL software for publication

Skills and Software

- R Studio
- Bash
- Coot
- Pymol
- Phenix

Publications

Lewis, M. C., … Poulos, T. L. (2020). Selective Anti-MRSA Inhibitors Targeting Nitric Oxide Synthase (In preparation)

Holden, J. K., **Lewis, M. C.,** Cinelli, M. A., Abdullatif, Z., Pensa, A. V., Silverman, R. B., & Poulos, T. L. (2016). Targeting bacterial nitric oxide synthase with aminoquinoline-based inhibitors. *Biochemistry*, *55*(39), 5587-5594.

Holden, J. K., Dejam, D., **Lewis, M. C**., Huang, H., Kang, S., Jing, Q., ... & Poulos, T. L. (2015). Inhibitor bound crystal structures of bacterial nitric oxide synthase. *Biochemistry*, *54*(26), 4075-4082.

Hollingsworth, S. A., **Lewis, M. C.**, & Karplus, P. A. (2016). Beyond basins: φ, ψ preferences of a residue depend heavily on the φ, ψ values of its neighbors. *Protein Science*, *25*(9), 1757-1762.

Hollingsworth, S. A., **Lewis, M. C**., Berkholz, D. S., Wong, W. K., & Karplus, P. A. (2012). (φ, ψ) 2 motifs: a purely conformation-based fine-grained enumeration of protein parts at the two-residue level. *Journal of molecular biology*, *416*(1), 78-93.

Teaching and Mentoring

UCI Winter 2016 and 2017	Graduate Teaching Assistant- Undergraduate Biochemistry Lecture and Lab
OSU Fall-Winter 2009-2011	Undergraduate Teaching Assistant- Advanced Experimental Chemistry Lab
OSU Spring 2011	Undergraduate Teaching Assistant- Advanced Analytical Organic Chemistry Lab
Vidhi – (2018 – 2020)	Masters degree student who became a full time Ph.D. student
Jenny Kim (2017-2020)	Undergraduate lab assistant interested in pursuing M.D./Ph.D post graduation
Hilary Liu (2016-2017)	Undergraduate lab assistant. Currently laboratory medical technician.

ABSTRACT OF THE DISSERTATION

Bacterial Nitric Oxide Synthase Inhibition: Designer Drugs to Fight Bad Bugs

By

Matthew Chancellor Lewis

Doctor of Philosophy in Biological Sciences

University of California, Irvine, 2020

Professor Thomas Poulos, Chair

Antibiotic resistance of pathogenic bacteria is a growing problem of global concern. Current antibiotics target all bacteria indiscriminately and consequently wipe out good, beneficial bacteria as well as the bad, pathogenic ones. Bacterial Nitric Oxide Synthase (bNOS) has been identified as a suitable target to combat Methicilin Resistant *Staphylococcus aureus* (MRSA), a pathogen responsible for thousands of deaths each year in the United States alone. We report here the development of bNOS selective inhibitors based on an aminoquinolone chemical scaffold. These inhibitors were found to bind in both the active and pterin sites of bNOS, effectively reducing bacterial survival. In addition, we tested the limits of an NO selective chemical probe and began preliminary investigations of other potential drug targets for MRSA related to the NO pathway.

INTRODUCTION

Antibiotic resistance

Antibiotics, compounds that inhibit the growth of or kill microorganisms, are critically important medicines for treatment of bacterial infections. They are also widely used in agricultural settings to prevent infections and improve livestock productivity. Overuse and misuse of antibiotics has led to antibiotic resistance, which is a growing problem of international concern. As antibiotics have been used more frequently, and resistance has subsequently increased, development of new antibiotics has slowed dramatically. It is estimated that 23,000 deaths occur annually as a direct consequence of infection with pathogenic bacteria that are resistant to at least one antibiotic (CDC). In addition, resistant bacteria contribute to many additional deaths due to complications of bacterial infections. Bacteria gain resistance to antibiotics by adapting to specific selective pressures shaped by the biological target of the antibiotic. The physiological consequence of resistance-conferring genetic changes is evidenced by increasing amounts of antibiotic required to inhibit or kill bacteria. Ultimately, antibiotics are completely ineffective at concentrations far above those originally to inhibit or kill. In addition to their normal mode of function, antibiotics induce oxidative stress via increased reactive oxygen species (ROS) which can contribute to bacterial killing. This killing is thought to occur through oxidation of proteins, DNA, and lipids. As such, it has been hypothesized that inhibiting the ability of bacteria to neutralize ROS would increase antibiotic efficacy and enhance immune-mediated clearance by the host.

Resistance vs Tolerance vs Persistence

Drug activity is often defined by the minimum inhibitory concentration (MIC), and the minimum duration for killing (MDK) by a specific antibiotic. It has become clear that there is a need to distinguish between different survival strategies of bacteria with regards to antibiotic resistance. Therefore, researchers have proposed that researchers should distinguish ‘Resistance’, ‘Tolerance’, and ‘Persistence’ as separate states that the bacteria use to survive [1]. Antibiotic

resistance develops when bacteria are able to survive and grow in concentrations of an antibiotic that are lethal to the non-resistant strains. Tolerance refers to bacteria that are able to survive an exposure to the antibiotic that does not meet the MDK of the drug, but exceeds the MIC of the drug [2, 3].

Tolerance can develop through two separate mechanisms: lagging growth or slow growth. Lag phase growth happens during a transition in environments, such as occurs upon entering a host, or are adapting to a new niche. Lagging growth is characterized by a longer period of dormancy: metabolically inactive bacteria persist for a longer period of time than the duration of a hostile environment, with resumption of normal growth upon entering permissive environmental conditions [4]. This provides a protective effect, particularly against drugs that require actively replicating bacteria for activity. The mechanism by which the bacteria are able to enter this lagging state is currently unknown. As an example, if we look at the cell wall targeting beta lactams, we initially see that surviving bacteria are those that alter their growth rate to replicate slowly. This compensates for the effect of the drug which blocks peptidoglycan formation. Tolerance from slow growth is understood much in the same context as lag phase growth [5]. Tolerant bacteria exhibit continual metabolic activity, but at a significantly lowered rate, usually achieved by switching from aerobic respiration to fermentative growth. It has been hypothesized that tolerant and persistent subpopulations of bacteria eventually give rise to resistant strains. Several generations later, the subset of the bacterial population which harbor mutations in the genes for peptidoglycan linking enzymes are those who are most able to thrive in the presence of the beta lactam antibiotic, and this population eventually overgrows the remaining tolerant or persistent population. The new resistant population is now characterized by its insensitivity to antibiotic treatment.

Persistence is phenomenon characterized by a subset of a heterogeneous bacterial population which survives lethal antibiotic treatment. Persistent strains are distinct from resistant strains: when they are expanded again, most of the population is killed off again, with persistence

of subset of the population. Persistence is not associated with heritable genetic changes, leading us to wonder what phenomic changes underlie this mechanism of antibiotic evasion. Again, persisting bacteria are thought to be the ones that eventually give rise to resistant strains, particularly in cases where the patient is repeatedly prescribed antibiotics. In all cases, bacteria are able to slow their metabolism by temporarily inhibiting the electron transport chain and energy production.

Methicillin-resistant *Staph aureus*

Methicillin resistant *Staphylococcus aureus* (MRSA) are a type of gram-positive pathogenic bacteria that are one of the leading causes of death due to infectious disease in the United States. MRSA has both the ability to adapt to many diverse environments*f* without changing its genome and a high mutation rate. Its phenomic potential is immense and allows survival in the harsh environments of nutrient-deprived hard surfaces, in both high and low oxygen environments, and in environments of extreme ROS or acid stress. MRSA infiltrates into the host, can survive intracellularly when phagocytosed by immune cells, and evades capture and killing by adaptive immune cells. Colonization occurs when MRSA is able to persist in a particular body location where it eventually forms a biofilm. The bacteria continue to grow until a sufficient quorum is reached, at which point the bacteria virulence is upregulated. This increased virulence corresponds with a shift from biofilm formation and maintenance to motility and dissemination within the host.

MRSA response to host

MRSA has evolved several mechanisms to protect itself from the ROS stress of the host immune system. Most well-known is the phenotypic conversion to the Small Colony Variant (SCV)[6, 7]. SCVs are often characterized by slow growth rate, reshaped cell wall, and upregulation of genes involved with oxidative stress responses, arginine acquisition, iron uptake and iron regulation [8, 9]. SCVs have also been found to exist inside of endothelial cells, which

may confer a degree of protection from the immune system [10]. Interestingly, many SCVs are auxotrophic for menadione or hemin, which are precursor molecules required for the electron transport chain, suggesting that these may represent a potential opportunity for treatment.

One method by which pathogenic bacteria accomplish their intracellular survival is by sequestration of host metabolites that are necessary for mounting an immune response [11]. By directly competing with the host for the substrate, they both increase their own potential for growth and inhibit the host's efficacy in attacking the pathogen. Interestingly, intracellular survival within host immune cells may not be associated with survival against antibiotic treatment: the antibiotic concentration inside of the immune cell is not significantly lower than outside [12].

[6-12]

Nitric Oxide

Nitric Oxide (NO) is a small, neutral, lipophilic, diatomic free radical that reacts with metalloproteins and protein thiols. Through these reactions, NO acts dichotomously as both an important signaling molecule and a potent toxin. One method by which NO can be produced is through the enzyme nitric oxide synthase (NOS). NOS is a cys-ligated heme-containing P450-like enzyme that catalyzes the conversion of L-arginine to L-citrulline and the free radical nitric oxide (Scheme 1). It does so in two distinct reactions, with N-Hydroxy-L-Arginine as a stable intermediate product. The full reaction cycle requires 3 electrons from NADPH and 2 molecules of dioxygen. In addition to heme, NOS utilizes both flavin mononucleotide (FMN) and flavin adenine dinucleotide (FAD) cofactors as well as tetrahydrobiopterin (H_4B).

NO RXN Cycle

The first reaction cycle is very similar in nature to that of a classic P450 hydroxylation reaction(Figure I.1 Cycle 1): Step 1 begins with Arginine entering the active site(2.1), but the reaction itself begins with the reduction of Fe^{III} to Fe^{II} via an electron donated from the reductase domain(2.1-2.2). This enables the binding of dioxygen to the reduced heme, forming a ferrous

heme-dioxygen complex(2.3). To prevent iron-oxo decay and the release of peroxide, the BH_4 cofactor rapidly donates an electron to the heme-dioxygen complex, forming the peroxo-ferriheme(2.5). This iron-peroxo then accepts a proton to form a hydroperoxo-ferriheme(2.6). Subsequently, the O-O bond is heterolyticalaly cleaved, generating the catalytically active compound I and water(2.7). Compound I hydroxylates the substrate to form the intermediate substrate L – N Hydroxy Arginine (NOHA)(2.8). A second electron from NADPH reduces the BH4 radical back to its precatyltic state, NOHA is released, and the cycle is ready to begin again.

The second catalytic cycle does not appear to involve compound I, and the entire cycle not yet been conclusively experimentally determined. It is speculated to happen as shown in Figure I.2, NOS Cycle 2. The primary difference of the second catalytic step relative to the first is that it only involves the donation of a single electron from NADPH. It is thought that the BH4 radical is reduced by the NO- Ferriheme to generate NO in a productive cycle, though this has yet to be characterized.

NOS biological function

NO is a vitally important signaling molecule that serves a variety of functions. Mammals express three isoforms in different tissues to serve different purposes. In the brain, neuronal NOS (nNOS)-derived NO contributes to signaling between neurons via activation of soluble guanylyl cyclase. Although nNOS derived NO is involved with synaptic plasticity, dysregulation and overproduction of NO is associated with ischemia, neurogenesis inhibition, schizophrenia, depression, seizures, and Alzheimer's disease dementia [13]. In the circulatory system, endothelial NOS (eNOS)-derived NO regulates blood pressure by inducing activation of soluble guanylyl cyclase to regulate vasodilation. Dysregulation of eNOS can cause hypertension. Both eNOS and nNOS bind calmodulin (CAM) in a calcium-dependent manner and are therefore calcium-dependent for enzyme activity. Lastly, inducible NOS (iNOS) is expressed predominantly by macrophages and other immune cells. It is used in conjunction with the

oxidative burst to eradicate phagocytosed pathogens. In contrast to eNOS and nNOS, iNOS binds CAM independently of calcium concentration. These three nitric oxide synthases (nNOS, eNOS, and iNOS) are collectively known as mammalian NOS (mNOS). Dysregulation of individual isoforms can lead to pathological consequences. Nitric Oxide Synthase (NOS) is a homodimer of two long single polypeptide chains composed of both a heme-containing oxygenase domain, a CAM binding domain, and the flavin mononucleotide (FMN) and flavin Adenine dinucleotide (FAD) containing reductase domains.

NOS Structure

Structurally, NOS is a homodimer of two long single polypeptide chains composed of both a heme-containing oxygenase domain, a CAM binding domain, and the flavin mononucleotide (FMN) and flavin adenine dinucleotide (FAD) containing reductase domains (Figure I.3). The three mammalian isoforms are expressed in different tissues and serve different purposes: neuronal NOS (nNOS) is involved in signaling between neurons; endothelial NOS (eNOS) regulates vasodilation and helps control blood pressure; and inducible NOS (iNOS) is expressed predominantly by macrophages and other immune cells to destroy pathogenic invaders. nNOS, eNOS, and iNOS are collectively known as mammalian NOS (mNOS). Disregulation of each of these isoforms can lead to neurodegeneration, seizures, disrupted blood pressure, and unregulated inflammation.

bNOS Structure

The bacterial isoform (bNOS) is unique by comparison to the mammalian forms and consists solely of the heme-containing oxygenase domain, and therefore relies on alternative redox partners for obtaining electrons for enzymatic activity (Figure I.3). It also lacks the zinc binding domain, which is crucial for dimerization of the mNOS and helps to regulate their activity. bNOS also does not require either Ca^{2+}-calmodulin for function, even though both are necessary for mNOS function. The most notable difference in the active sit is an conserved Val -

> Ile mutation compared to the mNOS[14, 15]. It is thought to decrease the rate of NO release from the active site to help regulate NO production[16, 17].

NOS Enzymology

There are some interesting enzmyological differences between the isoforms of NOS, likely due to their distinct differences in biological function . eNOS binds O_2 with a K_m of approximately 4 uM, probably related to regulating blood pressure in low oxygen environment of moving blood from low O_2 tissue back to the oxygen rich environment of the lungs[18, 19]. The higher a K_m of nNOS and iNOS for O_2 is also probably related to their functions in more oxygen rich environments[19]. bNOS tends to have a higher K_m likely pertaining to its role in sensing a decreasing (but still not hypoxic) level of oxygen[20].

bNOS Function

Bacterial production of NO from bNOS exists in some gram-positive bacteria species and has previously been associated with antibiotic resistance and cytoprotection from ROS. Two nitric oxide producing species of particular interest to human health are *Staphylococcus aureus* and *Bacillus anthracis*. Methicillin-resistant *S. aureus* (MRSA) causes thousands of deaths per year and can be refractory to treatment[21]. In MRSA, NO has a number diverse roles. It is involved in the transition from aerobic to microaerobic environments, mediates the subsequent metabolic shift from oxidative phosphorylation to nitrate reduction, and helps maintaining cell membrane potential during this process. NO production from bNOS is also involved in heme sensing, an essential mechanism for regulating iron acquisition and avoiding harmful hydroxyl radical formation due to the Fenton reaction. Lastly, NO provides protection from neutrophil-mediated killing by antimicrobial peptides and the phago-lysosome pathway. Because of this defensive role, NO has been linked to antibiotic resistance, as several antibiotics act to induce ROS generation in addition to their normal mode of function. This link provides a potential drug target for inducing antibiotic susceptibility by targeting bNOS. Given the growing difficulty in

treating MRSA, inhibition of NO generation in bacteria is a promising treatment method in combination with current antibiotics for what might otherwise be life-threatening infections.

NO in bacteria has a role in both biofilm formation and in triggering motility and biofilm dispersion[22]. Low concentrations of NO mediate both quorum sensing and biofilm formation[23, 24]. High concentrations of host derived NO (from iNOS) have been shown to facilitate biofilm adhesion[24, 25]. Some of the signaling is derived from NO specific sensors like the H-NOX family of proteins[26], while others stem from the activation of c-di-GMP pathways[27, 28]. Others are competitors for O_2 sensing proteins like AirSR or SrrAB in MRSA[29, 30].

To therapeutically target NO production in bacteria without disrupting the essential functions of mammalian NO in the host requires creating a highly selective inhibitory molecule that takes advantage of the subtle structural differences between bNOS and the mammalian isoforms. In collaboration with the Silverman lab at Northwestern, the Poulos lab has been characterizing and developing a library of isoform selective NOS inhibitors. Using structure aided drug-design, we were able to identify chemical moieties that provide selectivity towards each isoform.

There are several key differences between the isoforms that we have sought to exploit. Primarily, the mammalian NOS isoforms have a regulatory zinc binding domain that exists between the dimer interface. (Figure I.4) In addition to keeping both halves of the dimer together, it also provides increased binding affinity for the BH4 cofactor by decreasing the amount of solvent exposed area relative to bNOS. The difference in binding affinity would indicate that an inhibitor designed to bind both the active site as well as the BH4 site would exhibit greater selectivity for bNOS over the mNOSes. In addition, a single valine residue in the mammalian forms is an isoleucine in the bacterial forms and has been hypothesized to provide differences in the second catalytic cycle of the enzyme. Previous screening in the Poulos lab by Dr. Jeffery Holden yielded two potent structural frameworks that function both as antimicrobials

and bNOS specific inhibitors. These two frameworks contain either an aminopyridine or an aminoquinolone head combined with an extended tail that reaches out beyond the active site. Using these scaffolds and additional rounds of structure-aided drug design, we continued optimization of inhibitor compounds to find several candidates that are highly selective and have high affinity for the bacterial isoform. These compounds were then evaluated for functional inhibition and screened for their ability to directly affect bacterial killing in association with antibiotics, ROS stress and intracellular survival within immune cells.

In this thesis, I present data to show that we developed bNOS selective inhibitors that preferentially inhibit bNOS. I tested the efficacy of the next generation of aminoquinolone based inhibitors for their ability to selectively inhibit bNOS and found their occupation in the pterin site of bNOS (Chapter 1). I helped develop and test a class of bNOS specific inhibitors that occupy both the active site and pterin site of bNOS (Chapter 2) and tried to develop a high throughput method of measuring *in situ* efficacy (Chapter 3). I solved the structure and opened the door for further investigation on two other potential drug targets for antibiotic resistant bacteria (Chapters 4 and 5). Together these studies provide a framework for the development and discovery of new drugs to combat pathogenic bacteria like methicillin resistant *Staphylococcus aureus* and *Bacillus anthracis*.

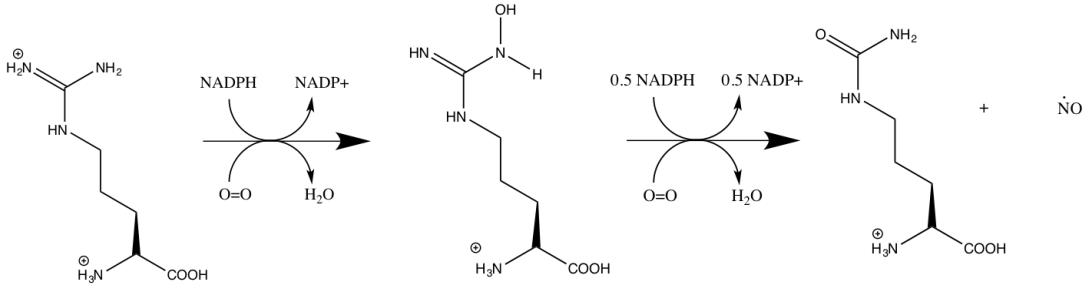

L-Arginine Nω-Hydroxy-L-Arginine L-Citrulline

Scheme I.1 – The production of NO via the two step oxidation of L-arginine to L-citrulline through the intermediate N^{ω}-Hydroxy-L-Arginine.

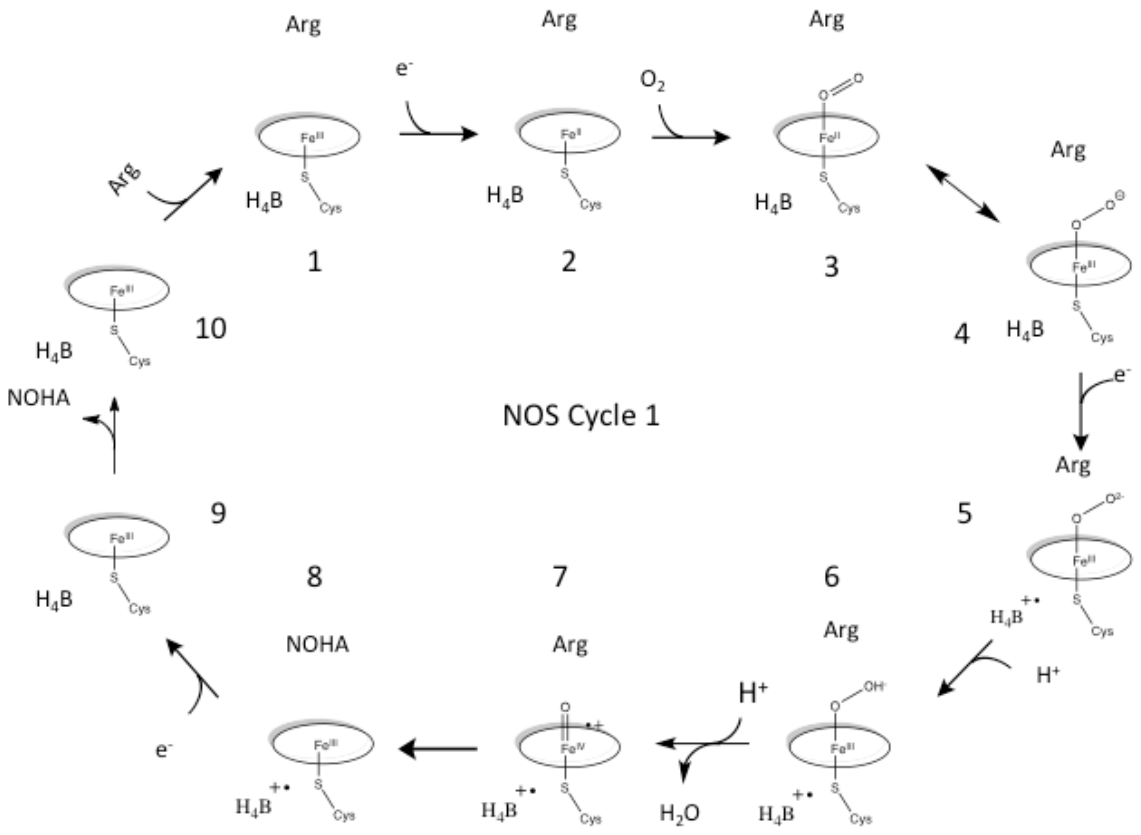

Figure I.1- The first reaction cycle catalyzed by NOS converting L-arginine to N-Hydroxy-L-Arginine.

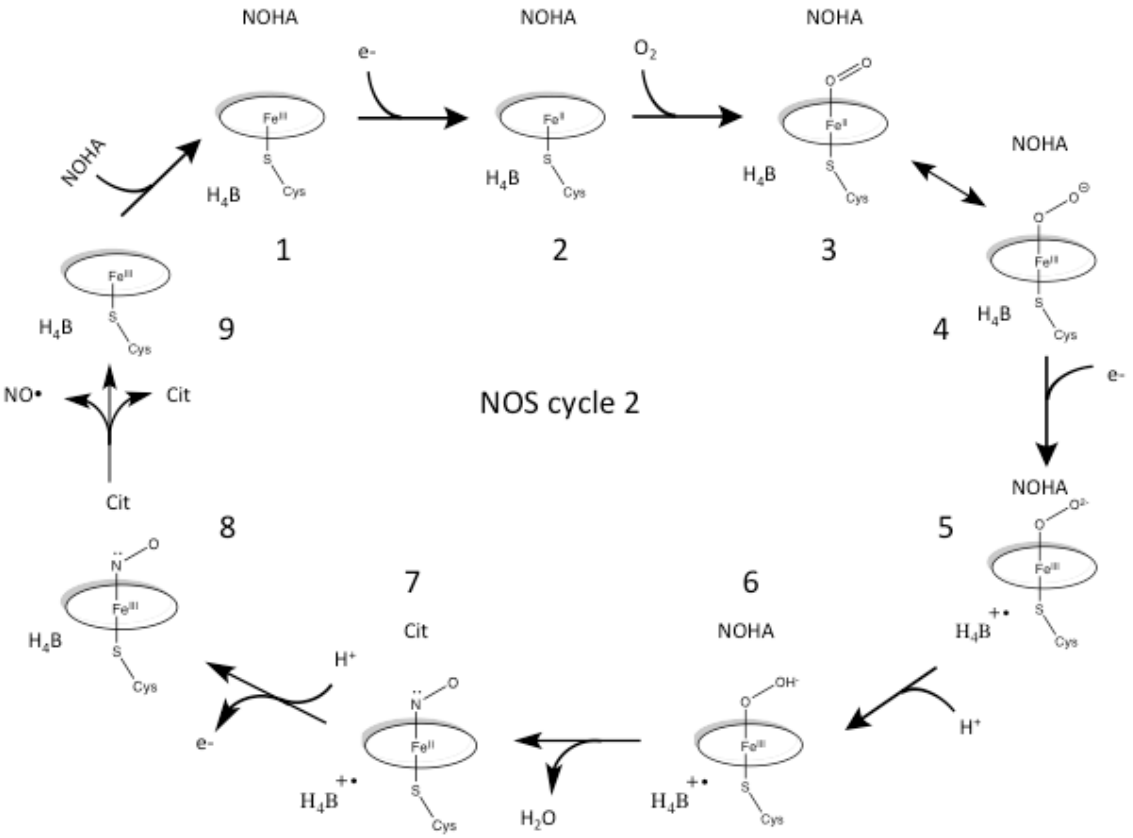

Figure I.2- The hypothetical second reaction cycle catalyzed by NOS converting N-Hydroxy-L-Arginine to citrulline and nitric oxide. Few of the intermediates of this cycle have been characterized.

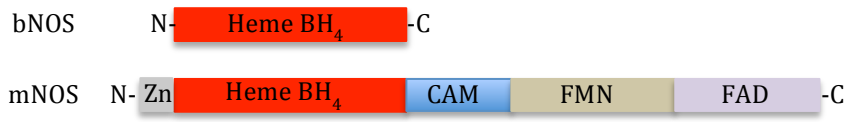

Figure I.3 Domain comparison of bNOS and mNOS

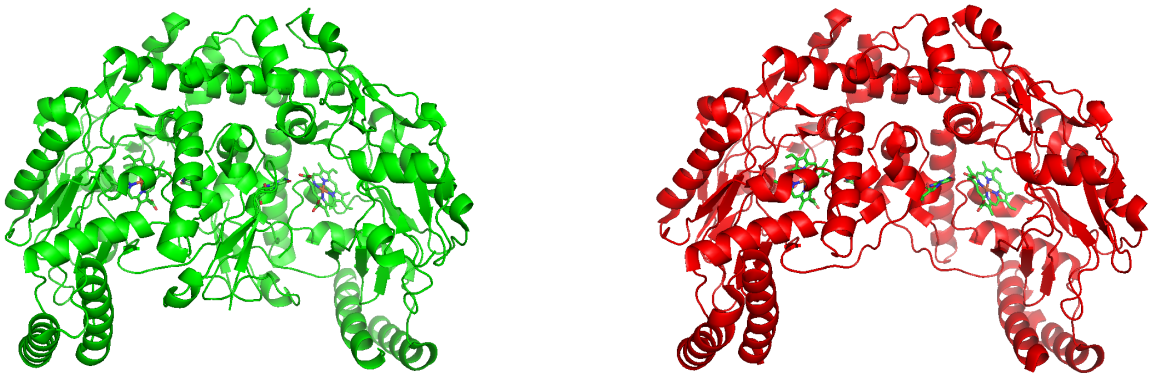

Figure I.4 Structural homology comparison of mNOS Heme and BH_4 domain and bNOS.

Reprinted with permission from: Jeffrey K. Holden, **Matthew C. Lewis**, Maris A. Cinelli, Ziad Abdullatif, Anthony V. Pensa, Richard B. Silverman, and Thomas L. Poulos
Biochemistry **2016** *55* (39), 5587-5594 DOI: 10.1021/acs.biochem.6b00786

Chapter 1

Targeting Bacterial Nitric Oxide Synthase with Aminoquinoline-Based Inhibitors

Author's Note: For this paper I purified bNOS, aided in some of the IC_{50} determinations, performed some of the spectral binding assays, and solved some of the structures.

Abstract

Nitric oxide (NO) is produced in Gram-positive pathogens *Bacillus anthracis* and *Staphylococcus aureus* by the bacterial isoform of nitric oxide synthase (NOS). Inhibition of bacterial nitric oxide synthase (bNOS) has been identified as a promising antibacterial strategy for targeting methicillin-resistant *Staphylocoocus aureus*[31]. One class of NOS inhibitors that demonstrates antimicrobial efficacy utilizes an aminoquinoline scaffold. Here we report on a variety of aminoquinolines that target the bacterial NOS active site, in part, by binding to a hydrophobic patch that is unique to bNOS. Through mutagenesis and crystallographic studies, our findings demonstrate that aminoquinolines are an excellent scaffold to further aid in the development of bNOS-specific inhibitors.

Introduction

Bacterial nitric oxide synthase (bNOS) shares many structural and enzymatic properties with the mammalian nitric oxide synthases (mNOS), neuronal NOS, inducible NOS, and endothelial NOS. Both bNOS and mNOS have heme-containing oxygenase domains that produce the free radical gas nitric oxide (NO) through a multi-electron transfer process. Biosynthesis of NO requires the substrate L-arginine (L-Arg), NADPH-derived electrons, and a reduced pterin group[32]. The active sites of all NOS isoforms are very similar and they all bind L-Arg directly over the heme, where a conserved L-Glu residue holds the L-Arg in place[33]. Despite many similarities between mNOS and bNOS, there are some significant differences. The mNOS isoforms are multi-domain proteins that transfer electrons from NADPH to the oxygenase domain *via* a separate reductase domain. Most bNOS enzymes, however, are composed of only the oxygenase domain, and thus depend on other redox partners for electron transfer[34]. The mNOS isoforms also contain an N-terminal Zn^{2+} binding motif that helps stabilize the dimer interface and binding of the pterin cofactor, tetrahydrobiopterin. In sharp contrast, bNOS lacks the Zn^{2+} binding motif and therefore has a more open dimer interface[35, 36] resulting in a larger pterin binding pocket[15, 37].

One of the many proposed roles of NO in bacteria is to help protect the bacteria from host cell or antibiotic-induced oxidative stress[38, 39], and in *Staphylococcus aureus* NO facilitates bacterial virulence*[40]*.Owing to the important role NO plays in methicillin-resistant *S. aureus* (MRSA), bNOS has become a promising therapeutic target. Previously, we demonstrated that NOS inhibitors improve the efficacy of the antimicrobial acriflavine[31, 41] and hydrogen peroxide-derived oxidative stress[33]. From our previous studies on NOS inhibition, we have identified several key active site differences that can be exploited for the design of bNOS specific inhibitors. Most notable is the “open” pterin-binding site that is unique to bNOS isoforms because of the missing Zn^{2+} binding motif[41] found in mNOS isoforms. Another notable difference is a hydrophobic patch at the distal face of the heme active site[42]; in bNOS this patch is composed

of a L-Ile residue, and in mNOS isoforms the analogous residue is a L-Val.

From a chemically diverse library of nNOS inhibitors, aminoquinoline-based inhibitors were identified for further development of a bNOS specific inhibitor targeting MRSA[31]. The aminoquinoline inhibitors were found to bind to the bNOS active site and exploit the hydrophobic patch contributed by the L-Ile residue (L-Val in mNOS) through van der Waals interactions. Since the aminoquinoline class of NOS inhibitors presents promising antimicrobial effects against MRSA, further characterization of aminoquinolines as bNOS inhibitors is necessary. Here we report on the characterization of 17 aminoquinoline-based bNOS inhibitors using binding, inhibition, and crystallographic studies. The inhibitors reported herein are shown in Figure 1.1.

Experimental Procedures

Molecular Biology

Bacillus subtilis NOS (bsNOS) DNA was previously cloned into a pET28a (Novagen) expression plasmid[41] with surface entropy reduction mutations E24A/E25A/E316A identified using the sERP server[43]. Introduction and expression/purification of bsNOS I218V was previously described[42]. Codon optimized DNA for *E. coli* expression of *Homo sapiens* inducible NOS (iNOS) was synthesized by Genewiz (South Plainfield, NJ) and cloned into pET28a (Novagen) using NdeI and XhoI as the restriction sites. The iNOS heme domain expression construct encoded residues Arg83 to Arg536. Active site mutation V352I was introduced to the heme domain expression construct by site directed mutagenesis using PfuTurbo (Agilent). An N-terminal His-tag calmodulin-expressing construct was prepared by PCR amplification of the calmodulin gene from a previous calmodulin expressing construct (a kind gift from Prof. Paul Ortiz de Montellano, UCSF) and cloned into pET28a (Novagen) using restriction sites NheI and HindIII, resulting in plasmid pJH114. Expression plasmid pJH114 was then digested with restriction enzymes XbaI and XhoI. The digested insert containing the calmodulin encoded gene was ligated into the XbaI and XhoI restriction sites of pET21a (Novagen) to produce Calmodulin

expression plasmid pJH115.

Expression and Purification

Both bsNOS and I218V bsNOS were overexpressed in *Escherichia coli* BL21(DE3) and isolated as previously described[41, 44]. Expression of the iNOS heme domain required co-expression with calmodulin. Hence, the iNOS heme domain-expressing plasmid was co-transformed with calmodulin expressing plasmid pJH115 into Overexpress C41(DE3) chemically competent *E. coli* cells (Sigma-Aldrich). The following morning an individual colony was inoculated into 5 mL of LB media supplemented with ampicillin and kanamycin at 50 ng/mL and 35 ng/mL, respectively. The starter culture was then aliquoted to 1 L TB media supplemented with 500 μM $CaCl_2$, 50 ng/mL ampicillin, and 35 ng/mL kanamycin. Following inoculation of the media, the culture was shaken overnight at 200 RPM and 30 °C. After this period, the culture reached OD_{600} > 2.0 and was induced by addition of 400 μM δ-aminolevulinic acid and 0.5 mM isopropyl β-D-1-thiogalactopyranoside. The bacterial cells were harvested by centrifugation and resuspended in lysis buffer composed of 40 mM Bis-Tris methane (pH 7.0), 200 mM NaCl, 1 mM $CaCl_2$, 4 mM L-Arg, 5 μM H_4B, 10% glycerol, and 5 mM imidazole. The bacterial cells were lysed using a microfluidics M-110L microfluidizer, and cell debris removed by centrifugation prior to loading on to a Ni^{2+}-nitrilotriacetate affinity column. The column was then washed with 10 CV of lysis buffer supplemented with 15 mM imidazole, and the targeted proteins were eluted with lysis buffer supplemented with 250 mM imidazole. The N-terminal His tag was removed by the protease thrombin (MP Biomedicals) at 4 °C overnight. Cleaved protein was resolved from the non-cleaved protein by Ni^{2+}-nitrilotriacetate affinity chromatography. The iNOS/calmodulin protein complex was further purified by Sepharose size-exclusion chromatography using a buffer composed of 40 mM HEPES (pH 7.6), 200 mM NaCl, 10% v/v glycerol, 10 μM H_4B, 0.5 mM imidazole, and 3 mM dithiothreitol.

Imidazole Displacement

The sample absorbance was monitored using a Cary 3E UV-visible spectrophotometer as inhibitors were titrated into a cuvette containing 50 mM Tris (pH 7.4), 1 mM imidazole, 100 μM dithiothreitol, 10 mM NaCl, and 2 μM of the corresponding NOS. The difference in the imidazole-bound low-spin state and the inhibitor-bound high-spin state was calculated as a function of inhibitor concentration, as previously annotated for bsNOS, bsNOS I218V, iNOS, and iNOS V352I[14]. From these data $K_{S,app}$, was calculated from the concentration of inhibitor required to transition 50% of the sample from low-spin to high-spin and was determined as previously reported[41] using a nonlinear regression analysis available in Sigmaplot version 10.0 (Systat Software, Inc., www.sigmaplot.com). The K_S for each ligand was then calculated from the $K_{S,app}$ as previously described[45] using the K_D of imidazole to bsNOS, bsNOS I218V, iNOS and iNOS 352I[14].

IC_{50} Determination.

Enzyme activity for bsNOS was measured using the previously described bBidomain construct.[44] The bBidomain enzyme is a fusion protein composed of bsNOS at the N-terminus, flavoprotein YkuN at the C-terminus, and a 30 amino acid peptide linker between the two proteins. In the presence of reductase YumC and NADPH a catalytic system is established and electrons are transferred to the bBidomain active site *via* the flavoproteins. Enzyme activity was measured by Griess reaction as previously described.[44] To calculate the IC_{50}, nitrite levels were measured at varying concentrations of inhibitor ranging from 0.1 μM to 200 μM for three separate replicates. The average percent inhibition was calculated for each inhibitor concentration evaluated and a curve was fit to the data in Sigmaplot version 10.0 (Systat Software, Inc., www.sigmaplot.com). The IC_{50} was extrapolated from the curve generated by Sigmaplot version 10.0.

Crystallization and Sample Preparation

Crystals of bsNOS and bsNOS I218V were obtained as previously described[41, 44]. Protein crystals were slowly cryoprotected in the presence of 2 mM H_4B and 25% v/v glycerol as previously reported[41]. Following cryoprotection, the crystals were soaked in the presence of 5-10 mM of the corresponding NOS inhibitor for 3-5 hours and then flash frozen using $N_2(l)$.

X-Ray Data Collection and Processing

X-ray diffraction data sets were collected on individual crystals at both the Advanced Light Source (Berkeley, CA) and the Stanford Synchrotron Radiation Light source (Palo Alto, CA). Data frames were indexed and integrated using either MOSFLM[46] or XDS[47]. The indexed data sets were scaled with Aimless[48] and some datasets with strong anisotropy were further scaled using the diffraction anisotropy server[49]. Structure factors were initially refined using Refmac[50] and PHENIX[51] was used for later rounds of refinement. The program COOT[52] was used to model inhibitor binding, and PyMOL (Version 1.5.0.4 Schrödinger, LLC.) was used to generate figures. Data collection and refinement statistics are provided in Table S1.

Chemical Synthesis of 1, 2, and 11

***tert*-Butyl (3-Hydroxybenzyl)(methyl)carbamate (19).** *Step 1.* Methylamine in THF (4.1 mL, 8.24 mmol) was diluted with $CHCl_3$ (10 mL), and aldehyde **18** (0.500 g, 4.12 mmol) was added in a solution of $CHCl_3$/MeOH (10:1, 5 mL). Anhydrous sodium sulfate (~2 g) was added, and the mixture was stirred rapidly under an argon atmosphere at room temp for 90 min. Glacial AcOH (50 μL) an additional anhydrous sodium sulfate (~1 g) was then added. The mixture was stirred for a total of 4 h, and the sodium sulfate was filtered from the mixture. The filtrate was concentrated, and the residue was diluted with MeOH (20 mL) and cooled to 0 ˚C. $NaBH_4$ (0.203 g, 5.36 mmol) was added, and the mixture was warmed to room temp and stirred for 20 min. The resulting mixture was concentrated, and the residue was partitioned between EtOAc and sat. aq.

$NaHCO_3$ (30 mL each). The layers were separated and the aqueous layer was extracted with EtOAc until no residual amine could be extracted (as measured by TLC). The organic layer was washed with sat. aq. NaCl (50 mL) and dried. Concentration afforded the intermediate secondary amine as an oil. *Step 2*. This amine was immediately diluted in THF (30 mL) and Boc_2O (0.900 g, 4.12 mmol) was added as a solution in minimal THF. The mixture was stirred at room temp for 3.5 h and then concentrated. The residue was partitioned between EtOAc and sat. aq. $NaHCO_3$ (30 mL each), the layers were separated, and the aqueous layer was extracted with EtOAc (3 x 30 mL). The combined organic layers were washed with H_2O and sat. aq. NaCl (50 mL each), dried over anhydrous sodium sulfate, and evaporated. The residue was purified by flash column chromatography (SiO_2), eluting with a gradient of hexanes to 35% EtOAc in hexanes to yield the product as a colorless syrup (0.756 g, 77%) that was used without further purification. ^{1}H-NMR (500 MHz; $CDCl_3$): δ 9.28 (br s, 1 H), 7.24-7.21 (m, 1 H), 7.09 (dd, J = 7.4, 1.6 Hz, 1 H), 6.94 (d, J = 8.1 Hz, 1 H), 6.81 (t, J = 7.4 Hz, 1 H), 4.31 (s, 2 H), 2.88 (s, 3 H), 1.48 (s, 9 H); ^{13}C-NMR (126 MHz; $CDCl_3$): δ 156.4, 131.4, 130.1, 122.6, 119.3, 117.7, 81.6, 49.6, 34.1, 28.5.

7-[(2-((Methylamino)methyl)phenoxy)methyl]quinolin-2-amine Dihydrochloride (11). NaH (60% suspension in mineral oil, 0.011 g, 0.27 mmol) was diluted with anhydrous DMF (1.5 mL) and cooled to 0 ˚C under an argon atmosphere. A solution of phenol **19** (0.064 g, 0.27 mmol) in anhydrous DMF (1.5 mL) was added slowly to the suspension and stirred at 0 ˚C for 20 min, followed by addition of bromide **20 (**see**[53]**; 0.075 g, 0.27 mmol) in anhydrous DMF. The reaction mixture was stirred at 0 ˚C for 1 h and was then quenched by addition of a 1:1 sat. aq. NaCl/H_2O (~15 mL). The mixture was extracted with EtOAc (3 x 20 mL), and the organic phase was washed with 5% aq. NaCl (3 x 50 mL) and sat aq. NaCl (50 mL). The organic layer was dried over anhydrous sodium sulfate, concentrated, and purified by flash column chromatography (SiO_2), eluting with a gradient of 5% EtOAc in CH_2Cl_2 to 35% EtOAc in CH_2Cl_2 to yield acetamide **21** as an off-white foam (0.099 g, 85%), which was immediately deprotected.

Compound **21** was diluted with anhydrous MeOH (10 mL), and anhydrous K_2CO_3 (0.063 g, 0.457 mmol) was added. The mixture was heated at reflux for 2.5 h, cooled, and concentrated. The resulting residue was partitioned between EtOAc and 1:1 H_2O/sat. aq. NaCl, and the aqueous layer was extracted with EtOAc (3 x 20 mL). The organic layers were washed with sat. aq. NaCl (40 mL), dried over anhydrous sodium sulfate, and concentrated. EtOAc (2 mL) was added to the residue, followed by hexanes (15 mL). The mixture was heated to boiling, and sonicated vigorously until an off-white solid precipitate formed, which was collected by filtration and washed with hexanes. This free aminoquinoline was diluted in 10:1 ether/MeOH, and filtered to remove any particulate matter. To the filtered solution was added methanolic HCl (3 M, 1 mL), and the mixture was stirred at room temperature overnight. The resulting precipitate was collected, diluted in hot MeOH (1 mL), and ether (10 mL) was added, giving **11** as a white flocculent solid (0.063 g, 75%) after washing with ether: mp 284-286 ˚C. ^{1}H-NMR (500 MHz; DMSO-d_6): δ 14.50 (br s, 1 H), 9.30 (br s, 1 H), 8.99 (br s, 2 H), 8.37 (d, J = 9.2 Hz, 2 H), 8.30 (br s, 1 H), 7.95 (d, J = 8.2 Hz, 1 H), 7.91 (s, 1 H), 7.60 (d, J = 7.6 Hz, 1 H), 7.49 (dd, J = 7.5, 1.6 Hz, 1 H), 7.43-7.39 (m, 1 H), 7.17 (d, J = 8.1 Hz, 1 H), 7.09 (d, J = 9.3 Hz, 1 H), 7.05 (td, J = 7.4, 0.7 Hz, 1 H), 5.41 (s, 2 H), 4.21 (t, J = 5.5 Hz, 2 H), 2.62 (t, J = 5.2 Hz, 3 H); ^{13}C-NMR (126 MHz; DMSO-d_6): δ 156.1, 154.4, 142.8, 142.0, 131.4, 130.8, 128.9, 123.6, 121.0, 120.3, 120.2, 115.1, 113.7, 112.5, 68.6, 46.4, 32.6; one of the aminoquinoline carbons is not visible due to baseline broadening. ESIMS *m/z* (rel. intensity) 294 (MH^+, 100); HRMS calcd for $C_{18}H_{20}N_3O^+$: 294.1601; found, 294.1612. HPLC purity: 100%.

Quinolin-2-amine Hydrochloride (1). A sealable vial was charged with 2-chloroquinoline (**22**, 0.244 g, 1.5 mmol), $Pd_2(dba)_3$ (13 mg), and DavePhos (13 mg). Anhydrous dioxane (1.1 mL) and LHMDS (1 M in THF, 3.4 mL, 3.4 mmol) were added, the solution was purged with argon, and the vial was sealed. The mixture was heated to 100 ˚C for 20 h, and then cooled and poured into 6 N HCl (20 mL). The solution was washed with EtOAc (20 mL), and the EtOAc layer was

extracted with 6 N HCl (3 x 20 mL). The various aqueous layers were washed with EtOAc (2 x 30 mL). The EtOAc washes were discarded, and the combined aqueous phase was basified with NaOH to pH 12. The suspension was extracted with EtOAc (3 x 30 mL), and the organic layers were washed with 5% aq. NaCl and sat. aq. NaCl (50 mL each), dried over anhydrous sodium sulfate, and concentrated. The residue was purified by flash column chromatography (SiO_2), eluting with a gradient of EtOAc to 2% MeOH in EtOAc to yield a white solid after dissolving in EtOAc (5 mL) and precipitating with hexanes (50 mL). The collected solid was diluted with dry ether (8 mL) and treated with methanolic HCl (3 M, 1.5 mL, 4.5 mmol), upon which a colorless solid precipitated, which was collected by filtration and dried to afford **1** (0.150 g, 70%): mp 110-111 ˚C (softens, possibly free-bases); 120-122 ˚C (melts) (see[54] mp: 222-223 ˚C (HCl salt); 126-127 ˚C (free-base)). ^{1}H-NMR (500 MHz; DMSO-d_6): δ 14.28 (s, 1 H), 9.14 (s, 1 H), 8.38 (d, J = 9.3 Hz, 1 H), 8.21 (br s, 1 H), 7.92 (dd, J = 8.0, 1.0 Hz, 1 H), 7.77 (td, J = 7.7, 1.3 Hz, 1 H), 7.71 (d, J = 8.2 Hz, 1 H), 7.50-7.47 (m, 1 H), 7.12 (d, J = 9.3 Hz, 1 H); ^{13}C-NMR (126 MHz; DMSO-d_6): δ 154.3, 143.0, 135.7, 132.5, 128.8, 124.9, 120.9, 117.2, 113.8. ESIMS *m/z* (rel. intensity) 145 (MH^+, 100). HPLC purity: 99.6%.

4-Methylquinolin-2-amine Hydrochloride (2). A mixture of 2-chlorolepidine (**23**) (0.300 g, 1.69 mmol), K_2CO_3 (1.17 g, 8.45 mmol), and dry acetamide (8.0 g, 135 mmol) was heated to 240 ˚C for 2 h, during which time a yellow color formed. The solution was then cooled and poured into H_2O (50 mL). The suspension was extracted with EtOAc (3 x 50 mL), and the organic layer was washed with H_2O (3 x 50 mL) and sat. aq. NaCl (50 mL) and then dried over anhydrous sodium sulfate. The solution was concentrated and the residue was purified by flash column chromatography (SiO_2), eluting with a gradient of EtOAc to 2% MeOH in EtOAc to yield a yellow solid after washing with 2% EtOAc in hexanes. The solid was diluted with dry ether (8 mL) and treated with methanolic HCl (3 M, 1.5 mL, 4.5 mmol), precipitating a colorless solid. An analytically pure sample was produced by preparative HPLC, using an Agilent Infinity 1200

HPLC pump with MS SQ 6130 detector, with a Phenomenex Gemini 5μ C18 150 x 21.2 mm column, eluting with a gradient of 97% H_2O (+ 0.1% formic acid) + 3% MeCN (+ 0.1% formic acid) to 40% H_2O (+ 0.1% formic acid) + 60% MeCN (+ 0.1% formic acid) over 20 min, at a flow rate of 20 mL/min. The product was obtained as a white solid (87 mg, 33%): mp 199-201 ˚C (see[55] mp 201-202 ˚C)); ^{1}H-NMR (500 MHz; DMSO-d_6): δ 14.04 (s, 1 H), 8.94 (br s, 1 H), 8.30 (br s, 1 H), 8.00 (dd, J = 8.2, 1.0 Hz, 1 H), 7.78 (ddd, J = 8.3, 7.1, 1.3 Hz, 1 H), 7.70 (dd, J = 8.3, 0.7 Hz, 1 H), 7.51 (ddd, J = 8.2, 7.1, 1.2 Hz, 1 H), 6.95 (d, J = 1.0 Hz, 1 H), 2.63 (d, J = 1.0 Hz, 3 H); ^{13}C-NMR (126 MHz; DMSO-d_6): δ 153.6, 152.4, 135.5, 132.3, 125.4, 124.8, 121.1, 117.5, 112.6, 19.0; ESIMS *m/z* (rel. intensity) 159 (MH^+, 100). HPLC purity: 100%.

Results and Discussion

Spectral Binding Analysis. Although the various NOS isoforms have very similar active site structures, one potentially important difference between mammalian and bacterial NOS isoforms is that an L-Ile in bNOS, which is a L-Val in mNOS isoforms, interacts with hydrophobic portions of inhibitors. Previously, we postulated that this subtle difference in hydrophobicity might contribute to inhibitor selectivity for bNOS[42]. To further evaluate the role of the bNOS Ile residue, we performed mutagenesis studies in bsNOS and the reverse mutation studies in iNOS. From the 17 aminoquinoline inhibitors studied here, Ile-218 was observed to contribute to the bsNOS inhibitor specificity (Table 2.1) as noted by an increase in K_s for the I218V bsNOS mutant. Specifically, for both **1** and **2** we observed a 26-fold and 7-fold decrease in inhibitor specificity between WT and I218V, respectively. However, this trend was not consistently observed for the K_s measured in iNOS WT and V352I iNOS. In fact, the K_s only decreased for compounds **7**, **8**, **13**, and **14** when V352I was introduced in iNOS and increased for 10 of the other inhibitors.

Aminoquinoline Inhibition of bNOS. The two most potent bsNOS inhibitors identified by K_S analysis (**1** and **2**, Table 2.1), were also the simplest aminoquinolines studied. To further evaluate the relationship between Ile218 and the inhibitory potential of aminoquinolines, both **1** and **2** were evaluated using the previously described bBiDomain assay[44]. The bBidomain is a construct consisting of the *B. subtilis* flavodoxin, YkuN, fused to the C-terminal end of bsNOS. In the presence of the *B. subtilis* FAD-containing reductase, YumC. and NADPH the bBidomain oxidizes substrate much more rapidly than the 3 component system consisting of bsNOS, YkuN, and YumC. [44] This has provided a more facile method for rapidly screening the ability of inhibitors to block bsNOS activity. [42] Both of these compounds were found to have IC_{50} values in the low μM range (Table 1.2). From these studies we also found that introduction of I218V to bBiDomain resulted in a small increase in the measured IC_{50} values.

Crystal Structure Analysis. Although 22 crystal structures were solved, we focus here on those that provide the most important insights into the effect of the I218V mutation. As expected, in all of these structures the aminoquinoline forms stacking interactions with the heme group and hydrogen bonds with the conserved active site Glu243, and it directly contacts Ile218 through a van der Waals interaction (Figure, 1.2, Figure. S1.1). For the simplest inhibitors, **1** and **2**, the 8-27 fold decrease in binding affinity in the I218V bsNOS mutant can be rationalized based on the additional non-covalent interactions between Ile218 and the inhibitor compared to Val218. We estimated the additional stability of the larger Ile vs. Val by calculating the non-bonded interaction energy between the inhibitor and residue 218 using the Sander module in Amber. The WT Ile provides an additional -1.8 kcal/mol greater stability. This is in agreement with the DG obtained from the spectral K_s data (≈-2 kcal/mol).

The addition of a linker to the aminoquinoline with various tail groups results in various binding orientations of the inhibitor tail, which extends out of the active site. The inhibitor tail binds better for some inhibitors than others as judged by the electron density. For example, the

electron densities observed for the tail end of inhibitors **6** and **8** are well ordered, while those for inhibitors **10** and **13** are not (Figure 1.2). There is also a relationship between how well ordered the tail end of the inhibitor is and the effect of the I218V mutant on binding affinity. For example, both inhibitors **6** and **8** were found to have well-defined electron density throughout. The more well-defined electron density inhibitors, such as **6** and **8**, were also minimally perturbed by the I218V mutation on the basis of differences in K_S (Table 1.1). In contrast, inhibitors with less defined inhibitor electron density, such as **10** and **13**, have K_S differences of 8 and 120 fold, respectively, between WT and I218V bsNOS (Table 1.1). We postulate that for inhibitors **10** and **13** the tail end of the inhibitor does not contribute much to stability so the effect of the mutation on binding to the aminoquinoline part of the inhibitor is more pronounced. Conversely, the effect of the mutant is less pronounced for **6** and **8** since the tail end contributes more to inhibitor binding. This results in a decreased effect on the mutation on the aminoquinoline portion of the inhibitor. One reason **6** and **8** have a more ordered tail is due to the interaction of the secondary amino group with the heme propionates.

Since the I218V mutation has a large effect on the K_S of inhibitor **13**, the crystal structure of the mutant enzyme bound to **13** was also solved (Figure 1.2). In the mutant, the tail end of the inhibitor exhibits weak density, and the F_o-F_c maps indicate that the tail of the inhibitor occupies at least two orientations. An important difference between **13** and some of the other inhibitors is that the linker in **13** has an ether oxygen rather than a secondary amino group. As a result, the linker of **13** cannot form a H-bond with the heme propionate, while the secondary amino group of inhibitors like **8** can form a hydrogen bond. Given the extra interactions in **8**, the I218V mutation has little effect, while for **13**, with no linker H-bonding possibilities, the effect of the destabilizing I218V mutation is much larger because the aminoquinoline itself contributes more to overall binding.

One remaining question is why the I218V mutation has a large effect on K_S in bsNOS but the reverse mutation in iNOS, V352L, has little effect. For example, the I218V mutation decreases affinity for inhibitor **13** by approximately 120 fold in bsNOS but there is little difference between WT iNOS and the V352I mutant. There are, however, other differences in the active site between bsNOS and iNOS. For example, His128 in bsNOS is replaced by Ala in iNOS. His128 contacts both the central region of the larger inhibitors as well as Ile218 thereby restricting inhibitor mobility within the binding pocket. The bsNOS active site is also more open than the iNOS active site because, unlike iNOS, bsNOS does not contain an N-terminal Zn^{2+} binding motif. Previously, we have observed that the open pterin site of bsNOS accommodates the binding of aminopyridine-based inhibitors[41] and allows for the binding modes of thiophenecarboximidamide-based inhibitors that are unique to bsNOS[33]. Therefore, it is likely that the N-terminal binding motif in iNOS also influences the binding of the longer aminoquinoline inhibitors that extend out of the active site in bsNOS.

Initial structural studies of aminoquinolines binding to bsNOS indicated that they might bind to the pterin site (data not shown). To determine if aminoquinolines can bind to this site we prepared crystals of **6** and **16** without H_4B present during the cryosoak. Processing of the crystallographic data provided a two-site binding model of both **6** and **16** to bsNOS when H_4B is absent (Figures 1.3B and 1.3D). In these two site models, one inhibitor is bound at the active site and the second binds to the pterin site by forming a π-π stacking interaction with Trp329. In the case of **6**, inhibitor binding at the pterin site requires a water molecule to bridge a hydrogen bond to the heme propionate group. Binding of **6** is further stabilized by a salt bridge between the secondary linker amine of **6** and R344(C=O) at the dimer interface (Figure 1.3B). Unlike **6**, a hydrogen bond between inhibitor linker and R344(C=O) is not observed with **16** because it has an ether-linked tail (Figure 1.3D). On the basis of $2F_o$-F_c maps, the binding of both **6** and **16** to the pterin site is weak compared to binding of H_4B, as H_4B can easily out-compete the aminoquinoline inhibitors evaluated. Inspection of both **6** and **16** bound to the active site reveals

the binding mode to be unchanged regardless of the ligand present at the pterin site (Figure 1.3). This confirms our earlier observations that the aminopyridine of inhibitors prefer the pterin site over aminoquinolines[41]. Even in the presence of H_4B we have found that aminopyridines can be quite effective at displacing H_4B while aminoquinolines prefer the active site[41].

Conclusions

Aminoquinoline-based inhibitors have been developed to inhibit NOS activity. Since the aminoquinoline scaffold also has been previously found to function as an antimicrobial agent against the highly pathogenic organism MRSA[42], an improved understanding of aminoquinoline binding to bNOS was necessary to further drug design efforts and identify new scaffolds for inhibitor design. Previous evidence also indicates that the potency and specificity afforded by the aminoquinoline-based inhibitors to be controlled by the subtle differences in hydrophobicity at the bNOS active site[42]. Specifically, the hydrophobic patch contributed by Ile-218 (mNOS equivalent residue is Val) allows for tighter binding of the aminoquinoline group as a result of a van der Waals interaction between the aminoquinoline group and active site Ile-218 residue.

On the basis of these results one might have anticipated that the reverse mutation in iNOS, V352I, should improve binding, but there is little difference between WT and mutant. However, in bsNOS His218 contacts the inhibitor while this equivalent residue is an L-Ala in iNOS and a L-Ser in both *H. sapiens* endothelial NOS (eNOS) and neuronal NOS (nNOS), respectively. As a result, the active site of bsNOS provides more contacts with the aminoquinoline inhibitors. These results, combined with previous studies, indicate at least two structural and functional differences between bNOS and mNOS that can be exploited in the design of bNOS-selective inhibitors. First, the larger aminoquinoline compared to the smaller aminopyridine favors the bNOS active site owing to the more extensive nonbonded contacts provided by Ile218. Second, aminopyridines favor the pterin site over aminoquinolines. Targeting

the pterin site might be especially useful since pterins bind more weakly to bNOS than nNOS, which should result in easier displacement of H_4B by inhibitors in bNOS. Thus, an inhibitor with an aminoquinoline in the active site and an aminopyridine in the pterin site has the potential to be an especially potent and selective bNOS inhibitor.

Acknowledgements

This work is greatly indebted to the expertise and wisdom provided by Dr. Huiying Li. We are also very grateful to the beamline staff at both the Advanced Light Source and the Stanford Synchrotron Radiation Light source (Palo Alto, CA) for help with remote data collection. This work was supported by National Institute of Health grants GM57353 (to TLP), GM49725 (to RBS), and F32GM109667 (to MAC).

Supporting Information

A summary of crystallographic and refinement statistics are provided in Table S1 and the electron density map for various inhibitors in Fig. S1.1.

Table 1.1. Spectral binding constants for inhibitors against NOS isoforms and mutants. [α]Value reported in [14], [β] Value reported in [42].

Ligand	bsNOS WT K_S (μM)	bsNOS I218V K_S (μM)	Human iNOS K_S (μM)	Human iNOS V352I K_S (μM)
L-Arg	4.8 ± 0.1[α]	2.0 ± 0.2[α]	16.1 ± 0.7[α]	40.9 ± 4.3[α]
1	1.25 ± 0.03	33.3 ± 1.5	4.5 ± 0.5	11.1 ± 0.7
2	0.80 ± 0.08	6.1 ± 0.3	3.5 ± 0.2	14 ± 1
3	3.2 ± 0.1	41 ± 6	7.1 ± 1.2	50 ± 18
4	3.2 ± 0.1	97 ± 6	91 ± 5	76 ± 6
5	1.3 ± 0.1	31 ± 2	40 ± 6	40 ± 3
6	6.7 ± 0.7[β]	12 ± 1[β]	42 ± 8	43 ± 5
7	3.6 ± 0.8[β]	18 ± 2	70 ± 35	50 ± 9
8	14.1 ± 0.4	11 ± 3	107 ± 39	80 ± 19
9	2.0 ± 0.1	34 ± 3	34 ± 4	44 ± 4
10	19 ± 1	154 ± 12	14 ± 3	36 ± 11
11	7.5 ± 0.3	182 ± 39	18 ± 2	33 ± 11
12	3.4 ± 0.1	266 ± 100	11 ± 1	56 ± 9
13	2.7 ± 0.1	320 ± 140	140 ± 29	122 ± 16
14	3.0 ± 0.1	39 ± 2	39 ± 3	26 ± 2
15	2.2 ± 0.1	184 ± 35	61 ± 6	61 ± 7
16	3.4 ± 0.1	103 ± 22	67 ± 14	117 ± 20
17	1.3 ± 0.1	17 ± 2	2.8 ± 0.3	8.3 ± 1.5

Table 1.2. IC_{50} (μM) of aminoquinoline inhibitors evaluated using bBidomain.

	WT	I218V
1	27.3	63.9
2	36.6	53.3

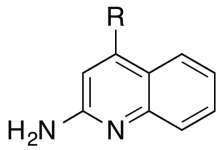

1. R=H
2. R=CH_3

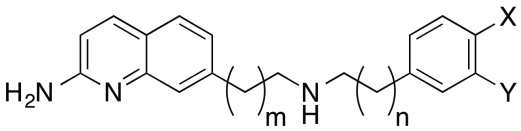

3. m=0, n=1, X=F, Y=H
4. m=0, n=2, X=H, Y=F
5. m=1, n=0, X=F, Y=H
6. m=1, n=1, X=H, Y=F
7. m=1, n=2, X=F, Y=H
8. m=0, n=0, X= H, Y= $N(CH_3)_2$

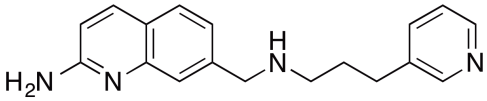

9.

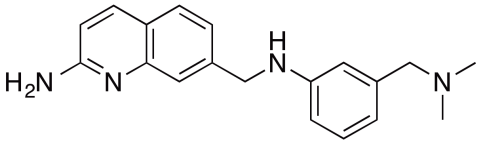

10.

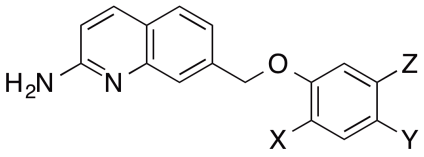

11. X=CH_2NHCH_3, Y=H, Z=H
12. X=H, Y=H, Z=CH_2NHCH_3
13. X=H, Y=H, Z=$CH_2CH_2NHCH_3$
14. X=H, Y=Cl, Z=$CH_2CH_2NHCH_3$
15. X=H, Y=H, Z=CH_2NH_2
16. X=H, Y=$CH_2N(CH3)_2$, Z=H

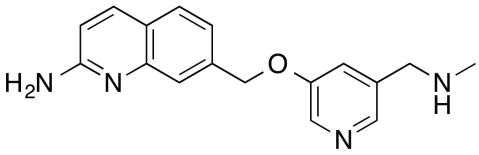

17.

Figure 1.1. NOS inhibitors reported in this study. Chemical syntheses of inhibitors **1**, **2**, and **11** are reported here (see Experimental Procedures). Syntheses of **3-7** are reported in [53] and that of **8** and **9** are reported in http://patents.justia.com/patent/9212144. Syntheses of inhibitors **10** and **12-17** are reported in [113].

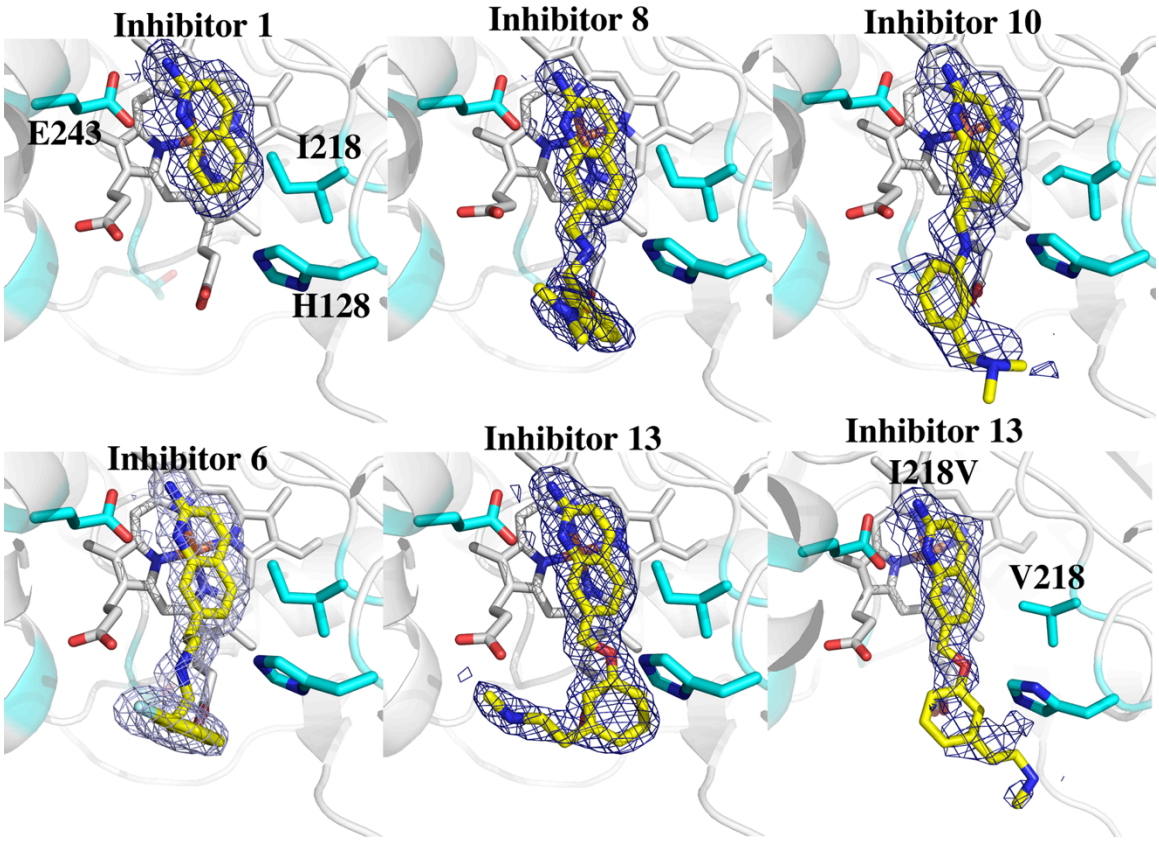

Figure 1.2. Crystal structures of WT and I218V bsNOS complexed with inhibitors shown in yellow and a F_o-F_c map contoured at 1.0s. The aminoquinoline group binds to the NOS active site for all molecules through a hydrogen bond to E243. The tails of inhibitors **6**, **8**, and **10** are stabilized by hydrogen bonds to heme propionate. **13** contains an ether group that positions the inhibitor tail away from the heme propionate group because of electrostatics.

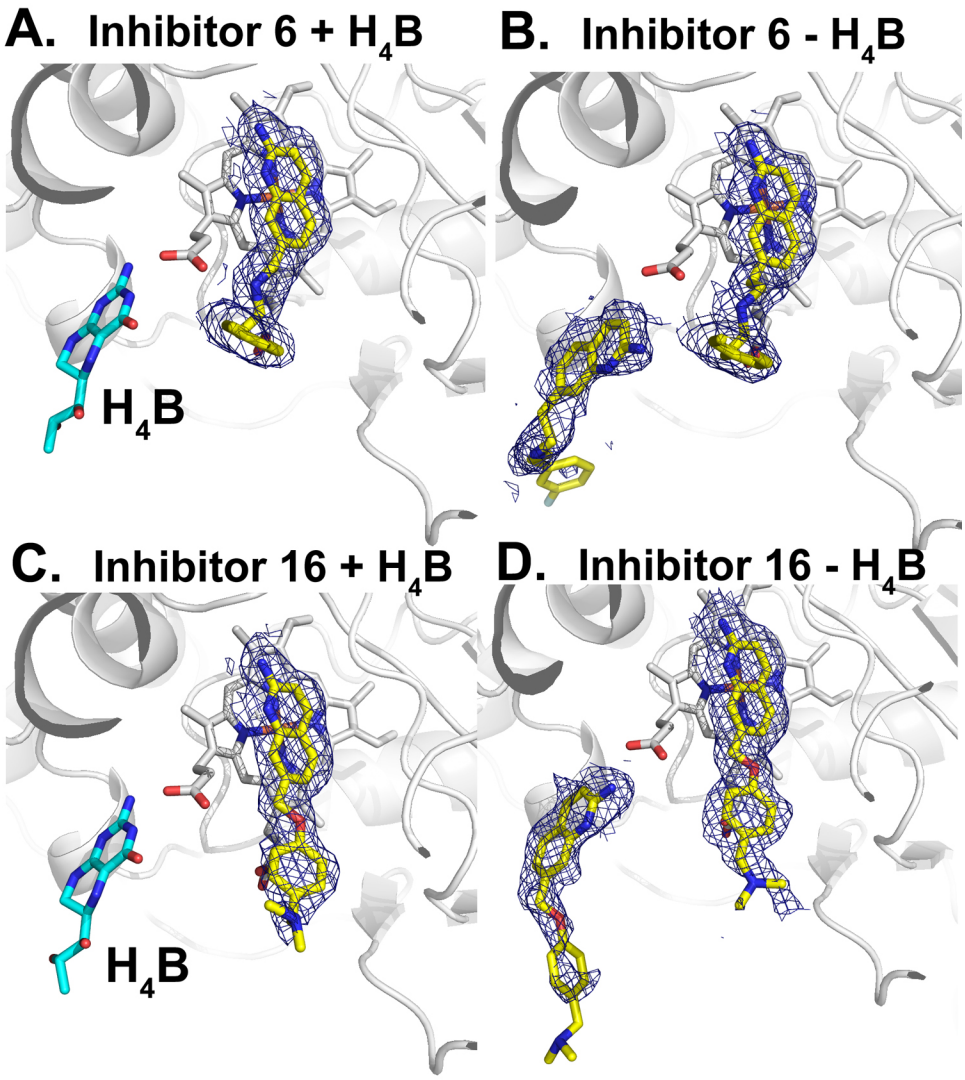

Figure 1.3. $2F_o$-F_c maps contoured at 1 σ for inhibitors **6** and **16** both in the presence and absence of H_4B. Inhibitors are colored yellow and H_4B is shown as cyan. When H_4B is absent inhibitor binding is also observe at the pterin site for B) **6** and D) **16**.

Chapter 2

Selective Anti-MRSA Inhibitors Targeting Nitric Oxide Synthase

Intro

Mammals have 3 isoforms of nitric oxide synthase called endothelial NOS (eNOS), neuronal NOS (nNOS), and inducible NOS (iNOS)[56]. Each isoform oxidizes L-arginine to L-citrulline and nitric oxide (NO). NO is an important signaling molecule in neural transmission (nNOS), in maintaining vascular tone (eNOS), and in the immune system (iNOS). Certain gram positive bacteria such as methicillin resistant *Staphylococcus aureus* (MRSA) and *Bacillus anthracis* also produce NO using a similar NOS, although there are two major structural differences between bacterial NOS (bNOS) and mammalian NOS (nNOS). First, mNOS has the heme-containing active site domain where the substrate, L-Arg, binds fused to the N-terminal end of a P450 reductase like domain that shuttles NADPH derived reducing equivalents to the heme. bNOS, however, is a stand alone heme domain and thus requires redox partners to bind and deliver electrons to the heme. Second, while both mNOS and bNOS form heme domain dimers, bNOS lacks the zinc binding motif at the dimer interface that helps stabilize the mNOS dimer.[15, 36] The active sites, however, are very much the same.

bNOS generated NO is known to protect gram positive bacteria from antibiotic and host induced oxidative stress and is important for establishing infections.[38, 39, 57] One promising explanation for how NO protects bacteria is that NO prepares the infectious agent for anaerobic respiration, an advantage in the anaerobic environment encountered by the bacteria during infection.[58] Since NO can readily coordinate to heme iron, NO is capable of shutting down respiration by blocking the bacterial equivalent of cytochrome oxidase where O_2 is reduced. bNOS generated NO readily oxidizes to nitrate which then serves as alternate electron acceptor

under conditions where O_2 levels are low. Given the importance of NO for MRSA to establish an infection, bNOS is a viable drug target. In previous studies we screened a large number of novel NOS inhibitors designed to selectively inhibit nNOS[59, 60] and found that some of these inhibitors are effective in working synergistically with antibiotics and H_2O_2 induced oxidative stress to kill *B. subtilis* and MRSA[31, 41]. While many of these compounds inhibited various mNOS isoforms about as well as bNOS, a large number of crystal structures[31, 33, 41, 42] revealed potentially important structural differences that can be exploited to develop highly selective bNOS inhibitors that target the pterin cofactor binding pocket. All mNOS isoforms require tetrahydrobiopterin (BH4) as a cofactor[61, 62] and while bNOS also can use BH4, it remain unclear which cofactor is utilized *in vivo*. As shown in Figure 2.1, BH4 binds in a pocket near one of the heme propionates. The BH4 pocket in bNOS is much larger and more exposed than in mNOS, which translates into a weaker affinity of pterins in bNOS. In our previous crystallographic studies we found that various inhibitors can more readily displace BH4 from bNOS than mNOS[31, 33, 41, 42]. Based on these observations, we now have designed, synthesized, solved crystal structures, and tested for MRSA killing ability a series of inhibitors that specifically target the bNOS pterin binding pocket.

Results

Crystal Structures

The crystal structures of QJ13 bound to bsNOS and rat nNOS (Figure 2.2)[41] provided the first hint that BH4 can be more readily displaced in bsNOS than in the various mammalian NOS isoforms. As shown in Figure 2.2, QJ13 flips 180^o in nNOS relative to bNOS and in bNOS the tail end aminopyridine displaces the BH4, even when BH4 is included in the crystallization medium[41] QJ13 does not displace BH4 in nNOS, presumably because BH4 binds more tightly to nNOS than to bsNOS. This together with the fact that QJ13 exhibited increased bacterial killing activity,[41] prompted us to design and synthesize NOS inhibitors that will displace BH4 in bNOS but not mNOS. An important design feature that emerged from our previous studies is

that aminoquinolines prefer to bind in the active site of bNOS compared to mNOS, where the smaller aminopyridines prefer to bind. One key difference that might control this preference for aminoquinolines by bNOS is that bNOS has Ile218 where mNOS has a (Val567 in nNOS) at this position (Figure 2.2). The slightly larger Ile side chain provides better non-bonded contacts with the larger aminoquinoline. Indeed, the Ile/Val mutant shows that this difference does contribute to better aminoquinoline binding.[63] Therefore, the inhibitors in this study all contain an aminoquinoline that should bind in the active site and a tail pyridine or aminopyridine that should extend out of the active site and bind in the BH4 pocket. Our initial efforts have resulted in the analysis of the seven compounds shown (compound PWA101 to PWA207 in Figure 2.3) and Table 2.1 summarizes the results of spectral dissociation constants and IC50 values determined for bsNOS, human eNOS and human iNOS. Table 2.2 shows the crystallographic details and PDB codes. Each compound exhibits excellent selectivity for bsNOS. With the exception of PWA115, we were able to obtain crystal structures of these compounds complexed to bsNOS but only the eNOS-PWA150 complex gave crystals suitable for crystallographic analysis. The 2Fo-Fc electron density maps contoured at 1.0σ for each complex are shown in Figure 2.4. In all the bsNOS structures the aminoquinoline of the inhibitor is positioned over the heme, enabling the inhibitor to H-bond with the active site Glu243. In addition, the tail end of the inhibitor with a pyridine or aminoquinoline is positioned in the BH4 binding pocket. Structures were solved with or without BH4 included in the crystallization medium and in all cases the inhibitor still bound to the BH4 pocket. The bsNOS-138 structure is a bit ambiguous and can be modeled with either the aminopyridine or aminoquinoline. The eNOS-150 structure has the inhibitor bound just the opposite to bsNOS (Figure 2.4). The aminopyridine is bound in the active site with the aminoquinoline extending out. This difference in binding mode is undoubtedly due to the inability of the inhibitor to displace BH4 in eNOS. This translates into a much larger IC50 in eNOS than in bsNOS.

The most potent inhibitors with Ks ≈ 2mM are 206 and 207. Similarly to all the other inhibitors, the aminoquinoline binds in the active site and H-bonds with Glu243. The tail aminopyridine for both bind in the BH4 pocket and form H-bonds with the heme propionate. 103 binds similarly although with slightly weaker affinity, ≈ 6.2 μm. 103 has 6 atoms between the central phenyl ring and amnopyridine while 206 and 207 have 5 and 3, respectively. As a result the linker secondary amine of 103 does not establish H-bonding interactions with either Arg247 or the heme propionate as do 206 and 207. In 150 there are only 2 atoms between the central phenyl ring and aminopyrydine. As a result, the aminopyridine cannot H-bond to the heme propionate as in the other inhibitors and instead, owing to potential steric clashes, the aminopyridine N atoms point away from the heme propionates. This no doubt accounts for why 150 binds about an order of magnitude more weakly, K_S = 29.9 μm, than 206 or 207. Even so 150 is the most selective over human eNOS and iNOS (Table 2.1).

Macrophage Killing of MRSA Assay – An integral part of the drug development pipeline is testing the efficacy of the drugs to not only reach their targets, but also demonstrate their selectivity. This is particularly important with regards to bNOS, given the similarity between bNOS and the mammalian NOS isoforms. Of the two lead candidate compounds, 206 and 207, 206 showed greater selectivity and efficacy in inhibiting bNOS and reduced the surviving percentage of MRSA in macrophages to 12.57 ± 6.41% at 125 μm (Figure 2.6). 207 also showed some efficacy at 125 μm, reducing the surviving bacteria to 70.4 ± 12.5 %.

Hydrogen Peroxide Survival Assay - A notable effect of bNOS is its integral role in protecting bacteria from the deleterious effects of radical oxide stress. Pathogenic bacteria are exposed to such an environment after being phagocytized by host immune cells. To test our inhibitors efficacy in preventing the survival response, we exposed the bacteria to 5mM H_2O_2, and 200 uM doses of either substrate LARG or inhibitor. Arginine provided a protective effect and allowed

the bacteria to recover from the stress as evidence by the bacteria growing to 112.7 ± 19.9% of the initial inoculum after 30 minutes of treatment. (Figure 2.7A). LNAME inhibited the recovery of the bacteria to 22.2 ± 4.4% of the initial inoculum, while 206 and 207 significantly inhibited the recovery of the bacteria to 2.7 ± 1.2% and 10.5 ± 1.5%, respectively. (Figure 2.7B, C, and D).

Conclusions

It had previously been hypothesized that an inhibitor with an aminoquinolone head group and an aminopyridine tail would be a potent and selective bNOS inhibitor to treat MRSA.

It had also been previously noted that binding affinity did not correlate strongly to efficacy in producing molecules that both inhibit bNOS and show efficacy in killing MRSA in the presence of ROS stress. Here we have designed such a class of inhibitors that selectively occupy both the active and the pterin site of bNOS. This selective binding mode displays potency in both inhibiting bNOS function more efficiently than mNOS, and is able to demonstrate selectivity for bNOS over iNOS in mouse macrophages. In addition, our two lead compounds greatly increase the efficacy of H_2O_2 mediated bacterial killing. Further investigation is necessary to determine the efficacy of these drugs in preventing or aiding in clearance of infection in an *in vivo* model. Further optimizations in the scaffold might generate inhibitors with even great selectivity for bNOS over mNOS.

Plasmid Preparation - Nitric Oxide Synthase DNA from *Bacillus subtilis* was cloned into a pET28a (Novagen) plasmid and prepared as previously described.[Holden, 2013 #8]

Expression and Purification - bsNOS, bsNOS-YKuN fusion, I218V bsNOS, and I218V bsNOS-YKuN fusion were overexpressed in *E. coli* BL21(DE3) and purified as previously described.[Holden, 2013 #8] *E. coli* were transformed with their respective plasmids via heat

shock and plated on selected media. Individual colonies were selected and grown, and sequenced to confirm gene presence. 1L cultures were grown to an OD_{600} of 0.6 at 37°C, 220 rpm. Protein expression was induced with 1mM IPTG and 0.4 mM δ-ALA, and expressed for 48 hours at 100 rpm and room temperature (roughly 25 °C). Cells were spun down at 4k rpm, 10 minutes, 4°C. Cells were resuspended in buffer containing 50 mM Tris (7.4), 150 mM NaCl, 2 mM DTT, 5 mM L-Arg, 5 mM Imidazole. Cells were lysed via high pressure liquid homogenization. Lysate was separated from cell debris by centrifugation at 15000 rpm, 4 °C, for 40 minutes. bNOS was purified as previously described [42].

Imidazole Displacement - The sample absorbance was measured using a Cary 3E UV-visible spectrophotometer while inhibitors were titrated into a cuvette containing 50 mM Tris (pH 7.4), 1 mM imidazole, 100 uM dithiothreitol, 10 mM NaCl, and the comparable NOS at 2 uM. The difference in absorbance of imidazole bound low-spin Soret peak at 430 nm and the inhibitor bound high spin Soret peak at 395 nm was calculated as a function of inhibitor concentration, as previously annotated for bsNOS, bsNOS I218V[41]. From these data, $K_{S,app}$ was calculated from the concentration of inhibitor required to convert 50% of the sample from low-spin to high spin and was determined as a previously reported using nonlinear regression analysis available in Sigmaplot version 10.0 (Systat Software, Inc.). The K_s for each ligand was then calculated from $K_{S,app}$ as previously described,[41] using the K_D of imidazole to bsNOS, bsNOS I218V, iNOS, eNOS and normalized to L-Arg.

IC_{50} Determination - Enzyme activity for bsNOS and bsNOS I218V was measured using the bBidomain constructs, as described previously[63], with some minor caveats. bsNOS, bsNOS I218V had reactions run for 8 minutes, whereas hiNOS and heNOS were run for 4 minutes, as this allowed for adequate signal before complete substrate depletion. hiNOS and heNOS

reactions also had calmodulin added at 10x protein concentration. Inhibitors were tested from 5 μM to 800 μM. IC_{50} was calculated as previously described [63].

Crystallization and Sample Preparation – bsNOS crystals from space group $P2_12_12$ were grown via vapor diffusion at room temperature (approximately 22° C). Initial crystals were obtain by mixing of equal volumes of crystallization buffer and bsNOS at 38 mg/mL in 25 mM Tris pH 67.6, 150 mM NaCl, 1 MM DTT. The reservoir was composed of 60 mM BisTris and 40mM citric acid pH 7.6 and 20% vol/vol polyethylene glycol (PEG) 3350, and 1% propanol. Initial crystals were crushed and used as seed stock for subsequent crystals grown in the same conditions. These crystals then had inhibitors ± BH_4 , both at a concentration of 3mM soaked in during cryoprotection with 23% vol/vol glycerol for 3 hours.

X-Ray Data Collection and Processing – X-ray diffraction data were collected on individual crystals at both the Advanced Light Source (Berkeley, CA) and the Stanford Radiation Light Source (Palo Alto, CA). Data frames were indexed and integrated using either MOSFLM [46] or XDS. [47] Indexed data sets were scaled using Aimless[48]. Structure factors were initially refined using PHENIX [51] COOT [52] was used to model inhibitor binding and PyMOL(Version 2.0.5, Schrödinger, LLC) was used to create figures. Data collection and refinement statistics are listed in Table 2.2.

KILLING ASSAYS – Mouse macrophages were differentiated from bone marrow from 2-6 month old C57BL/6J mice bred at UCI. Bone marrow was isolated, red blood cells lysed with ACK buffer (Gibco), and plated on non-tissue culture treated dishes (Fisher) in DMEM media (Hyclone) supplemented with 2mM L-glutamine (Corning), 100U/mL pen-strep (Hyclone), 10% fetal bovine serum (OmegaScientific), and 10% cell conditioned media from CMG14-12 cells as a source of CSF[64]. Macrophages were isolated after 6 days of differentiation and stored frozen

in liquid nitrogen. One day prior to assay, macrophages were thawed and plated in flat-bottomed 96-well culture plates (VWR) at 50-70,000 cells per well in antibiotic-free DMEM media supplemented with 10% fetal bovine serum and L-glutamine.

MRSA was grown overnight in TB supplemented with 1mM Glucose. Overnight cultures were then diluted to an OD_{600} of 0.4, and adjusted to have an inoculum of 3-5x of the macrophage cell number plated per well. Bacteria and inhibitors or vehicle control were added to each well. Plate was spun down for 5 minutes, 1500 rpm, 25°C to bring bacteria in contact with the macrophages. Plate was incubated for 1 hour at 37°C with 5% CO_2. Plate was spun down for 5 minutes, 1500 rpm 25 C. Supernatant was pippeted off and discarded. Cells were lysed with 2% Triton-X 100 for 15 minutes. 100 ul of 1 mg/mL MTT in LB were added to each well, and plates were incubated for 2 hours at 37C. MTT was solubilized in DMSO, and plates were read at 540 nM. Killing measurements were normalized to untreated bacteria. Empty wells with known bacteria quantities were used as a positive control. Conditions were sampled in triplicate, values are presented as mean ± SD. Statistical analysis was performed using Excel (Microsoft) and Prism (GraphPad).

Hydrogen Peroxide Killing - MRSA was grown overnight in TB supplemented with 1mM Glucose. Overnight cultures were then diluted to an OD_{600} of 0.4, and adjusted to have an concentration of ~2 * 10^7 cfu/ml. 25 uL volumes were dispensed into 96-well plate with 200 uL aliquouts of LB or LB with 5mM Hydrogen peroxide, 200 uM of LARG, LNAME or Inhibitor. Plates were incubated at 37°C with shaking. Cultures were sampled at T_0 and T_{30} by removing 25 uL for serial dilution in LB and spot plating on TB agar. Plates were incubated overnight and the culture cfu/ml concentration was calculated by enumerating colonies and multiplying back through the dilution factor. Conditions were sampled in triplicate, values are presented as mean ± SD. Statistical analysis was performed using Excel (Microsoft) and Prism (GraphPad).

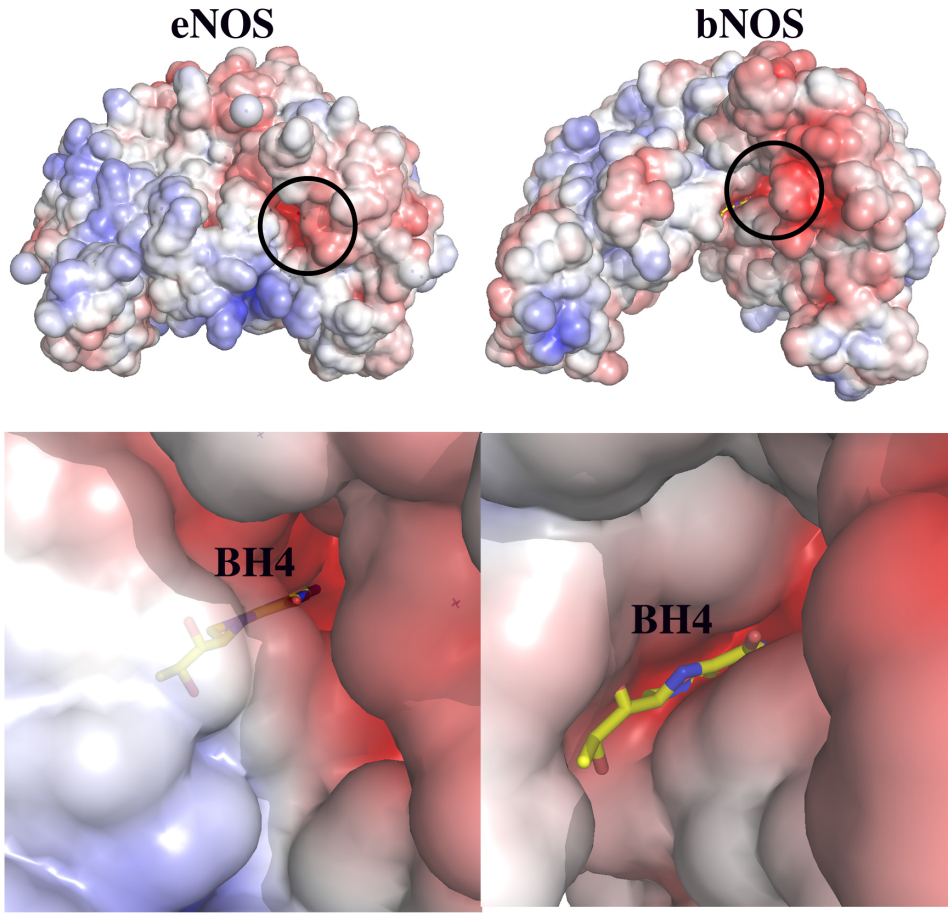

Figure 2.1 – Structures of eNOS and bsNOS showing the electrostatic surface potential contoured at ±5kt (red=negative, blue=positive). Close-up views of the BH4 binding pocket illustrate that the BH4 electronegative pocket is larger and more exposed than in eNOS.

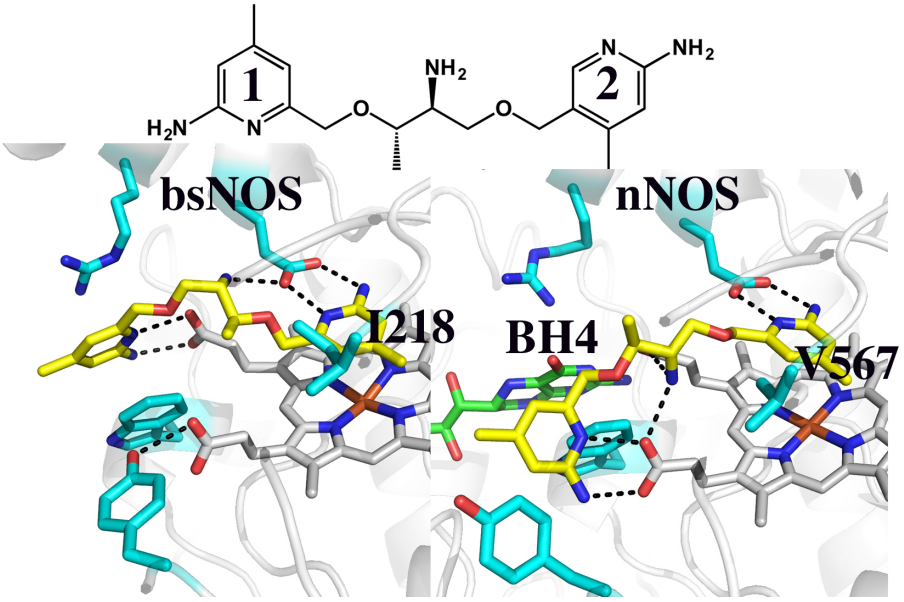

Figure 2.2 – Crystal structure of eNOS (PDB 4LUX) and bsNOS((PDB 4LWA) bound to QJ13. In bsNOS the **2** aminopyridine ring binds over the heme while the **1** ring binds in the BH4 pocket. In eNOS it is just the opposite with the **2** ring over the heme while the **1** ring extends out of the active to interact with one of the heme propionates. QJ13 is able to displace BH4 in bsNOS but not eNOS.

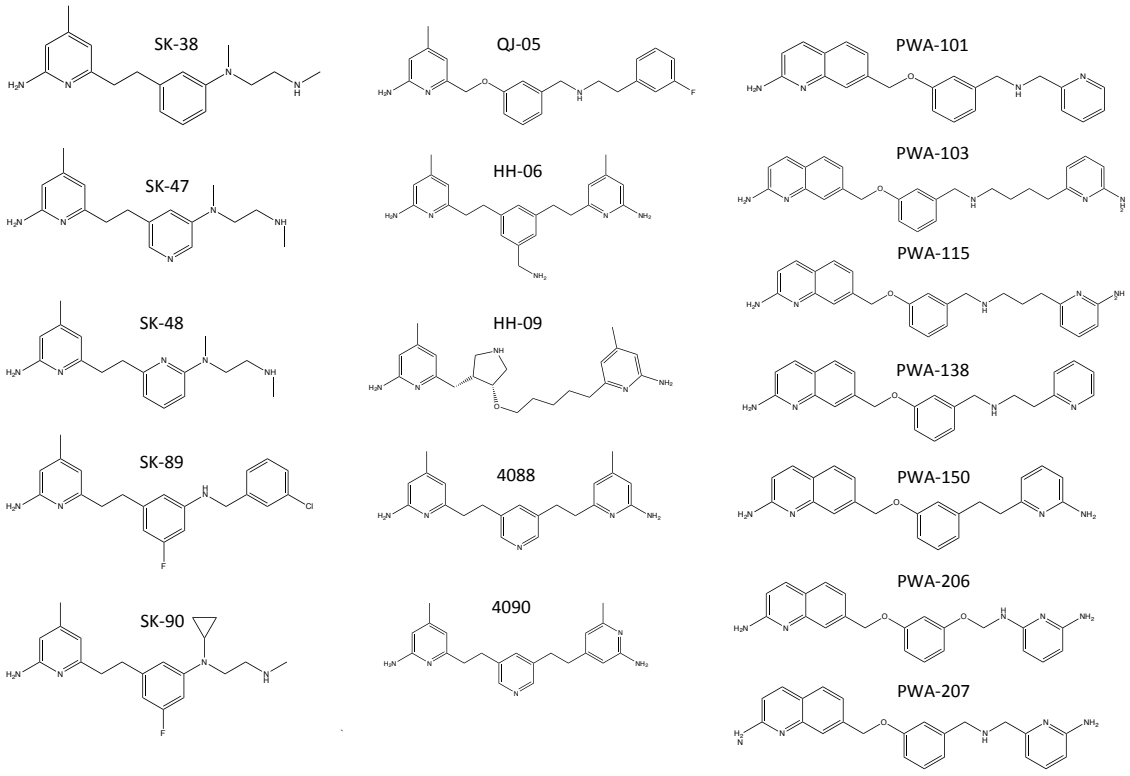

Figure 2.3 – Structures of NOS inhibitors used in this studies. Compounds X to Y are new to this study while structure A to B are from previous studies.

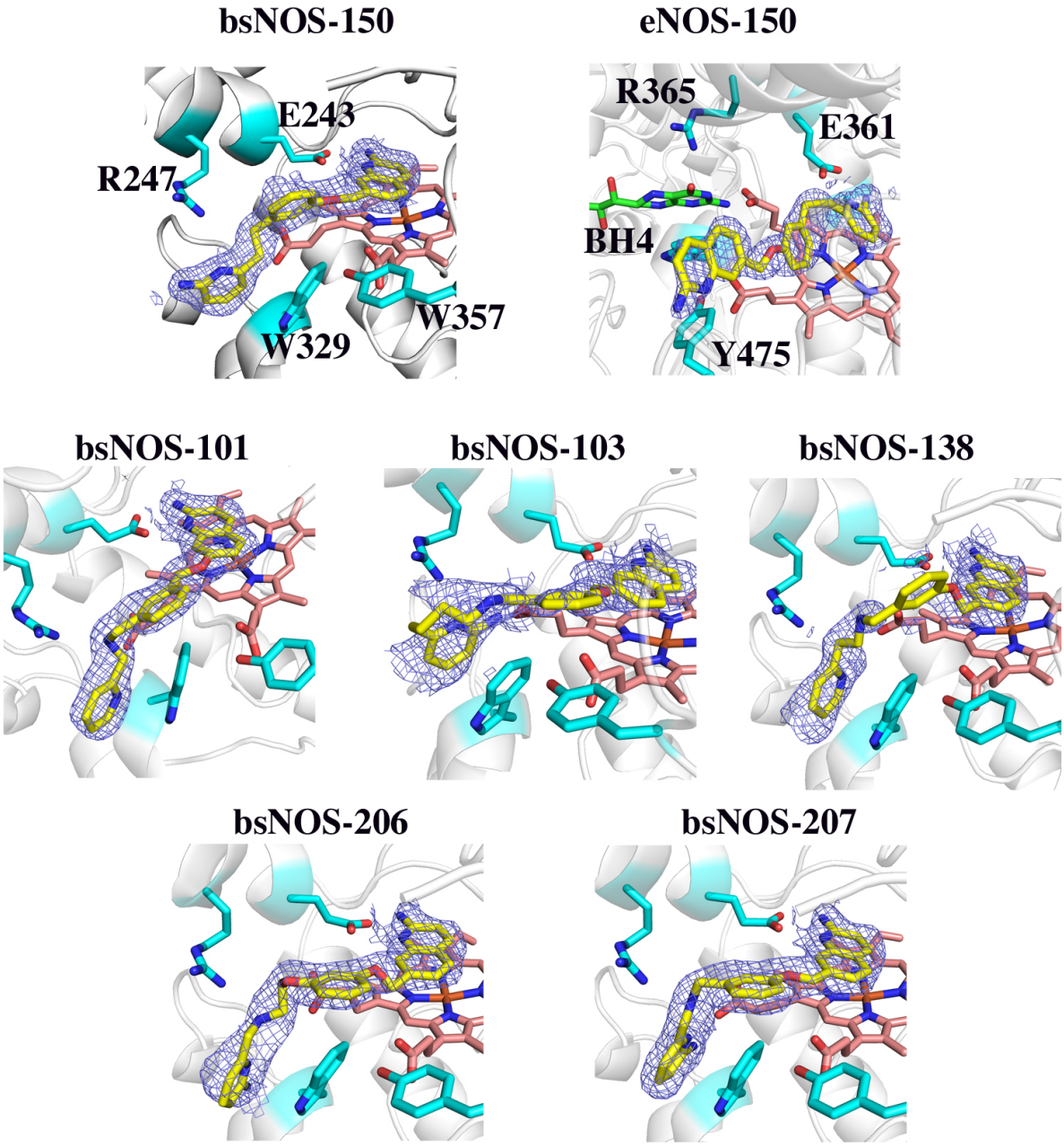

Figure 2.4 – 2Fo-Fc electron density maps of contoured at 1.0s for PWA inhibitors bound to bsNOS and PWA 150 bound eNOS.

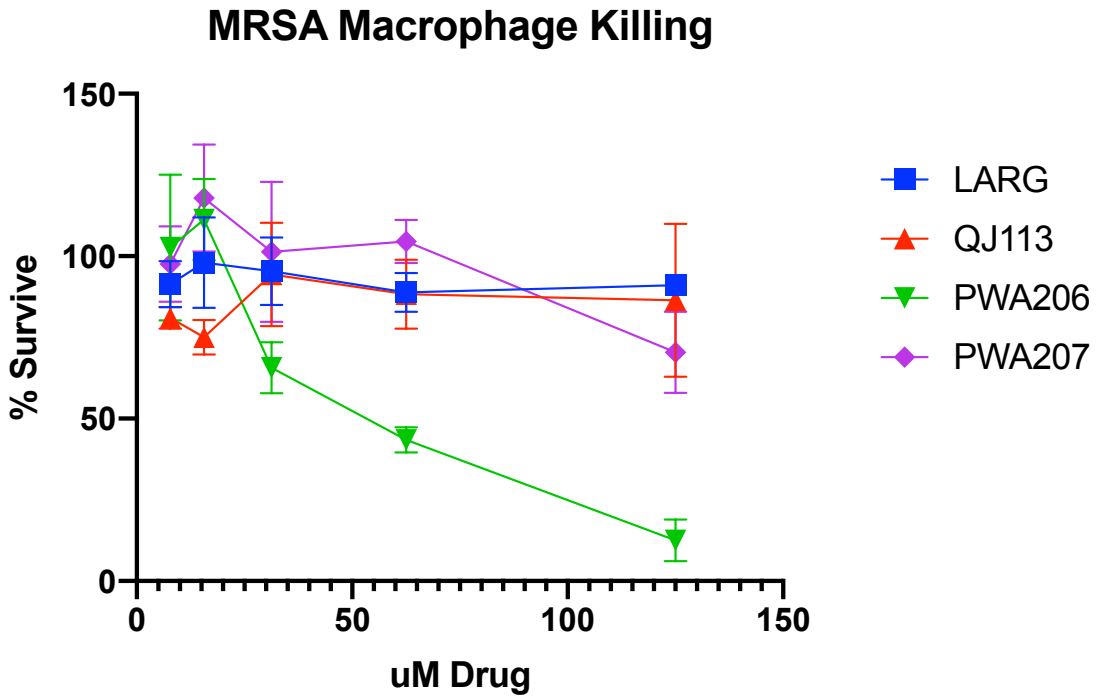

Figure 2.5 – A plot of the experimental results of MRSA killing by macrophages. L-ARG and L-NAME were ineffective at inhibiting survival of MRSA. PWA 206 showed great efficacy for inhibiting bacterial survival intracellularly. PWA 207 was only able to inhibit survival at 125 uM.

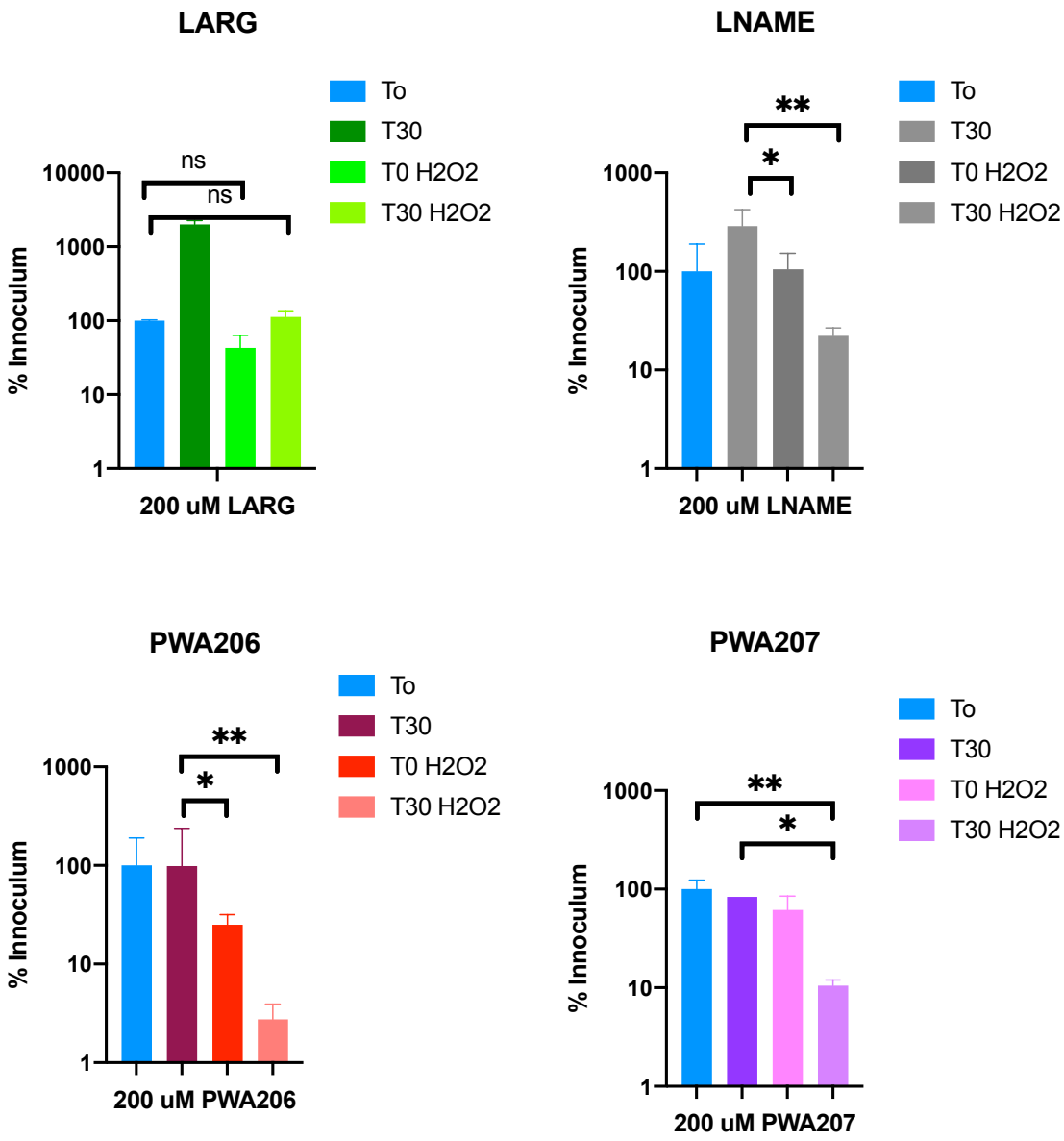

Figure 2.6 – bNOS inhibitors amplify the killing effects of hydrogen peroxide on MRSA. L-ARG treated MRSA recovered fully after 30 minutes(A). LNAME reduced bacterial survival to 22% of the initial inoculum(B). 206 had the greatest effect, reducing the bacteria to 2.75% after 30 minutes(C). 207 also showed efficacy by reducing bacterial survival to 10.5% of the initial inoculum(D).

Table 2.1 Binding constants and IC_{50} values for dual headed inhibitors.

Compound	bNOS	bNOS I218V	bNOS	bNOS I218V	heNOS	hiNOS
	Ks (uM)	Ks (uM)	IC_{50} (uM)	IC_{50} (uM)	IC_{50} (uM)	IC_{50} (uM)
PWA101	32	58.9	40	86	475	143
PWA103	6.3	6.3	6.1	9.2	126	24
PWA115	11.3	ND	12.3	25	>500	39.6
PWA138	22.6	31.9	21.6	63.8	ND	396
PWA150	29.9	23.5	23.1	31.2	>500	435
PW-II-6	2.25	24.6	26.5	228	493	350
PW-II-7	2.3	40.0	28	144	307	318

Table 2.2 – Crystallographic details for each PDB structure

PWA101	6XK3
Wavelength	
Resolution range	34.44 - 1.95 (2.02 - 1.95)
Space group	P 21 21 2
Unit cell	81.2199 95.7998 62.5199 90 90 90
Total reflections	70891 (7070)
Unique reflections	36086 (3566)
Multiplicity	2.0 (2.0)
Completeness (%)	99.23 (99.86)
Mean I/sigma(I)	8.35 (1.89)
Wilson B-factor	30.87
R-merge	0.03551 (0.2747)
R-meas	0.05022 (0.3885)
R-pim	0.03551 (0.2747)
CC1/2	0.997 (0.922)
CC*	0.999 (0.979)
Reflections used in refinement	36004 (3562)
Reflections used for R-free	1998 (198)
R-work	0.1808 (0.2251)
R-free	0.2081 (0.2884)
CC(work)	0.966 (0.933)
CC(free)	0.957 (0.876)
Number of non-hydrogen atoms	3248
macromolecules	2947
ligands	101
solvent	200

Table 2.2 – Crystallographic details for each PDB structure, continued

PWA103	6XK4
Wavelength	
Resolution range	37.06 - 2.13 (2.206 - 2.13)
Space group	P 21 21 2
Unit cell	80.4901 95.05 62.7399 90 90 90
Total reflections	54641 (5332)
Unique reflections	27561 (2689)
Multiplicity	2.0 (2.0)
Completeness (%)	99.75 (99.74)
Mean I/sigma(I)	7.51 (1.69)
Wilson B-factor	33.00
R-merge	0.04911 (0.3799)
R-meas	0.06945 (0.5372)
R-pim	0.04911 (0.3799)
CC1/2	0.997 (0.822)
CC*	0.999 (0.95)
Reflections used in refinement	27536 (2687)
Reflections used for R-free	2000 (196)
R-work	0.2088 (0.3005)
R-free	0.2463 (0.3387)
CC(work)	0.951 (0.860)
CC(free)	0.943 (0.778)
Number of non-hydrogen atoms	3121
macromolecules	2940
ligands	82
solvent	99

Table 2.2 – Crystallographic details for each PDB structure, continued

PWA115	6XK5
Wavelength	
Resolution range	33.7 - 1.87 (1.937 - 1.87)
Space group	P 21 21 2
Unit cell	80.3199 94.9897 61.9498 90 90 90
Total reflections	70558 (6596)
Unique reflections	37828 (3559)
Multiplicity	1.9 (1.9)
Completeness (%)	93.72 (90.75)
Mean I/sigma(I)	7.53 (1.69)
Wilson B-factor	23.42
R-merge	0.04175 (0.322)
R-meas	0.05904 (0.4554)
R-pim	0.04175 (0.322)
CC1/2	0.997 (0.911)
CC*	0.999 (0.976)
Reflections used in refinement	37393 (3551)
Reflections used for R-free	1998 (188)
R-work	0.1972 (0.2704)
R-free	0.2458 (0.3443)
CC(work)	0.961 (0.910)
CC(free)	0.936 (0.788)
Number of non-hydrogen atoms	3236
macromolecules	2940
ligands	93
solvent	203

Table 2.2 – Crystallographic details for each PDB structure, continued

PWA138	6XK6
Wavelength	
Resolution range	37.53 - 1.84 (1.906 - 1.84)
Space group	P 21 21 2
Unit cell	80.16 94.3297 61.9499 90 90 90
Total reflections	81454 (8078)
Unique reflections	41333 (4082)
Multiplicity	2.0 (2.0)
Completeness (%)	99.27 (99.49)
Mean I/sigma(I)	8.26 (1.24)
Wilson B-factor	23.58
R-merge	0.03991 (0.3732)
R-meas	0.05645 (0.5278)
R-pim	0.03991 (0.3732)
CC1/2	0.992 (0.809)
CC*	0.998 (0.946)
Reflections used in refinement	41200 (4064)
Reflections used for R-free	1998 (198)
R-work	0.2009 (0.2918)
R-free	0.2308 (0.3340)
CC(work)	0.962 (0.823)
CC(free)	0.960 (0.833)
Number of non-hydrogen atoms	3199
macromolecules	2940
ligands	85
solvent	174

Table 2.2 – Crystallographic details for each PDB structure, continued

PWA150	6XMC
Wavelength	
Resolution range	37.2 - 1.85 (1.916 - 1.85)
Space group	P 21 21 2
Unit cell	80.887 94.82 61.924 90 90 90
Total reflections	82101 (8017)
Unique reflections	41107 (4022)
Multiplicity	2.0 (2.0)
Completeness (%)	85.97 (70.14)
Mean I/sigma(I)	16.62 (2.06)
Wilson B-factor	31.47
R-merge	0.01449 (0.2981)
R-meas	0.02049 (0.4216)
R-pim	0.01449 (0.2981)
CC1/2	1 (0.94)
CC*	1 (0.985)
Reflections used in refinement	35590 (2856)
Reflections used for R-free	1739 (143)
R-work	0.1969 (0.3247)
R-free	0.2444 (0.4081)
CC(work)	0.969 (0.926)
CC(free)	0.927 (0.915)
Number of non-hydrogen atoms	3143
macromolecules	2940
ligands	94
solvent	109

Table 2.2 – Crystallographic details for each PDB structure, continued

PWA206	6XCX
Wavelength	
Resolution range	37.13 - 2.252 (2.333 - 2.252)
Space group	P 21 21 2
Unit cell	80.67 94.9798 61.79 90 90 90
Total reflections	46089 (4492)
Unique reflections	23115 (2196)
Multiplicity	2.0 (2.0)
Completeness (%)	99.62 (97.34)
Mean I/sigma(I)	14.94 (5.36)
Wilson B-factor	34.56
R-merge	0.02028 (0.09352)
R-meas	0.02868 (0.1323)
R-pim	0.02028 (0.09352)
CC1/2	0.999 (0.987)
CC*	1 (0.997)
Reflections used in refinement	23040 (2194)
Reflections used for R-free	1997 (189)
R-work	0.1804 (0.2171)
R-free	0.2177 (0.3097)
CC(work)	0.967 (0.955)
CC(free)	0.950 (0.849)
Number of non-hydrogen atoms	3146
macromolecules	2940
ligands	96
solvent	110

Table 2.2 – Crystallographic details for each PDB structure, continued

PWA207	6XK8
Wavelength	
Resolution range	37.07 - 2.252 (2.333 - 2.252)
Space group	P 21 21 2
Unit cell	80.599 94.4994 61.9293 90 90 90
Total reflections	46007 (4477)
Unique reflections	23021 (2234)
Multiplicity	2.0 (2.0)
Completeness (%)	99.78 (99.55)
Mean I/sigma(I)	19.62 (8.60)
Wilson B-factor	34.23
R-merge	0.01642 (0.05799)
R-meas	0.02322 (0.08201)
R-pim	0.01642 (0.05799)
CC1/2	0.999 (0.995)
CC*	1 (0.999)
Reflections used in refinement	22983 (2230)
Reflections used for R-free	1999 (194)
R-work	0.1823 (0.2020)
R-free	0.2179 (0.2509)
CC(work)	0.966 (0.953)
CC(free)	0.955 (0.900)
Number of non-hydrogen atoms	3158
macromolecules	2940
ligands	102
solvent	116

Chapter 3

Measuring NO Production and Inhibition *in situ*

Introduction

Nitric oxide synthase (NOS) is a highly conserved heme protein that catalyzes the conversion of L-arginine to L-citrulline and produces the radical oxide species nitric oxide (NO). There are three mammalian isoforms of NOS—neuronal NOS (nNOS) is involved in signaling between brain cells; endothelial NOS (eNOS) participates in regulation of blood pressure in capillaries; and inducible NOS (iNOS) is used by the immune system to fight off pathogens[65]. In addition to the mammalian isoforms, several gram-positive bacterial species also posses a nitric oxide synthase (bNOS) that shares high structural similarity with the mammalian forms[15]. Notably, several virulent strains of bacteria, namely MRSA and *Bacillus anthracis,* use bNOS to help fight off the host immune system and survive during antibiotic treatment[39, 40, 66]. These traits make bNOS a target of particular interest for developing new strategies for combating antibiotic resistant bacterial infections[31, 42].

Measuring nitric oxide production is a difficult proposition given that it is a small highly reactive molecule[67]. Several methods have been used to measure NO with varying degrees of success, often relying on detection of degradation products and not the NO itself[67-69]. In aqueous solutions, NO decays rapidly to nitrite or nitrate over the course of seconds to several minutes, and nitrite/nitrate can be measured colorometrically using the Griess reaction. In a biological setting, NO can quickly react with a variety of materials— from proteins, to unsaturated fatty acids, to DNA and RNA. In this environment, NO's half-life is considerably shorter, and thus it is difficult to accurately measure NO production.

The Lippard group at MIT has recently developed several fluorescent nitric oxide-specific chemical probes[69]. These have been used to measure biologic nitric oxide in many instances, with varying degrees of success. His most notable is the molecule FL2E, which is a cell-trappable version of a NO-specific probe[70]. It has been used to measure small changes in

the production and non-isoform selective inhibition of NO in *Bacillus anthracis* and *Staphylococcus aureus* successfully[71].

Our lab has been working in collaboration with the Silverman group at Northwestern to develop isoform selective nitric oxide synthase inhibitors that work solely against the bacterial isoform[41, 42, 44, 63]. In order to measure the effectiveness of our bNOS selective inhibitors to both enter the cell and inhibit bNOS *in situ*, we attempted to utilize FL2E to setup a high throughput intracellular screen in an engineered bNOS expressing *E. coli* strain.

Materials and Methods

Confocal Imaging of NO production and inhibition – NO production was detected via a cell permeable NO selective fluorescein Cu_2FL2E[70]. Cu_2FL2E specifically reacts with NO to form a fluorescently active adduct that is unable to leave the cell. Late log phase *Bacillus subtilis* (WT and mutants) were protected from light and co-incubated in PBS with both 1 uM Cu_2FL2E and either water (VC) or various concentrations of L-nitroarginine (L-NNA) for 4 hours (37°C, 225rpm). Bacteria were then pelleted and washed with BPS to remove any unused fluorescein and inhibitor. The cultures were concentrated 10-fold by centrifugation and re-suspension in $1/10^{th}$ the normalized volume of PBS. 2-3 uL of the concentrated stocks was plated onto a microscope slide with 2-3 uL of warm 0.5% agarose to immobilize the bacteria for imaging. A coverslip was applied and the edges sealed with clear nail polish. Images were taken as Z-stacks on the Leica SP8 confocal microscope, using the FITC (Excitation 488 nm, emission 515 nm) laser at 2.68% power of 20% power overall. 3-5 images were taken from randomized locations on the slide, and each set of images was saved as an individual .lif file. Data was processed using ImageJ[72]. 10 individual cells were randomly selected from each field of view, and fluorescence measured from that outline. Fluorescence was normalized to the background.

Flow Cytometry Imaging of NO production and inhibition in Bacillus subtilis.

Bacillus subtilis WT, ΔNOS, and ibsNOS strains were plated out on LB agar plates, +/ - 50 ug /mL Spectinomycin for ΔNOS, and ibsNOS selectivity. Individual colonies were used to inoculate 5mL cultures of TB (+/- 50 ug/mL Spectinomycin). These were grown 37°C, 220 RPM shaking until reaching an OD_{600} of 0.5-0.6, and then induced with 1mM IPTG and 400 uM δ-ALA. Bacteria were grown an additional 12-16 hours (overnight) to allow time for the production of high levels of bsNOS. Cells were spun down 4K RPM, 4 Minutes, 4°C. Cells were resuspended in PBS, spun down 4K RPM for 4 Minutes at 4°C., and then resuspended in M9 minimal media, followed by OD_{600} normalization to 1.0. 100 uLs of culture was mixed with inhibitors to achieve the desired concentration and activated FL2E was added at 10 uM (2 uL of 500 uM). The samples were protected from light, and incubated for 1.5 hours at room temperature. Aliquoted samples were then fixed with 1-2% Paramformaldehyde for 20 minutes, and diluted to 1 mL with PBS. Cells were spun down at 14k rpm, 4 minutes, room temperature. Pellets were resuspended in 1 mL PBS, and lightly sonicated (10% amp, 0.3 seconds on, 1.0 seconds off, 3 seconds total time) to separate cells. Samples were run on a Amnis imagingflow cytometer. Gated samples were normalized to the background fluorescence, and mean fluorescence intensities were calculated for the bulk population for each conditions tested.

FL2E Testing with NaHS and a NO donor.

SNAP and NaHS at 5 uM each were combined with 5 uM FL2E and incubated for 45 minutes. Fluoresence was measured using a fluorescence plate reader. Samples were normalized to PBS blanks.

Results and Analysis

To demonstrate therapeutic efficacy of targeting bNOS containing bacteria, we needed an assay to measure functional inhibition of NO production inside of bacterial cells. Historically, the

Griess reaction, has been used as a surrogate for quantifying NO levels by measuring NO_2^-. This assay is acceptable for measuring NO production from purified proteins in solution, but cannot accurately represent the NO production in an intracellular environment because NO_2^- is produced through multiple pathways, NO itself reacts with substrates that do not lead to NO_2^-, and the limit of detection of the reaction itself is too high. In collaboration with the Lippard lab we used a cell-trappable, NO-specific fluorescent probe to measure NO inhibition within live bacterial cells. The absorbance and emission bands are close to GFP, making it easily detectable by multiple methods including microscopy and flow cytometry. Using a strain of *Bacillus subtilis* that had been engineered to overexpress bNOS (ibsNOS) and this newly developed probe, we measured and compared NO production relative to the wild type (WT) bacteria or a strain that lacks the bNOS gene (ΔNOS). After incubating bacteria in the FL2E probe for several hours, the cells were embedded in warm agar and fixed to slides for confocal microscopy using a 488nm laser. The relative object intensity (ROI) of individual cells was measured using ImageJ software. We were initially able to detect a modest difference between WT *Bacillus subtilis* (70 Relative Fluorescence Units (RFU)), ΔNOS (20 RFU) and ibsNOS (80 RFU) (Figure 3.2A). We also measured a 14-fold decrease in fluorescence in the presence of pan-NOS inhibitor L-N^G-Nitroarginine (LNNA) (Figure 3.2B). Given the expected decrease of NO in the presence of an inhibitor and the reduced fluorescence, we now have a method for measuring both the production of NO and any resulting inhibition within bacterial cells.

To perform the assay with higher throughput on a per-cell basis, we measured fluorescence intensity at 518nm using the AMNIS MK II imaging flow cytometer. We obtained good signal differentiation between the ΔNOS, WT, and ibsNOS cells. In comparison to the confocal microscopy experiments, we saw an increase in averaged Mean Fluorescence Intensity (MFI) per bacterial cell. MFIs for WT were found to be close to the range for ΔNOS at around 2581 and 2155, with the ibsNOS having the strongest average signal at 3380 (Figure 3.2C and

3.2D). Surprisingly, the addition of NOS inhibitors resulted in an *increase* in signal presumably indicative of increased NO production.

To explain this increase signal, we had to consider several options. Either the bacteria were producing more NO via upregulation of bNOS, or there was some other molecule interfering with the probe. The first case is highly unlikely, as we see a dose dependent increase in signal relative to the amount of LNNA added. Given the lack of additional substrate, it is highly unlikely that this would be the case. Others have noted that when NO production in bacteria is inhibited, H_2S production is increased to compensate[73]. When reviewing the specificity of FL2E, we noted that H_2S had not been tested with the other small molecules[70]. In order to test if FL2E was activated by H_2S, we used an H_2S donor (NaHS), and an NO donor (SNAP) in PBS. Fascinatingly, H_2S showed a large increase in signal with FL2E over SNAP (Figure 3.4). Thus, FL2E may not be as selective for NO as previously thought.

Discussion

The accurate measurement of NO in biological samples has long been a difficult problem for researchers to address. Most of the methods utilized rely on secondary degradation products of NO decay. With the development of NO specific fluorometric probes, we were finally able to begin measuring NO more directly[70]. We intended to use the probes to develop a high throughput model for screening the efficacy of our inhibitors ability to both enter the cell, and inhibit bNOS production of NO. Instead, we found that the NO selective probes were also detecting H_2S production.

The mechanism by which FL2E is activated by H_2S is unknown. It is likely due to HS- affinity for metal ions, where it will attack the copper in the active FL2E structure (Scheme 3.1). Further study here is required. Regardless, we are still in need of an effective NO selective probe that can be trapped in cells. This would aid immensely in being able to measure the ability of NOS selective inhibitors to effectively enter and inhibit NOS in a more biologically relevant system.

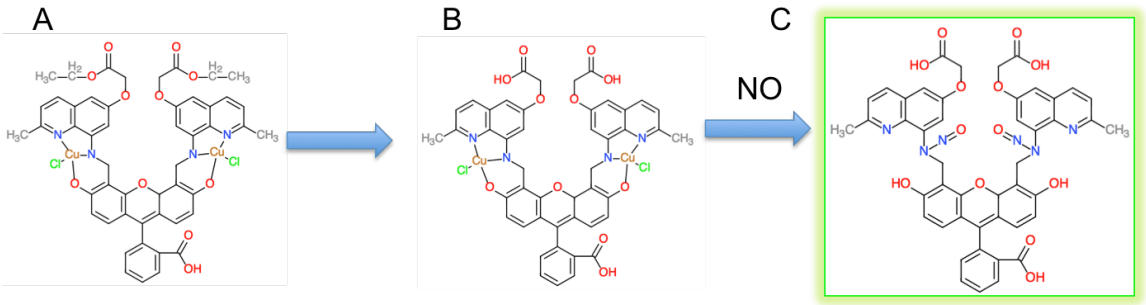

Scheme 3.1 – A) FL2E is activated with $CuCl_2$ becoming weakly fluorescent. B) Upon entering the cell, naturally occurring esterases cleave off the ether moiety making FL2E too electronegative to pass back through the cell membrane. C) Upon contact with NO, the Cu is forced out, the NO is irreversible bound and the molecule becomes fluorescently active.

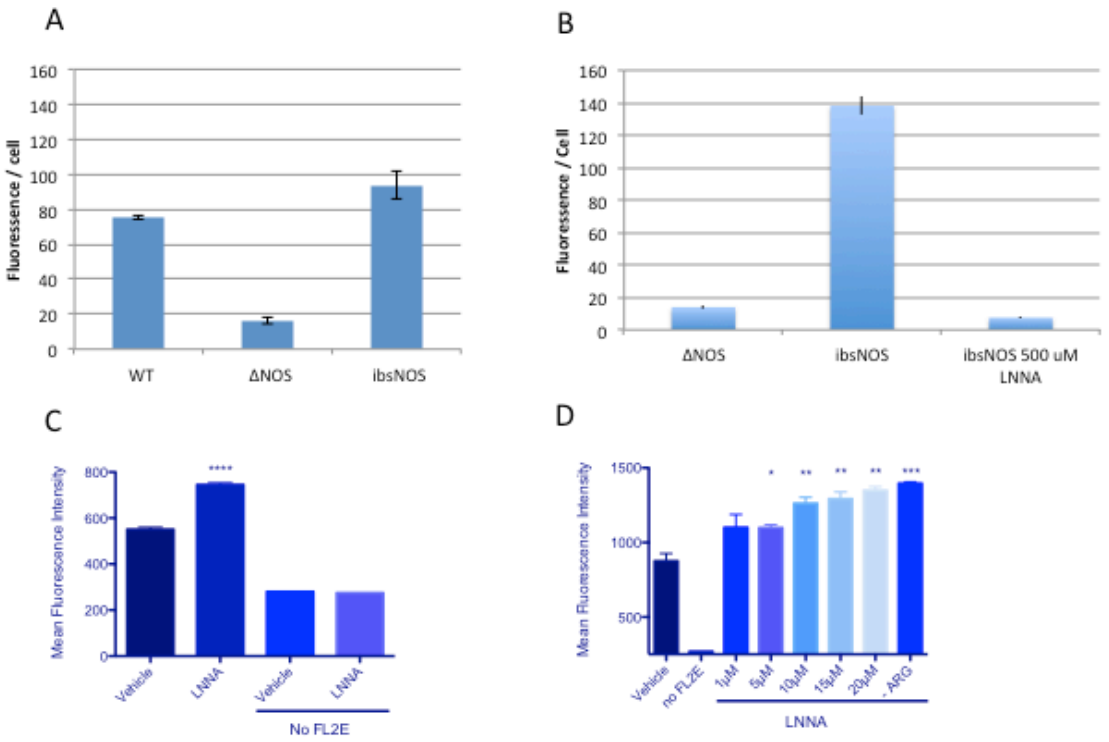

Figure 3.1 Confocal microscopy measurement of bacterial NO via FL2E in *Bacillus subtilis*. A) Difference in fluorescence by microscopy between Wild Type (WT), a NOS deficient strain (ΔNOS), and a strain engineered to overproduce bsNOS (ibsNOS) B) Inhibition of bNOS by LNNA at 500 uM as measured by confocal microscopy C) Flow Cytometry measurements of NO production ΔNOS and D) ibsNOS. LNNA Appears to be increasing signal in a dose-dependent manner. * P<0.05, ** P<0.01, *** P<0.005, **** P<0.001 Significance calculated by student's *t* test as compared to vehicle control.

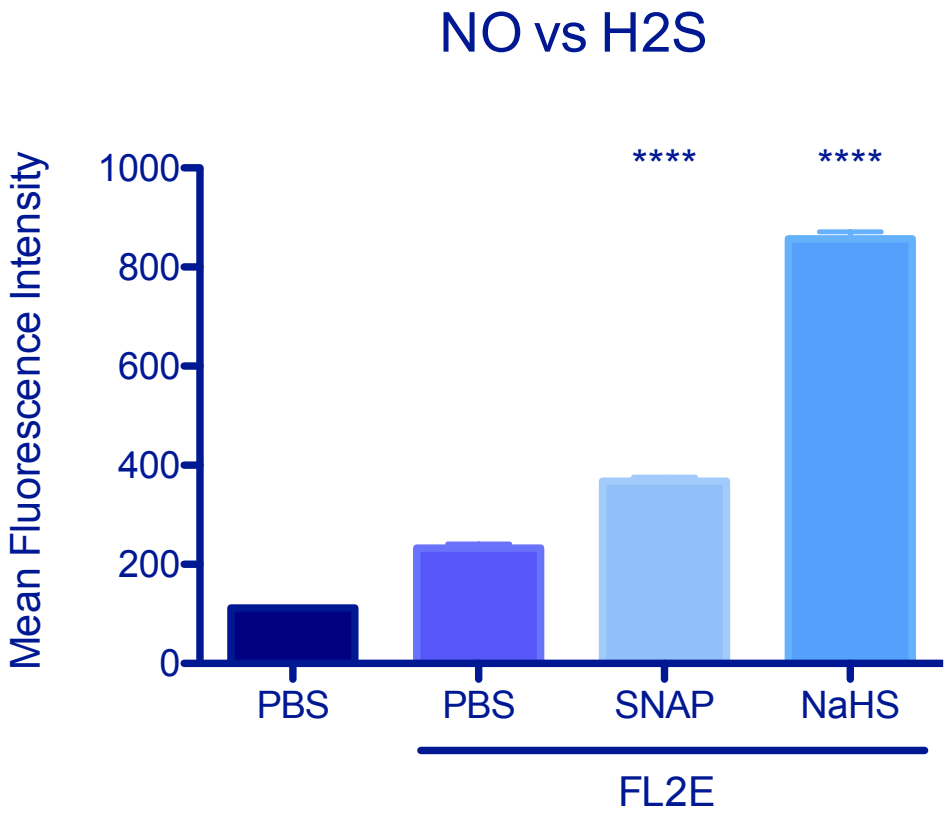

Figure 3.2 Testing of FL2E selectivity for NO with NO donor SNAP and H_2S donor NaHS. 5 mM FL2E was incubated with 5 mM SNAP or NaHS for 5 minutes at room temperature. * P<0.05, ** P<0.01, *** P<0.005, **** P<0.001 Significance calculated by student's *t* test as compared to vehicle control.

Chapter 4

Structural Studies of *Staphylococcus aureus* Cystathionine γ-Lyase and Cystathionine β-Synthase

Introduction

Sulfur is an important biological element that is able to cycle through oxidation states ranging from -2 (in hydrogen and metal sulfides) to +6 (in sulfate)[74]. Most commonly associated with its distinctive 'stinky egg' smell, H_2S is a colorless gas found in biogeochemical cycles as an important energy source for microbes. H_2S is considered a weak acid with pK_{a1} of 6.9 and pK_{a2} of >12 and a solubility in the 80 mm range at physiological temperatures. At a pH of 7.4, it exists as a 3:1 ratio of HS^- : H_2S. This makes it less cell permeable compared to its chemical gasotransmitter relatives nitric oxide and carbon dioxide. For the purposes of this chapter, we will refer to this pool of free sulfide as H_2S. Like other gasotransmitters, H_2S is a dichotomous molecule that is toxic at high concentrations but exhibits important biological functional properties at lower concentrations.

H_2S Production

H_2S has been hypothesized to be primarily produced from the desulfhydration of cysteine, a reaction catalyzed by a pyridoxal phosphate (PLP) containing family of enzymes. In bacteria, there are two ways of generating cysteine: the *de novo* synthesis method from a two step process with L-serine-O-acteyltransferase(SAT/CysE) and O-acetyl-L-serine sulfhydrylase (OASS/CysK), and the reverse transulfuration pathway, where cysteine is generated via cystathionine beta synthase (CBS) and cystathionine gamma-lyase (CSE or CGL)[75, 76]. Interestingly, human CBS and CSE can produce H_2S from the desulfurhydration of cysteine, as well as several other reactions[75]:

CBS: 1. Cysteine + Homocysteine -> Cystathionine + H_2S

2. Cysteine + Cysteine -> Lanthionine + H_2S

CSE: 1. Cysteine + Homocysteine -> Cystathionine + H_2S

2. Cysteine + Cysteine -> Lanthionine + H_2S

3. Homocysteine -> α-ketobutyrate + NH_3^+ + H_2S

4. Homocysteine + Homocysteine -> Homolanthionine + H_2S

H_2S is also formed nonenzymatically from polysulfides[77]. Another pathway in mammals to produce H_2S is the mercaptopyruvate sulfur transferase (MST) and cysteine transferase (CAT). Interestingly, the pathway used to produce H_2S is thought to be dependent on the environmental constraint of the cell types: MST/CAT operate under mostly normoxic conditions, whereas CBS/CSE are upregulated during times of oxidative stress to supply cysteine for glutathione replenishment[78, 79].

H_2S Function

In mammals, H_2S is involved in regulation of several key biological processes including vasorelaxation, cardioprotection, neurotransmission, and anti-inflammatory actions in the gut[80-82]. Disregulation of H_2S production is associated with a number of negative health outcomes, including homocysterinia, seizures, low blood pressure, and cancer[83, 84]. H_2S is able to induce a state of suspended animation in mammals via reversibly inhibiting cytochrome c oxidase and thus lowering the metabolic rate[85]. H_2S is also involved in post-translational modification of proteins in a manner similar to nitric oxide[86]. It is thought to either provide protection from oxidative damage of cysteines by offering sacrificial S atoms to be oxidized over the amino acid linked sulfur[87].

Cysteine Metabolism

H_2S is oxidized in a series of steps to persulfide, then sulfite, thiosulfate, and finally sulfate. The conversion of H_2S to a protein bound persulfide is catalyzed by a mitochondrial membrane flavoprotein known as SQR. The electron accepter for the reaction is ubiquinone, which links H_2S metabolism to the electron transport chain by transferring electrons to complex III of the electron transport chain. Then, either low molecular weight thiols (such as glutathione or bacillithiol) transfer the persulfide group from SQR to a sulfur dioxygenase, or the sulfur dioxygenase and sulfer transferase convert the persulfide from SQR to sulfite and then thiosulfate. The exact mechanism has not yet been conclusively determined. Interesting to consider is that while low levels of H_2S stimulate oxygen consumption by promoting electron transfer through the electron transport chain, higher levels (~20 uM or greater) inhibit the mitochondrial respiratory machinery[88].

Redox Stress and Reactive Sulfur Species

With regards to redox stress, H_2S plays several different roles. In the protection of cysteine residues, H_2S is only able to attack the cysteine after the cysteine sulfur is rendered sufficiently electrophilic by being oxidized by H_2O_2[89]. This S-sulfhydration is thought to have proteomic effects similar in some ways to protein phosphorylation, setting off a signaling cascade as a response mechanism to ROS stress[87, 90, 91]. This protection is thought to provide relief from higher level oxidation states of sulfur, which require energy input from thioredoxins and other similar proteins[92]. H_2S is not the only means by which this protection is inferred: small molecular weight thiols like glutathione also provide similar protection.

H_2S in Bacteria

In bacteria, the role of H_2S is not as well understood: it has been associated with resistance to antibiotics and ROS stress, transcriptional signaling, as well as being a virulence factor. Nudler *et al.* described the protective effect of endogenous H_2S production by bacteria as being a critical component of antibiotic resistance(citation). Using a pan-PLP inhibitor and a

specific sulfur gamma-lyase inhibitor combination, they were able to show an increased susceptibility of methicillin resistant *Staphylococcus aureus*, *Psuedomonas aeruginosa,* and *Bacillus anthracis* to killing by antibiotics and ROS stress from H_2O_2[93]. There exist only a few structures for human and yeast cystathionine beta synthase and cystathionine gamma lyase, whereas there are several crystal structures for related proteins in the same PLP family[94-96]. Currently there is one bacterial putative CBS protein structure (PDBid: 4OFX) from *Coxiella burnetii* (No pubmed paper associated), and several structures of a cystathionine gamma-lyase like protein from *Xanthomonas oryzae*. The lack of structural knowledge for this H_2S-generating pathway in bacteria not only provides an open field of study but also has broad implications for novel antibiotic targeting.

Pathogenic bacteria have several potential ways of deriving H_2S from cysteine[73]. The method employed is likely dependent upon the available substrates of their local environment[9]. In the context of survival within a human host, it would make sense that the bacteria would coopt the available resources and sequester host metabolites for their own benefit. In this case, the reverse transulfuration pathway makes the most sense as a likely target as it is the only method of cysteine metabolism available to mammals[75]. *Staphyloccus aureus* is a notorious pathogen that colonizes over 30% of the population in the U.S. and is a leading cause of death from infectious bacteria[97]. *Staphyloccus aureus* has become resistant to many commonly used antibiotics, and some very pathogenic strains (USA300) are able to survive the oxidative burst from neutrophils and macrophages via an unknown mechanism[9, 29]. For combating *Staphlococcus aureus,* targeting CBS and CSE could have therapeutic potential. Following short term (10 min) exposure to H_2O_2, *Staphlococcus aureus* upregulates expression of CBS and CSE more than 10 fold within 10 minutes[93]. At this early time point, bacteria are repairing damage induced by oxidative stress and deactivating oxygen radicals, but haven't yet reached the point where they can resume rapid growth. CBS/CSE transcription decreases rapidly once the bacteria resume rapid growth, indicating they are essential only for protection and recovery from oxidative burst events and not

for normal cell function. CBS and CSE have been shown to be important proteins for other pathogens that survive harsh intracellular environments including macrophages[98, 99]. Namely, CBS was shown to be important for the intracellular survival of *Trypansoma* and *Leishmania* species[100]. In addition, CBS is detectable in *Mycobacterium tuberculosis* (rv1077) only when the bacterium is within the phagosomal compartment of macrophages further implying a purpose for survival from oxidative stress[101]. Given that a large component of MRSA persistent infection is ascribed to its ability to survive phagocytosis and ROS production from the human immune system[9], identifying and targeting the means by which MRSA survives could be of great clinical interest in an age with fewer effective treatment methods[102].

By studying the structural differences of bacterial and human CBS and CSE, we may be able to develop targeted therapeutics to inhibit the bacterial isoform selectively. To that end, here we present the structural characterization of saCSE and the purification of saCBS. We also discuss important similarities and differences between our structural analysis of saCSE and existing structures of huCSE.

Materials and Methods

Gene Expression and Purification

saCBS (SAUSA300_0359) and saCSE(SAUSA300_0360) genes were synthesized by Genewiz. saCBS was codon optimized for expression in *E. coli* and had a thrombin digestable GSH tag on the N terminus end, and inserted into a pGEX-4T plasmid. saCSE was codon optimized for expression in *E. coli* , and had a thrombin digestible 6x His tag added to the N terminal end, and was inserted into a pET-28a plasmid.

The plasmids were heat shocked into *E. coli* C41 cells. Individual colonies were selected and grow, and sequenced to confirm gene presence.

Cells were grown in 1L cultures to an OD_{600} of 0.7, and protein expression was induced with 1mM IPTG. After 24 hours of growth at 20C, 200 RPM, bacteria were pelleted by repeated rounds of centrifugation, 4k RPM, 4°C, 10 minutes. Pellets were frozen at -80 C. Pellets were

resuspended in lysis buffer: saCSE 25 mM Tris (7.5) 300 mM NaCl, 15 mM imidazole and 3mM BME. saCBS: 1x PBS (7.8). Cells were lysed via high pressure liquid homogenization. Lysate was separated from insoluble cell debris via centrifugation at 15000 rpm, 4°C for 45 minutes. saCSE was purified using a Ni affinity column, the poly his tag was cleaved using thrombin (1 U / mg saCSE) overnight at 20°C. Uncleaved protein was separated from cleaved by running the mixture over the regenerated Ni affinity column. The cleaved protein was concentrated to 20 mg/mL and then purified further using gel filtration size exclusion. 1 mL fractions were collected, and the purest fractions as determined by gel filtration were combined and concentrated to a final concentration of 30 mg/mL in 25 mM Tris (7.5) and 300 mM NaCl, 3% Glycerol.

Crystallization

Initial crystallization conditions were discovered from crystal screens, and saCSE yielded small crystals of space group $I4_122$ in 100mM Bis Tris (6.5) and 2M ammonium sulfate at ambient temperature. Crystals were grown by mixing equal amounts of protein (25 mg/ml and reservoir solution (100 mM BisTris 6.5 and 2M ammonium sulfate) in vapor diffusion hanging drops. Optimization of these conditions led to 9 mg/mL saCSE in 100 mM Bis Tris (6.5) and 2M ammonium sulfate. Crystals grew as large Bi-tetrapyramidal clear crystals after 72 hours. X-ray diffraction data were collected on individual crystals at the Advnaced Light Source (Berkeley, CA). Data frames were indexed and integrated using MOSFLM[46]. Index data sets were scaled using Aimless. Structure was solved using molecular replacement and huCSE as a search model (PDBID: 2MNP) Structure factors were initially refined using PHENIX[51]. COOT was used to build the model and PyMOL (Version 2.0.5, Schrödinger, LLC) was used to create figures[52]. Data collection and refinement statistics are listed in Table 4.1.

Results and Analysis

Purification and Crystallization. After identification of the putative saCBS and saCSE, we tested a variety of *E. coli* cell types and found that they both expressed best in C41s. Initial expression tests showed that 24 hours post induction of overexpression yielded the largest quantity of

protein, with quantities degrading as time progressed. Our initial solubility conditions for buffers for purification were loosely based off of similar conditions that were used for huCSE, with some slight modifications [95]. Nickel Affinity chromatography yielded relatively pure protein, with purity improving after thrombin cleavage and an additional run through the column. Size exclusion yielded the purest fractions of protein, which were concentrated and used to set up hanging drop crystal trays (Figure 4.3). We initially discovered two conditions which yielded crystals: 100mM Bis Tris (6.5) and 2M ammonium sulfate, and 60% tascimate at pH 6.5. Further optimization led to the adoption of 9 mg/ml of protein in a 4uL drop of 100 mM Bis Tris (6.5) and 2 M Ammonium Nitrate as a crystallization condition. After 72 hours, enormous clear bipyramidal crystals of space group $I4_122$ appeared(Figure 4.4). Initial attempts to cryoprotect the crystals in 100 mM Bis Tris (6.5) and 2M Ammonium Sulfate and 20+% Glycerol cracked and destroyed the crystals. We were able to find a suitable cryoprotectant in the form of 100 mM BisTris 6.5 and 3.4 M Ammonium Sulfate. Crystals were quickly soaked in the cryoprotectant and then immediately flash frozen in liquid nitrogen.

Sequence and Structural Similarity to huCSE

saCSE and huCSE share 45% sequence identity with almost no gaps (1%). saCBS and huCBS have 36% identity and 10% gaps, mostly due to extra domains associated with huCBS. Structurally, huCSE and saCSE are almost identical, with an RMS of 0.87Å. Despite the profound similarity, there are subtle differences between the two. In addition, our saCSE structure provides a clearer picture on how the N-terminal regions helps to form the biologicially relevant tetrameric structure (Figures 4.5 and 4.6). saCSE and huCSE form tetramers within the unit cell of the crystal structure, with each monomer consisting of an α/β/α fold, a seven stranded mixed β-sheet which is surrounded on both sides by eight α-helices (Figure 4.5). The central β-sheet is mostly parallel, with only one strand being anti-parallel to the whole sheet. The second β-sheet is in a four strand antiparallel configuration with 3 α-helices on one side of it.

saCSE is an open conformation compared to huCSE's closed conformation

saCSE appears to have adopted a more open conformation as compared to the huCSE, with the Ala_{343}-Glu_{350} helix being between 4 and 6 Ångstroms from the equivalent Lys361-Leu_{367} helix in the huCSE. This might be due to the active site of saCSE not having a PLP cofactor bound to the active site Lysine (Figures 4.7, 4.8). Instead, saCSE has a phosphate or sulfate group bound at the same place that the phosphate of the PLP binds in huCSE (Figure 4.8). The movement of this helix allows the active site saCSE Tyr_{99} to adopt a different conformation than the equivalent Tyr_{441} of huCSE (Figures 4.6-8). This Tyrosine is crucial for catalysis[95] and enzyme turnover. Further crystallization experiments with PLP and substrate with saCSE should be performed to determine if PLP not being bound is the cause of this structural shift.

It would be interesting to see if PAG (a PLP pan inhibitor) is able to bind to saCSE in a similar way as it does to huCSE, and thus cause inhibition via steric hindrance[95].

Future Directions

Many questions remain with regards to saCSE and saCBS: How well do they produce H_2S? How well do they bind different substrates? Are there sufficient differences in and around the active site in order to begin designing an bacterial CSE/CBS isoform selective inhibitor? Our lab is currently working on answering these questions.

A major problem for developing PLP inhibitors comes from PLP homology. The active sites are very similar, and even single amino acid mutations can cause a shift in preference for the type of reaction catalyzed by PLP[75]. Developing selective inhibitors for PLP enzymes will open up a whole new range of druggable targets.

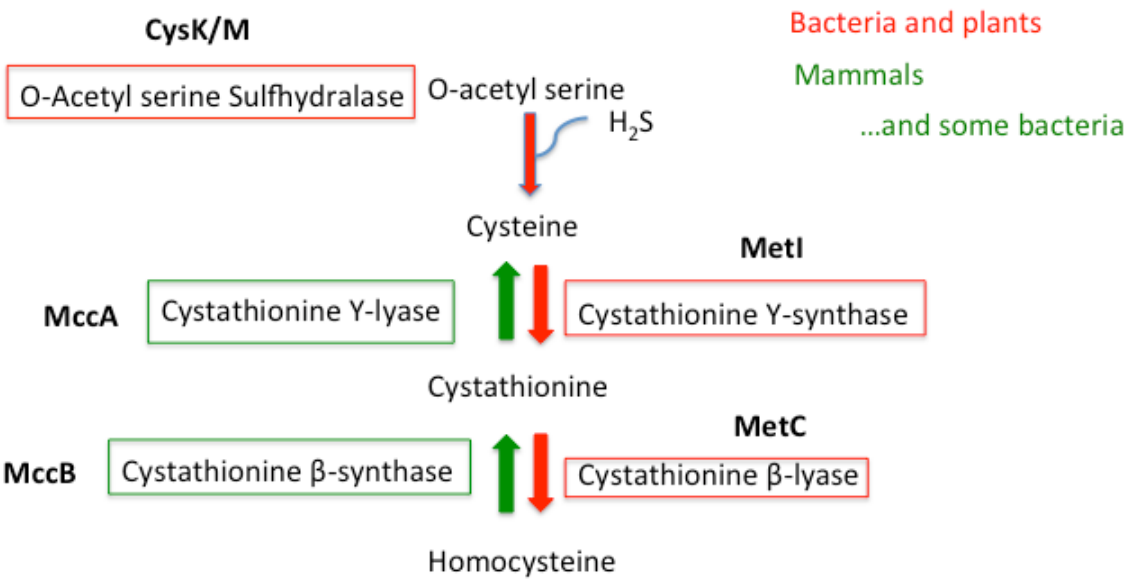

Scheme 4.1 – Pathways of H_2S production. Two primary pathways are the O-Acetyl Serine Sulfhydrase (OASS in red) or the reverse Transulfuration Pathway (Green).

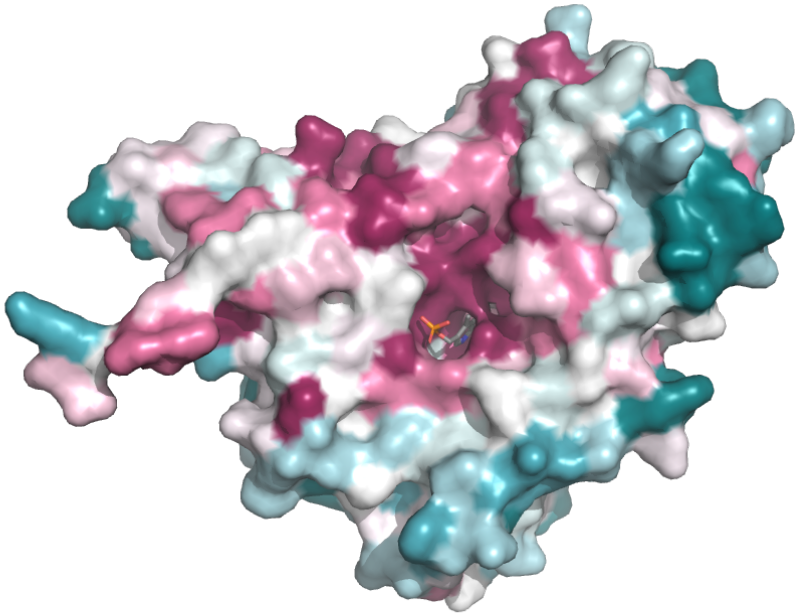

Figure 4.1 Conservation of sequence for CSE proteins based off of huCSE (2NMP) calculated using CONSURF. Red are more conserved amino acids, blue are less conserved. The active site of CSE, with PLP in orange and grey is highly conserved across species.

```
Query: None Query ID: lcl|Query_9315 Length: 380

>unnamed protein product
Sequence ID: Query_9317 Length: 403
Range 1: 21 to 395

Score:315 bits(808), Expect:8e-110,
Method:Compositional matrix adjust.,
Identities:171/376(45%), Positives:246/376(65%), Gaps:4/376(1%)

saCSE  5    TKLIHGGHTTDDYTG-AVTTPIYQTSTYLQDDIGDLRQGYEYSRTANPTRSSVESVIATL  63
            T+ IH G   + +T  AV  PI  ++T+ Q   G    G+EYSR+ NPTR+ +E  +A L
huCSE  21   TQAIHVGQDPEQWTSRAVVPPISLSTTFKQGAPGQ-HSGFEYSRSGNPTRNCLEKAVAAL  79

saCSE  64   ENGKHGFAFSSGVAAISAVVMLLDKGDHIILNSDVYGGTYRALTKVFTRFGIEVDFVDTT  123
            +  K+  AF+SG+AA   +  LL  GD II   DVYGGT R   +V + FG+++ FVD +
huCSE  80   DGAKYCLAFASGLAATVTITHLLKAGDQIICMDDVYGGTNRYFRQVASEFGLKISFVDCS  139

saCSE  124  HTDSIVQAIRPTTKMLFIETPSNPLLRVTDIKKSAEIAKEHG-LISVVDNTFMTPYYQNP  182
                +  AI P TK+++IETP+NP  +V DI+  A I  +HG +I VVDNTFM+PY+Q P
huCSE  140  KIKLLEAAITPETKLVWIETPTNPTQKVIDIEGCAHIVHKHGDIILVVDNTFMSPYFQRP  199

saCSE  183  LDLGIDIVLHSATKYLGGHSDVVAGLVATSDDKLAERLAFISNSTGGILGPQDSYLLVRG  242
            L LG DI ++SATKY+ GHSDVV GLV+ + + L  RL F+ NS G +  P D YL  RG
huCSE  200  LALGADISMYSATKYMNGHSDVVMGLVSVNCESLHNRLRFLQNSLGAVPSPIDCYLCNRG  259

saCSE  243  IKTLGLRMEQINRSVIEIIKMLQAHPAVQQVFHPSIESHLNHDVHMAQADGHTGVIAFEV  302
            +KTL +RME+  ++ + + + L+++P V++V +P + SH  H++   Q  G TG++ F +
huCSE  260  LKTLHVRMEKHFKNGMAVAQFLESNPWVEKVIYPGLPSHPQHELVKRQCTGCTGMVTFYI  319

saCSE  303  KNT-ESAKQLIKATSYYTLAESLGAVESLISVPALMTHASIPADIRAKEGITDGLVRISV  361
            K T + A+  +K    +TLAESLG  ESL  +PA+MTHAS+  + R   GI+D L+R+SV
huCSE  320  KGTLQHAEIFLKNLKLFTLAESLGGFESLAELPAIMTHASVLKNDRDVLGISDTLIRLSV  379

saCSE  362  GIEDTEDLVDDLKQAL  377
            G+ED EDL++DL QAL
huCSE  380  GLEDEEDLLEDLDQAL  395
```

```
Query: saCBS |MITYDLIGNTPLVLLEHYSDDKVKIYAKLEQWNPGGSVKDRLGKYLVEKAIQEGRVRAGQ Query
ID: lcl|Query_8083 Length: 244

>huCBS |MPSETPQAEVGPTGCPHRSGPHSAKGSLEKGSPEDKEAKEPLWIRPDAPSRCTWQLGRPA
Sequence ID: Query_8085 Length: 491
Range 1: 81 to 346

Score:145 bits(365), Expect:5e-45,
Method:Compositional matrix adjust.,
Identities:96/269(36%), Positives:142/269(52%), Gaps:29/269(10%)

saCBS  1    TIVEATAGNTGIGLAIAANRHHLKCKIFAPYGFSEEKINIMIALGAEVSRTSQSEGMHGA  60
            TI+E T+GNTGIGLA+AA      +C I   P   S EK++++ ALGAE+ RT  +
huCBS  81   TIIEPTSGNTGIGLALAAAVRGYRCIIVMPEKMSSEKVDVLRALGAEIVRTPTNARFDSP  140

saCBS  61   Q----LAARSYAEKYGAVYMNQFESEHNPDTYFHTLGPELTSALQQ----IDYFVAGIGS  112
            +    +A R   E   +  ++Q+ +  NP  ++ T   E+   LQQ    +D  VA +G+
huCBS  141  ESHVGVAWRLKNEIPNSHILDQYRNASNPLAHYDTTADEI---LQQCDGKLDMLVASVGT  197

saCBS  113  GGTFTGTARYLKQHHVQC--YAVEPEGSVL------NGGPAHAHDTEGIGSEKWPIFLER  164
            GGT TG AR LK+    C    V+PEGS+L      N      ++ EGIG +  P  L+R
huCBS  198  GGTITGIARKLKEKCPGCRIIGVDPEGSILAEPEELNQTEQTTYEVEGIGYDFIPTVLDR  257

saCBS  165  RLVDGIFTIKDQDAFRNVKSLAINEGLLVGSSSGAALQGALNLKAQLSEG-TIVVVFPDG  223
             +VD  F   D++AF   + L   EGLL G S+G+ +  A+    +L EG   VV+ PD
huCBS  258  TVVDKWFKSNDEEAFTFARMLIAQEGLLCGGSAGSTVAVAVKAAQELQEGQRCVVILPDS  317

saCBS  224  ---------SDRYMSKQIFNYEENNNEQE  243
                     SDR+M ++ F  EE+  E++
huCBS  318  VRNYMTKFLSDRWMLQKGFLKEEDLTEKK  346
```

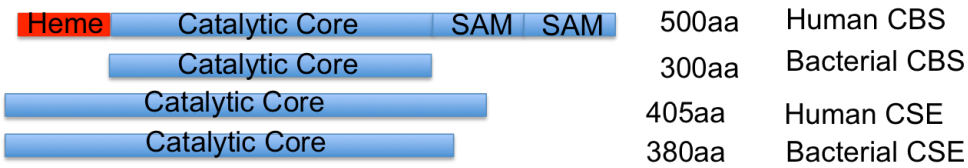

Figure 4.2 – Sequence alignment for CSE and CBS from *Staphylococcus aureus* and *Homo sapiens*.

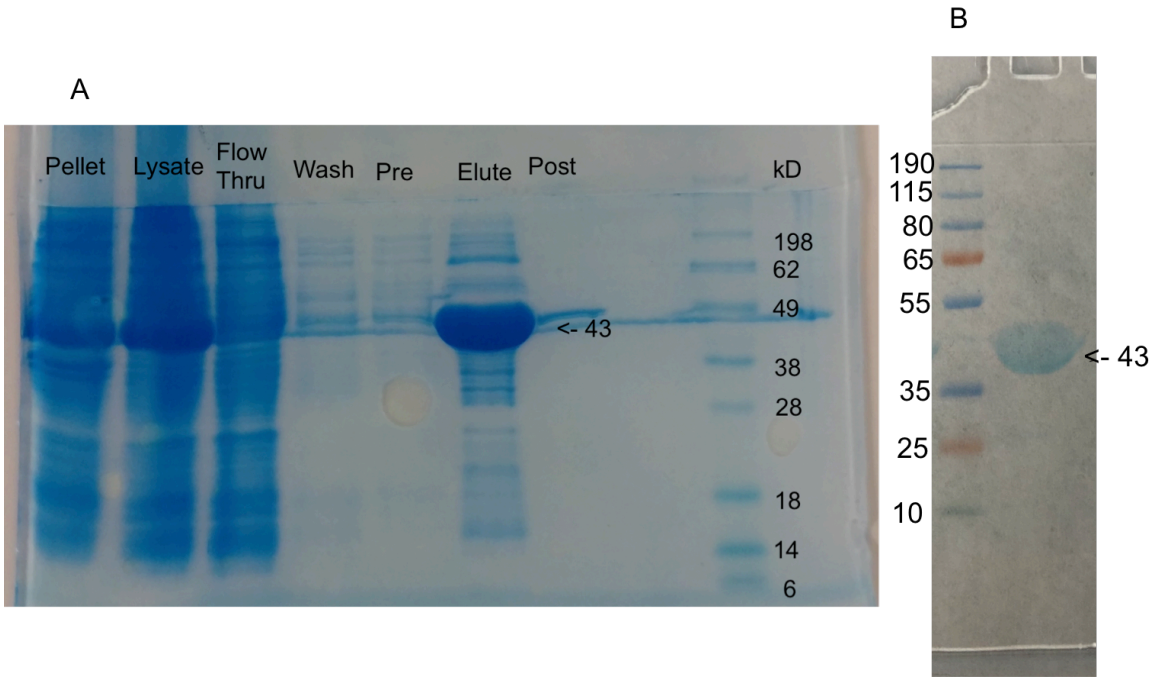

Figure 4.3 – Electrophoresis gels of saCSE purification. A) Ni affinity column B) Size exclusion final combined fraction showing quite pure protein.

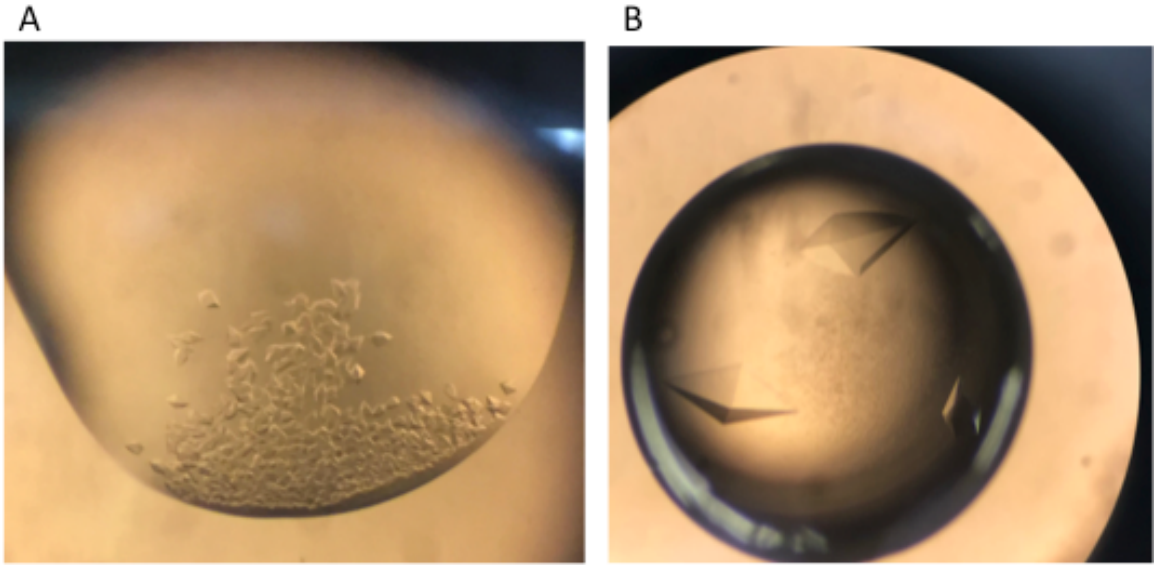

Figure 4.4 – Crystallization of saCSE. A) Initial hit from crystal screen. saCSE at 12.5 mg/ml in 100 mM Bis Tris pH 6.5 and 2M Ammonium Sulfate. B) Optimized saCSE crystals at 9 mg/ml in 100 mM Bis Tris pH 6.5 and 2M Ammonium Sulfate grow for 72 hours.

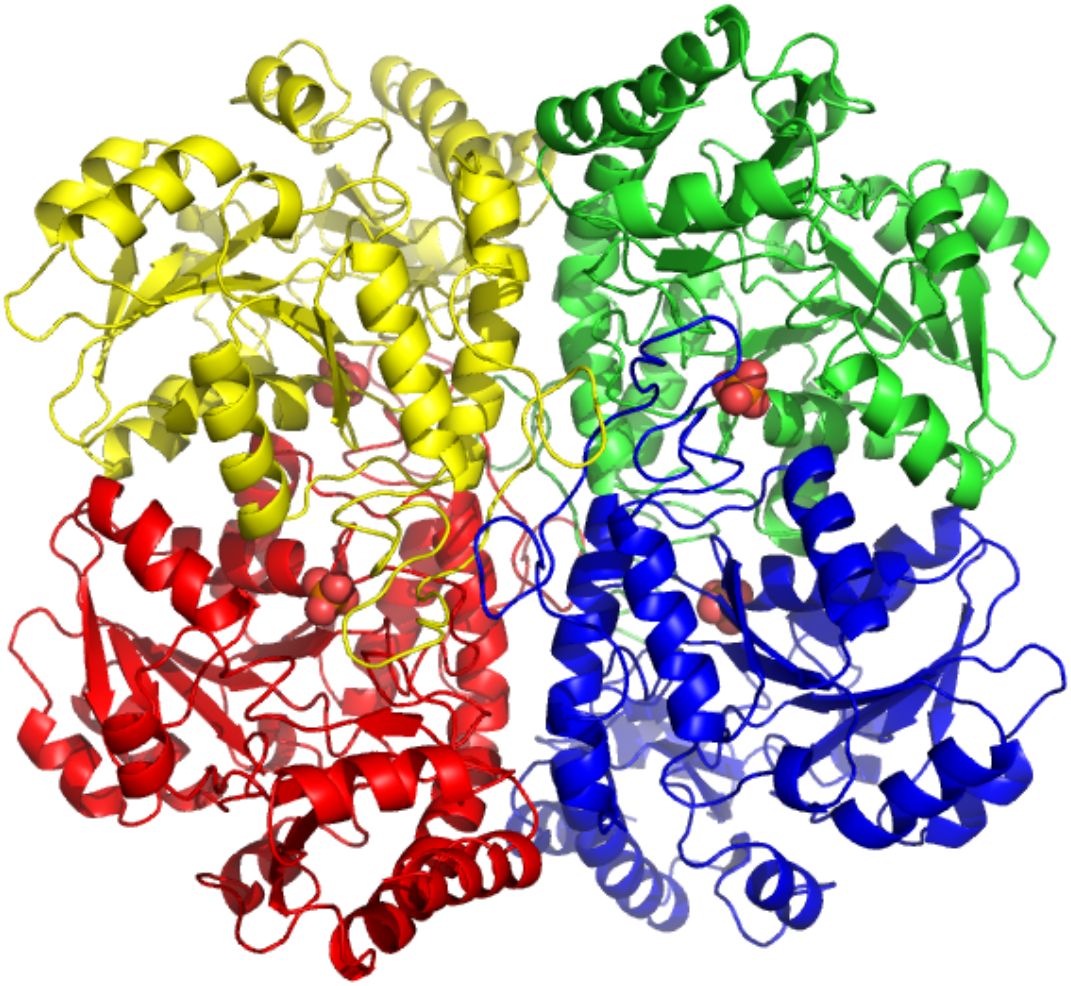

Figure 4.5 – saCSE forms into a tetramer within the unit cell of the crystal structure. The N-terminal loop allows for contacts between monomers.

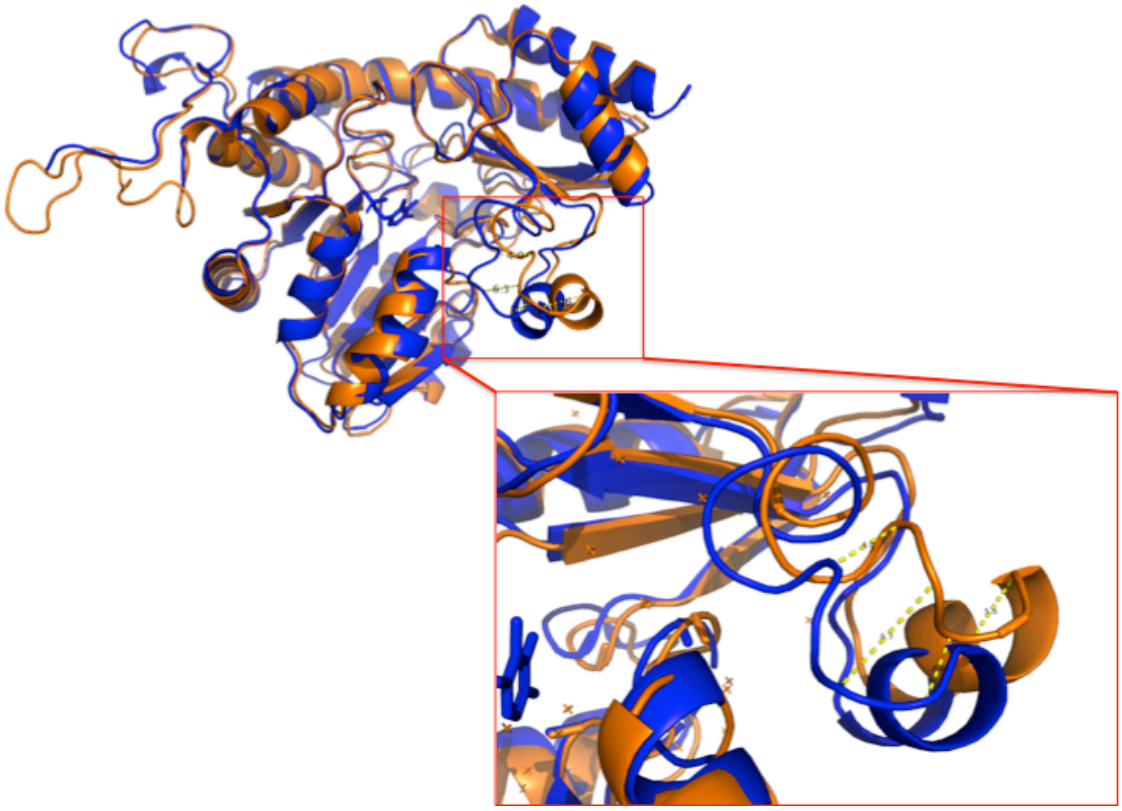

Figure 4.6 - Overlay of saCSE (Orange) and huCSE (Blue PDBid: 2NMP) monomers. saCSE has adopted a more open conformation by moving the highlighted helix out and away from the active site.

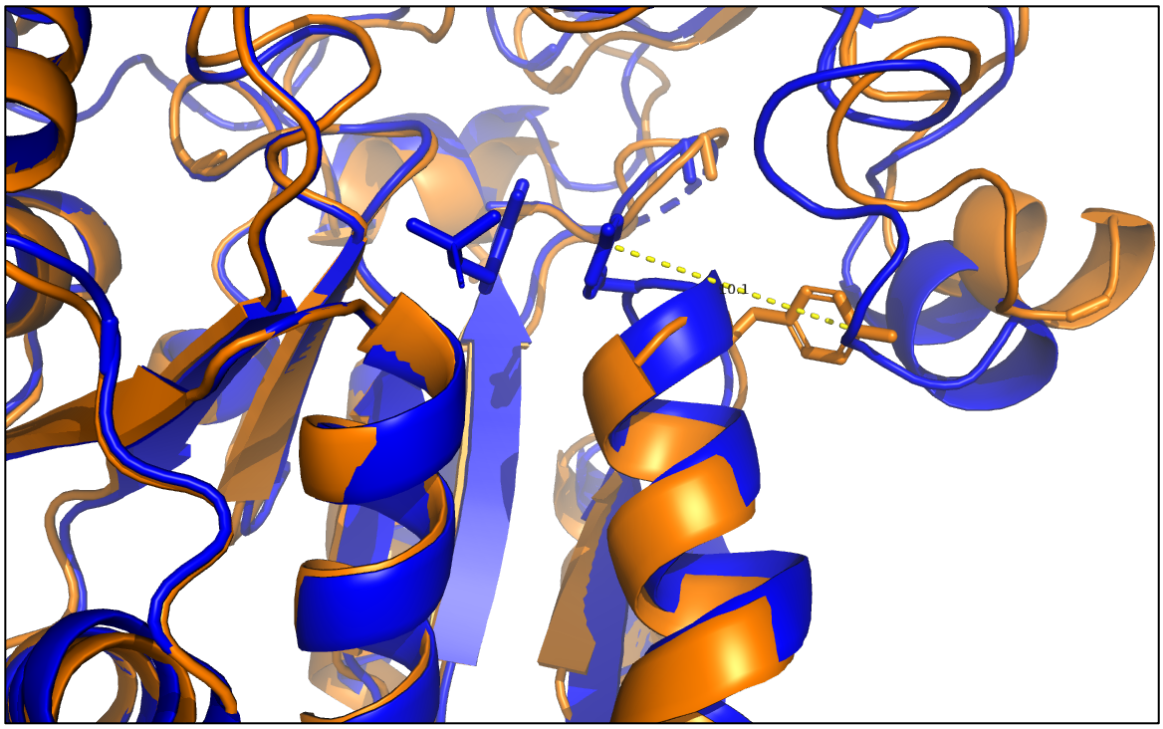

Figure 4.7 - Movement of active site Tyrosine (saCSE in orange, huCSE in blue). The movement of the outer helix in saCSE allows space for this Tyrosine to adopt an alternate conformation and move 10 Ångstroms away.

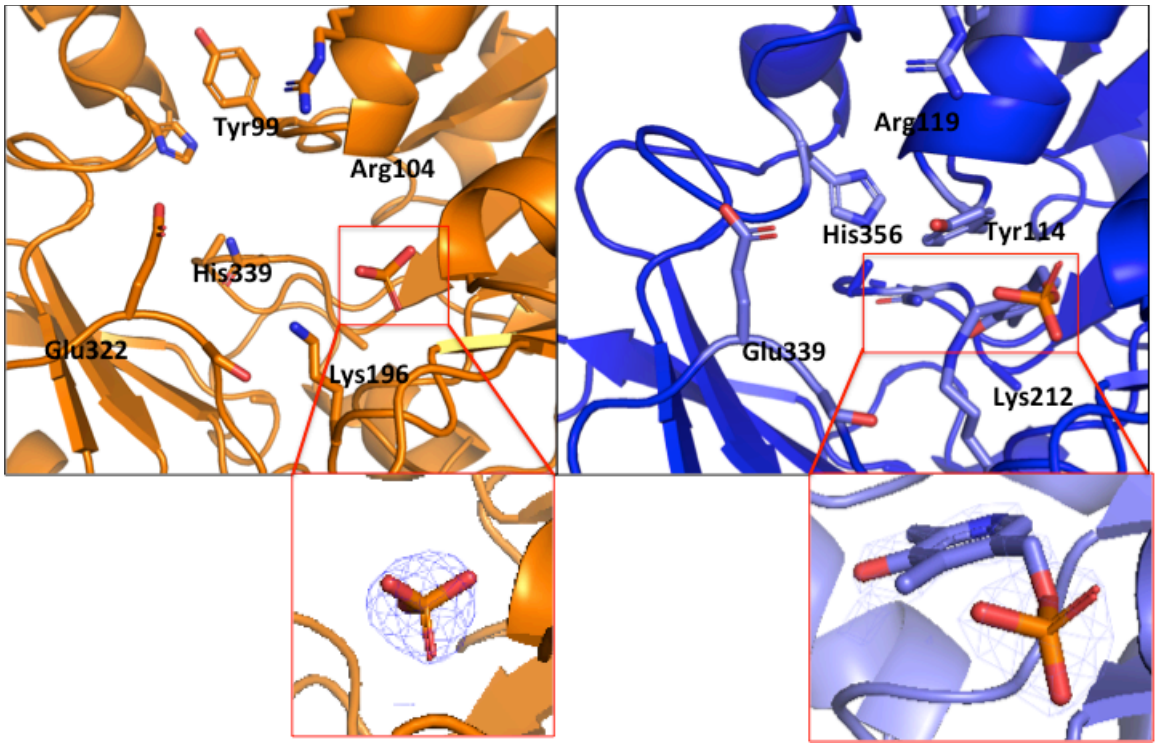

Figure 4.8 – Active site differences between saCSE (Orange) and huCSE (Blue, PDBiD 2NMP). Density of active site ligands highlighted. PLP is clearly bound to Lys212 in huCSE, whereas saCSE has a phosphate or sulfate group where the phosphate group of the tail of PLP residues. The active site Tyrosine is flipped up and away from the active site in saCSE.

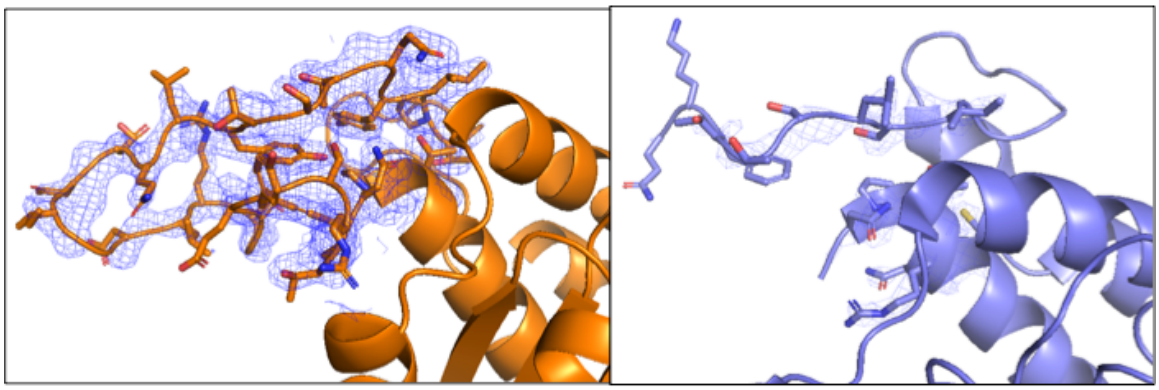

Figure 4.9 - Density difference for the N terminal loop region of saCSE (Orange) compared to the huCSE(Blue, PDB 2NMP). Electron Density mapped at 2Fobs – Fcalc, contoured to 1σ.

Table 4.1 – Crystallographic details for saCSE

	saCSE
Wavelength	
Resolution range	37.2 - 2.12 (2.196 - 2.12)
Space group	I 41 2 2
Unit cell	105.221 105.221 289.004 90 90 90
Total reflections	685109 (68391)
Unique reflections	46446 (4567)
Multiplicity	14.8 (15.0)
Completeness (%)	99.41 (99.08)
Mean I/sigma(I)	26.62 (1.09)
Wilson B-factor	42.89
R-merge	0.1705 (1.548)
R-meas	0.1765 (1.602)
R-pim	0.04499 (0.4091)
CC1/2	0.994 (0.91)
CC*	0.999 (0.976)
Reflections used in refinement	46199 (4527)
Reflections used for R-free	1979 (193)
R-work	0.2067 (0.3664)
R-free	0.2309 (0.3949)
CC(work)	0.960 (0.855)
CC(free)	0.960 (0.807)
Number of non-hydrogen atoms	3043
macromolecules	2922
ligands	5
solvent	116

Chapter 5

Structural Studies on *Bacillus subtilis* Arginase

Introduction

Arginase Pathway

Arginase is a binuclear manganese containing metalloenzyme that catalyzes the hydrolysis of L-arginine to urea and L-ornithine, which eventually leads to polyamine synthesis. This conversion is catalyzed by the attack of a metal coordinated hydroxyl ion used to cleave the guanidine group from L-arginine, thus generating urea and L-ornithine. Humans have two separate arginase isoforms: arginase I and arginase II[103]. Arginase I is a trimeric cytosolic enzyme found in the liver which acts in the final steps of the urea cycles. Arginase II is also a trimer, but is expressed as a mitochondrial protein in several tissues like the kidneys and brain[104, 105].

Arginase vs NOS.

Arginase competes with nitric oxide synthase (NOS) for the substrate arginine[106]. Which enzyme is being produced depends on the physical environment of the cell types where each is produced[104]. Naturally, dysregulation of arginase can have somewhat similar effects of NOS dysregulation, with disruptions effecting immune function, blood pressure regulation, and neuronal signaling[107, 108].

Bacterial Arginase

Bacteria have two methods by which they can generate ornithine from arginine: the arginase pathway and the arginine deiminase pathway. The arginase pathway leads towards the production of polyamines, whereas the arginine deiminase pathway moves towards cellular energy production and acid stress protection[109].

Pathogens use Arginase to deplete host Arginine levels.

Pathogenic intracellular bacteria rely on a variety of tools in order to survive and thrive in a hostile environment[110]. Several pathogens will utilize host arginine pools to both boost their own growth via arginase and deplete the host's ability to mount an immune response via

iNOS[11]. Arginase effectively competes with iNOS for the arginine pool due to Arginase's significantly higher Vmax[111]. Additionally, increased bacterial arginase expression induces a shift in the host macrophages to produce more of their own arginase[112, 113].

bNOS vs bArginase

Some gram-positive bacteria have their own version of NOS, which is used for a variety of functions[37, 114]. In the context of intracellular survival, it aids the bacteria in surviving the oxidative burst and protects them for the deleterious effects of antibiotics[39, 66]. It is currently unknown when or why bacteria utilize bNOS or barginase in order to aid in their survival. *Bacillus subtilis* has both a NOS and an arginase gene. The bsNOS has been well studied and characterized and is used as the model protein for developing bNOS selective inhbitors[41, 42, 59, 63]. The bsarginase has not been well characterized. Given that both enzymes share arginine as a substrate, we sought to investigate if there was the potential for our bNOS selective inhibitors to also inhibit bsArginase. To that end, we expressed, purified, crystallized, and solved the structure of *Bacillus subtilis* arginase to 2.07 Å resolution (PDB: 6DKT).

Materials and Methods

The known sequence of *Bacillus subtilis 168* arginase was cloned into a pET28a plasmid and overexpressed in E. coli BL21 DE3 cells with a fused N terminal His_6Tag. Cells were grown to an OD_{600} of 0.6 and expression was induced using 0.5 mM IPTG for 12 hours. Cells were pelleted by centrifugation at 4K rpm, 4C, 10 minutes. Cell pellets were resuspended in lysis buffer: 100 mM Hepes (pH 7.4), 10% Glycerol and 10 mM $MnCl_2$. Cells were lysed via shear stress. Lysate was separated from cellular debris via centrifugation at 15k RPM, 4C, 45 minutes. Arginase was purified using Ni-affinity and size exclusion chromatography. The purified concentrated protein was stored in 20 mM MOPS (pH 7.5) at -80C.

Small rod shaded arginase crystals were discovered from crystal screens. Optimization of conditions led to large rod shaped crystals of arginase at 14 mg/ml in 90 mM BisTris (pH 7.7) 10 mM Bis Tris (pH 9.0), 10 mM $MnCl_2$ 11% PEG8000 and 6% PGA. (Figure 5.1) Crystals were harvested and cryoprotected in well solution with 70% glycerol v/v. Crystals were flash frozen in liquid nitrogen.

X-ray diffraction data were collected on individual crystals at SSRL beam line 14-1. The Data frames were indexed and integrated using MOSFLM[46]. Index data sets were scaled using Aimless[48]. The structure was solved using molecular replacement using chain A of 2CEV by PHASER in RefMac. The initial MR model was modified by PHENIX plugin Sculptor to mutate the previously known structure to match the primary sequence of bsarginase[51]. Structure factors were refined using PHENIX. COOT was used to build the model and PyMOL was used to create the figures[52]. Data collection and refinement statistics are listed in Table 5.1. Homology structure was generated from our PDB using the CONSURF server[115-118].

Results and Discussion

bsarginase assembles into a hexamer within the unit cell of the crystal structure(Figure 5.2 A). Each monomer consists of a central 8 strand β-sheet packed on either side by either 3 or 4 α-helices(Figure 5.2 B). The active site contains two Mn^{2+} ions near the C-terimunus of the central β-strands. The symmetry and structure of the *bacillus subtilis* arginase is quite similar to previously solved structure of the related *Bacillus caldovelox* arginase.

Looking at the active site more closely, we see the two Mn^{2+} ions in the same positions as found in other arginases(Figure 5.2C). The manganese ion furthest from the solvent is in a square pyramidal geometry and is coordinated by His97, Asp 120, Asp 124, Asp223, and a linking water molecule(Figure 5.3). The manganese ion closest to the surface is a somewhat distorted

octahedral geometry and is coordinated by Asp120, His122, Asp223, Asp225 and that same bridging water.

bsarginase shares 42% identity with human arginase I, and the active site is conserved(Figure 5.4). Indeed, a CONSURF generated BLAST of 150 related homologues to bsarginase show a high degree of conservation around the active site (Figure 5.4). This is probably due to the highly conserved nature of arginase, which is found in all kingdoms of life. It seems unlikely that isoform selective inhibitors could be generated for a bacterial arginase, given that the active sites are so well conserved.

It also seems unlikely that our bNOS selective inhibitors would bind well to bsarginase for several reasons. Primarily, the active site pocket is rather shallow and much more solvent accessible than the deep pocket of bsNOS. In addition, the amino acids around the active site that hold the substrate in place are quite different [106]. Further experiments to test the binding affinity and efficacy of the bNOS inhibitors for bsarginase would elucidate this.

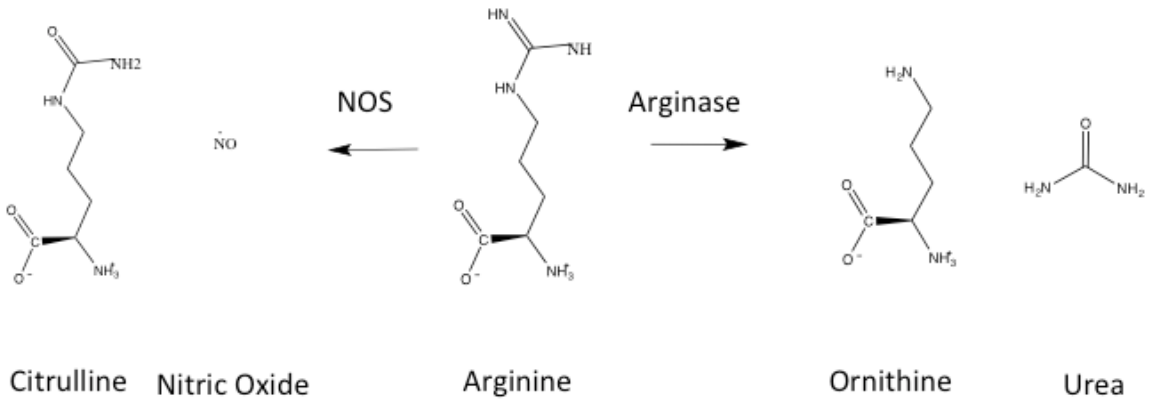

Scheme 5.1 – Arginine Pathways – either processed by arginase to generate ornithine and urea and push towards the polyamine pathway, or to generate NO and citrulline via NOS.

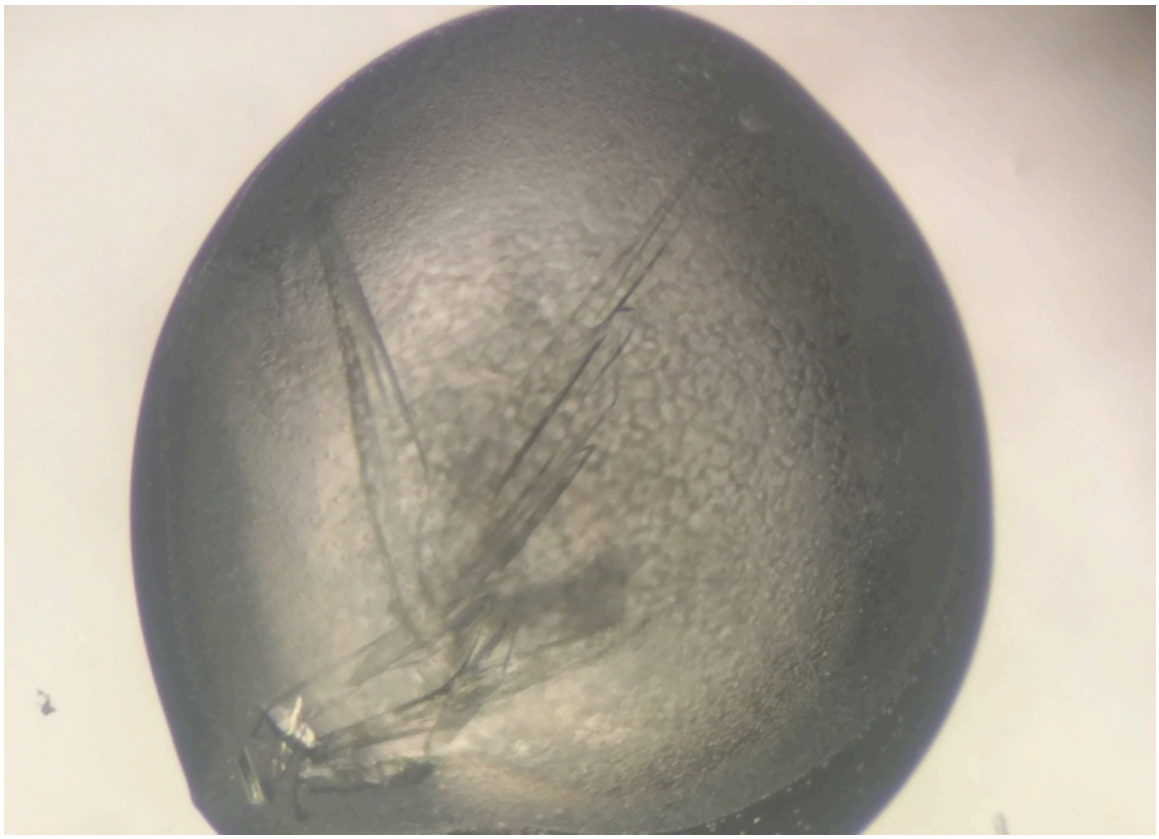

Figure 5.1 - Arginase crystals grew as long rods in 90 mM BisTris (pH 7.7) 10 mM Bis Tris (pH 9.0), 10 mM $MnCl_2$ 11% PEG8000 and 6% PGA at 14 mg/ml.

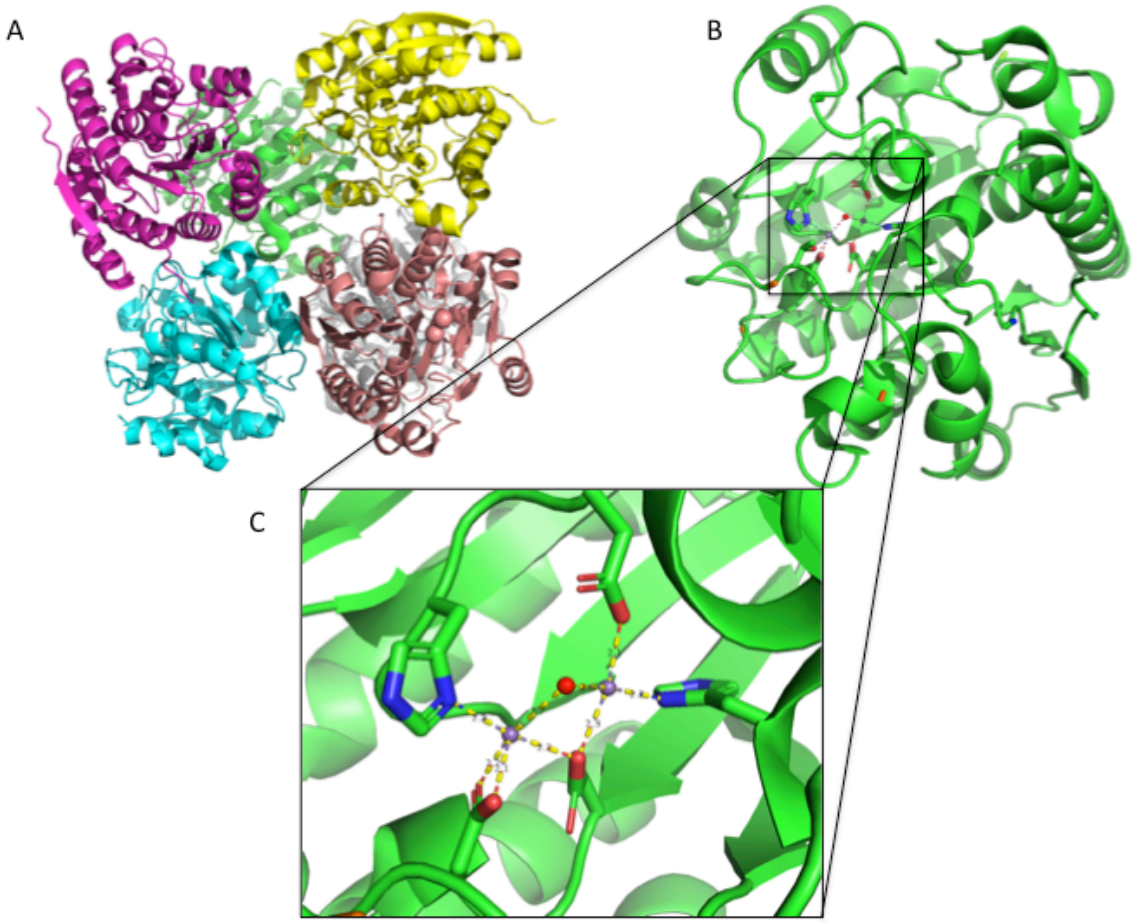

Figure 5.2 - A) Arginase forms a hexamer in the unit cell. B) Monomer of arginase with 8 central β-sheets with 3 and 4 α-helices on each side.

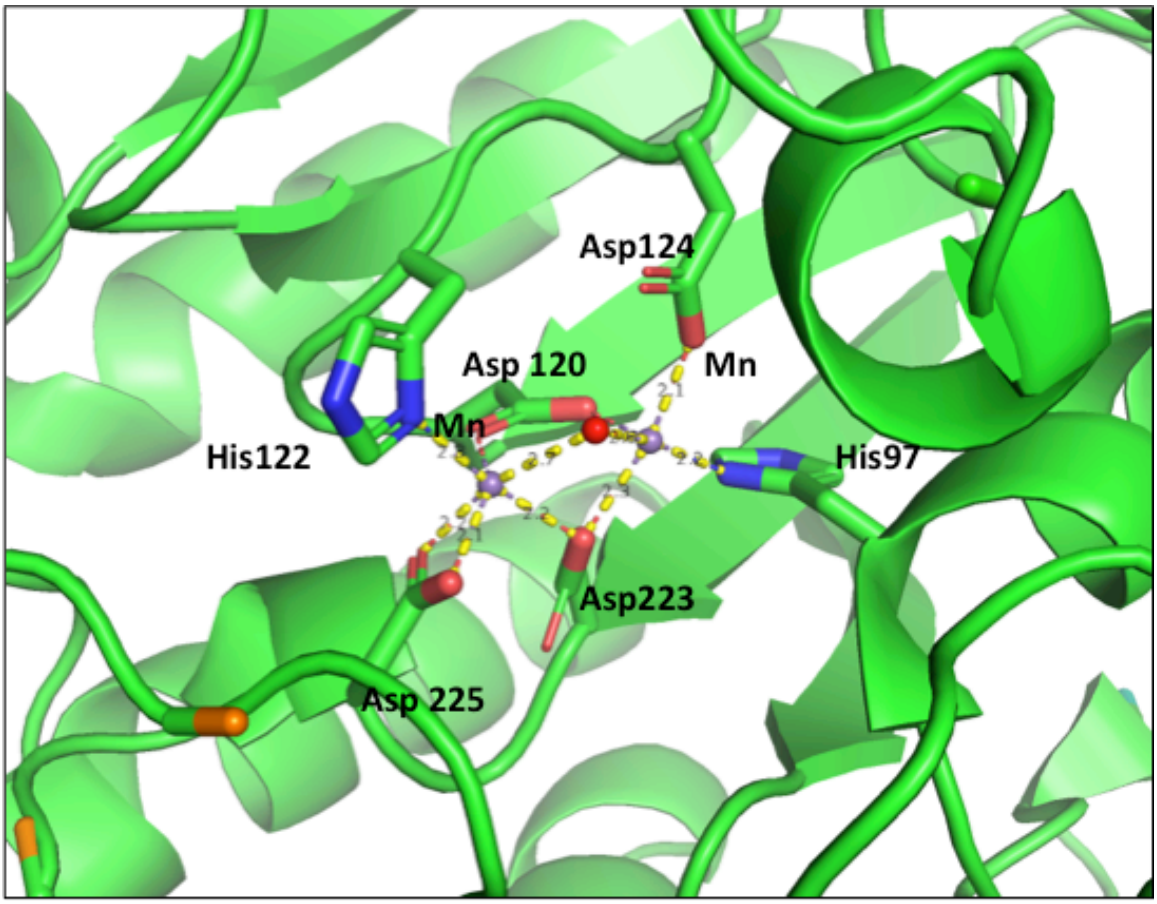

Figure 5.3 – Active site of bsarginase. A water molecule links the two manganese ions which are coordinated by His and Asp residues.

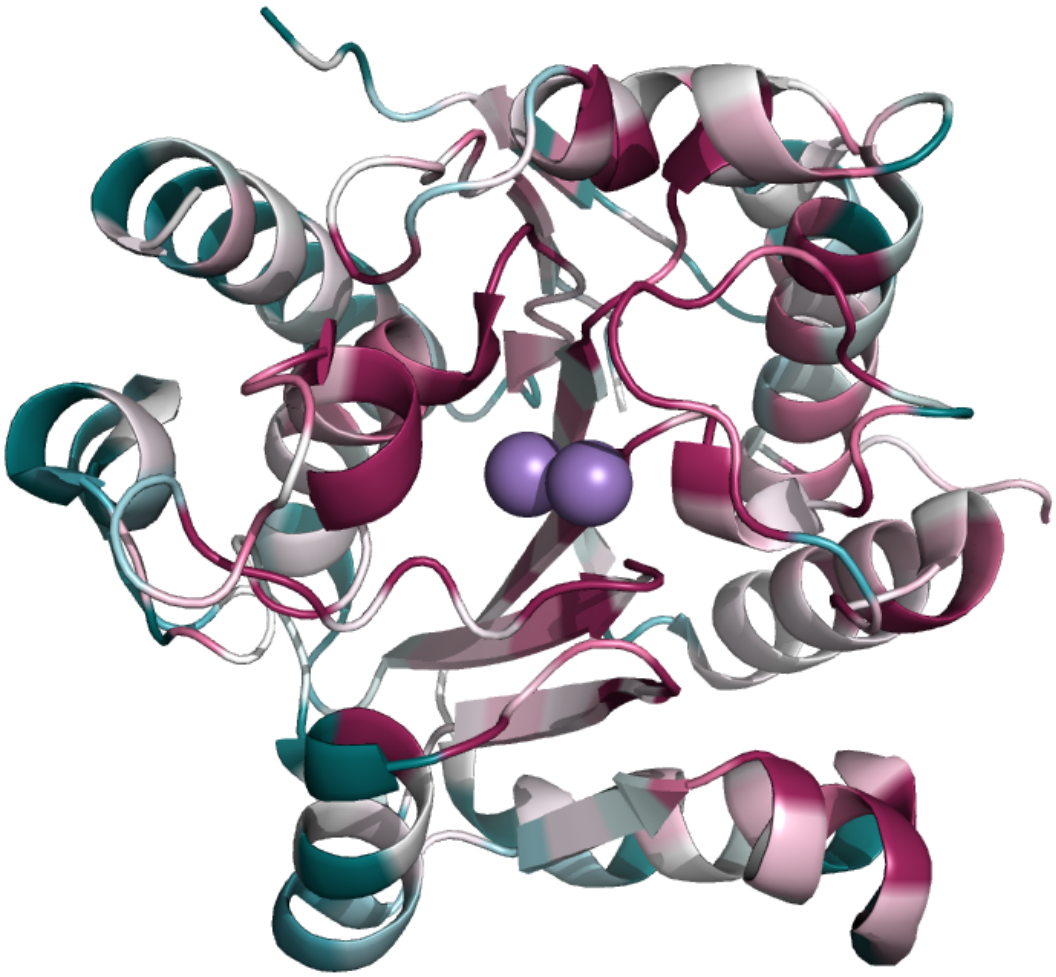

Figure 5.4 - Conservation of Arginase across species. Red are more conservfed, blue are less conserved amino acids. The active site around the two manganese ions is highly conserved. Conservation calculated using CONSURF server.

Table 5.1 – Crystallographic details for each arginase structure

	Arginase
Wavelength	0.979493 Å
Resolution range	46.08 – 20.77 (2.151 – 2.077)
Space group	P 1 21 1
Unit cell	77.1399 128.55 82.02 90 112.69 90
Total reflections	168905 (16255)
Unique reflections	88598 (8819)
Multiplicity	1.9 (1.8)
Completeness (%)	100 (100)
Mean I / sigma(I)	6.26 (1.92)
Wilson B-factor	28.04
R-merge	0.05977 (0.2799)
R-meas	0.08453 (0.3958)
$CC_{1/2}$	0.993 (0.803)
CC*	0.998 (0.944)
Reflections used in refinement	88581 (8815)
Reflections used for R-free	2009 (209)
R-work	0.2044 (0.2609)
R-free	0.2314 (0.3155)
Number of non-hydrogen atoms	13125
Macromolecules	12578
Ligands	12
Protein residues	1692
RMS (bonds)	0.004
RMS (angles)	0.74
Ramachandran plot	
Favored (%)	95
Allowed (%)	3.6
Outliers (%)	1.8
Rotamer outliers (%)	7.8
Clashscore	7.45
Average B-factor	40.52
Macromolecules	40.61
Ligands	25.89
Solvent	38.71
Number of TLS groups	6

Statistics for the highest-resolution shell are shown in parentheses

Conclusions and Final Thoughts

Bacterial nitric oxide synthase has been our target for developing a novel therapeutic due to its important function in protecting pathogenic bacteria like methicillin resistant *Staphylococcus aureus* and *Bacillus anthracis* from both antibiotics and the host immune system[39, 66]. The greatest challenge thus far has been to develop an inhibitor selective for bNOS over the 3 mammalian isoforms, which all share high structural homology[59]. Overcoming that selectivity issue to avoid negative side effects of NOS inhibition has been and will continue to be of prime importance in developing a bNOS selective inhibitor. The biggest structural difference between bNOS and mNOS is pterin binding pocket, which due to an N-terminal zinc binding domain of mNOS causes a significantly greater affinity for pterin for mNOS than bNOS[41].

Building on the work of Dr. Jeffrey Holden and our collaborators in the Silverman group at Northwestern University, we continued to screen for bNOS selective inhibitors[44, 59]. In order to identify if there was rotameric freedom of Tyr357 in bNOS, which would open up additional surface area for ligand binding, we made a Tyr -> Phe mutation[42]. Crystal structures of our inhibitors and the Y357F mutant revealed that there is indeed rotameric freedom of that residue, which could provide potential for a bulky inhibitor to occupy that area in bNOS[42].

The next portion involved the continuing optimization of aminoquinolone based inhibitors, which had been found to show both higher selectivity towards bNOS and were based around the anti-microbial chemical moiety of aminoquinolone (Chapter 1). Interestingly, this class of inhibitor was found to occupy the pterin site as well as the active site with two separate molecules. Another class of molecules involving an dual headed aminopyridine group was able to occupy both the active site and the pterin site in the absence of BH_4. This was the first indication that it would be possible to target both the active site and the pterin site of bNOS simultaneously. By developing an inhibitor with both an aminoquinolone and an aminopyridine

group, we sought to occupy both the active site and the pterin site simultaneously, even in the presence of BH_4. (Chapter 2)

Our next goal was to test the efficacy and selectivity of our inhibitors in living systems (Chapters 2 and 3). We found that our selective inhibitors were able to effectively decrease the intracellular survival of MRSA in mouse macrophages (Chapter 2). In an effort to develop a high throughput screening tool for measuring the ability of our bNOS selective inhibitors to both enter the cell and inhibit NO production, we found that an NO selective probe actually also measured another small gasotransmitter H_2S (Chapter 3).

It had been noted that bacteria will compensate the inhibition of NO or H_2S via increasing the production of the other[71]. H_2S is also associated with pathogenic bacterial intracellular survival and resistance to some classes of antibiotics[73]. In order to better understand H_2S production in MRSA, we expressed, purified and characterized saCBS and saCSE (Chapter 4). The crystal structure of saCSE has the potential to open up a new avenue for drug development. Further investigation and study of these systems may shed new light on the dynamic nature of the interplay between NO and H_2S.

Chapter 5 involved the solving of the structure of arginase from *Bacillus subtilis.* It was a small step in the broader study of the interplay between arginase and NOS as competitors for arginine. While we did not note any major structural differences, we did find more evidence of the conservation found within arginases.

In conclusion, we have pushed forward the development of bNOS selective inhibitors and found a subset which are able to occupy both the active site and the pterin cofactor site. We found them to be effective in reducing MRSA's intracellular survival in macrophages, as well as reducing MRSA's survival with H_2O_2. We opened up a new avenue for exploring a combined treatment by trying to inhibit both bNOS and saCSE/CBS simultaneously if suitable drugs could be discovered or developed. Future experiments to test the ability of our bNOS selective

inhibitors in a mouse model of infection would pave the way towards having another tool against MRSA.

1. Brauner, A., et al., *Distinguishing between resistance, tolerance and persistence to antibiotic treatment.* Nat Rev Microbiol, 2016. **14**(5): p. 320-30.
2. Kester, J.C. and S.M. Fortune, *Persisters and beyond: mechanisms of phenotypic drug resistance and drug tolerance in bacteria.* Crit Rev Biochem Mol Biol, 2014. **49**(2): p. 91-101.
3. Handwerger, S. and A. Tomasz, *Antibiotic tolerance among clinical isolates of bacteria.* Rev Infect Dis, 1985. **7**(3): p. 368-86.
4. Fridman, O., et al., *Optimization of lag time underlies antibiotic tolerance in evolved bacterial populations.* Nature, 2014. **513**(7518): p. 418-21.
5. Tuomanen, E., et al., *The rate of killing of Escherichia coli by beta-lactam antibiotics is strictly proportional to the rate of bacterial growth.* J Gen Microbiol, 1986. **132**(5): p. 1297-304.
6. Tuchscherr, L., et al., *Staphylococcus aureus phenotype switching: an effective bacterial strategy to escape host immune response and establish a chronic infection.* EMBO Mol Med, 2011. **3**(3): p. 129-41.
7. Leimer, N., et al., *Nonstable Staphylococcus aureus Small-Colony Variants Are Induced by Low pH and Sensitized to Antimicrobial Therapy by Phagolysosomal Alkalinization.* J Infect Dis, 2016. **213**(2): p. 305-13.
8. Sandoz, K.M., et al., *Transcriptional Profiling of Coxiella burnetii Reveals Extensive Cell Wall Remodeling in the Small Cell Variant Developmental Form.* PLoS One, 2016. **11**(2): p. e0149957.
9. Dastgheyb, S.S. and M. Otto, *Staphylococcal adaptation to diverse physiologic niches: an overview of transcriptomic and phenotypic changes in different biological environments.* Future Microbiol, 2015. **10**(12): p. 1981-95.
10. von Eiff, C., et al., *Intracellular persistence of Staphylococcus aureus small-colony variants within keratinocytes: a cause for antibiotic treatment failure in a patient with darier's disease.* Clin Infect Dis, 2001. **32**(11): p. 1643-7.
11. Gobert, A.P., et al., *Helicobacter pylori arginase inhibits nitric oxide production by eukaryotic cells: a strategy for bacterial survival.* Proc Natl Acad Sci U S A, 2001. **98**(24): p. 13844-9.
12. Lacoma, A., et al., *Investigating intracellular persistence of Staphylococcus aureus within a murine alveolar macrophage cell line.* Virulence, 2017. **8**(8): p. 1761-1775.
13. Zhou, L. and D.Y. Zhu, *Neuronal nitric oxide synthase: structure, subcellular localization, regulation, and clinical implications.* Nitric Oxide, 2009. **20**(4): p. 223-30.
14. Wang, Z.Q., et al., *A conserved Val to Ile switch near the heme pocket of animal and bacterial nitric-oxide synthases helps determine their distinct catalytic profiles.* J Biol Chem, 2004. **279**(18): p. 19018-25.
15. Pant, K., et al., *Structure of a nitric oxide synthase heme protein from Bacillus subtilis.* Biochemistry, 2002. **41**(37): p. 11071-9.
16. Beaumont, E., et al., *Distal Val346Ile mutation in inducible NO synthase promotes substrate-dependent NO confinement.* Biochemistry, 2007. **46**(47): p. 13533-40.
17. Whited, C.A., et al., *Gating NO release from nitric oxide synthase.* J Am Chem Soc, 2012. **134**(1): p. 27-30.
18. Abu-Soud, H.M., et al., *Electron transfer, oxygen binding, and nitric oxide feedback inhibition in endothelial nitric-oxide synthase.* J Biol Chem, 2000. **275**(23): p. 17349-57.
19. Santolini, J., A.L. Meade, and D.J. Stuehr, *Differences in three kinetic parameters underpin the unique catalytic profiles of nitric-oxide synthases I, II, and III.* J Biol Chem, 2001. **276**(52): p. 48887-98.
20. Tsutsui, Y., et al., *Reaction Intermediates of Nitric Oxide Synthase from Deinococcus radiodurans as Revealed by Pulse Radiolysis: Evidence for Intramolecular Electron Transfer from Biopterin to Fe(II)-O2 Complex.* Biochemistry, 2018. **57**(10): p. 1611-1619.
21. CDC. Available from: https://http://www.cdc.gov/mrsa/.

22. Williams, D.E. and E.M. Boon, *Towards Understanding the Molecular Basis of Nitric Oxide-Regulated Group Behaviors in Pathogenic Bacteria.* J Innate Immun, 2019. **11**(3): p. 205-215.
23. Hossain, S., L.M. Nisbett, and E.M. Boon, *Discovery of Two Bacterial Nitric Oxide-Responsive Proteins and Their Roles in Bacterial Biofilm Regulation.* Acc Chem Res, 2017. **50**(7): p. 1633-1639.
24. Arora, D.P., et al., *Nitric Oxide Regulation of Bacterial Biofilms.* Biochemistry, 2015. **54**(24): p. 3717-28.
25. Hall-Stoodley, L., J.W. Costerton, and P. Stoodley, *Bacterial biofilms: from the natural environment to infectious diseases.* Nat Rev Microbiol, 2004. **2**(2): p. 95-108.
26. Nisbett, L.M. and E.M. Boon, *Nitric Oxide Regulation of H-NOX Signaling Pathways in Bacteria.* Biochemistry, 2016. **55**(35): p. 4873-84.
27. Rinaldo, S., et al., *Beyond nitrogen metabolism: nitric oxide, cyclic-di-GMP and bacterial biofilms.* FEMS Microbiol Lett, 2018. **365**(6).
28. Plate, L. and M.A. Marletta, *Nitric oxide modulates bacterial biofilm formation through a multicomponent cyclic-di-GMP signaling network.* Mol Cell, 2012. **46**(4): p. 449-60.
29. Cao, S., et al., *Alternative Evolutionary Pathways for Drug-Resistant Small Colony Variant Mutants in Staphylococcus aureus.* mBio, 2017. **8**(3).
30. Hall, J.W., et al., *The Staphylococcus aureus AirSR Two-Component System Mediates Reactive Oxygen Species Resistance via Transcriptional Regulation of Staphyloxanthin Production.* Infect Immun, 2017. **85**(2).
31. Holden, J.K., et al., *Nitric Oxide Synthase as a Target for Methicillin-Resistant Staphylococcus aureus.* Chem Biol, 2015. **22**(6): p. 785-92.
32. Crane, B.R., J. Sudhamsu, and B.A. Patel, *Bacterial nitric oxide synthases.* Annu Rev Biochem, 2010. **79**: p. 445-70.
33. Holden, J.K., et al., *Structure-based design of bacterial nitric oxide synthase inhibitors.* J Med Chem, 2015. **58**(2): p. 994-1004.
34. Wang, Z.Q., et al., *Bacterial flavodoxins support nitric oxide production by Bacillus subtilis nitric-oxide synthase.* J. Biol. Chem., 2007. **282**(4): p. 2196-202.
35. Pant, K. and B.R. Crane, *Structure of a loose dimer: an intermediate in nitric oxide synthase assembly.* J. Mol. Biol., 2005. **352**(4): p. 932-40.
36. Adak, S., K.S. Aulak, and D.J. Stuehr, *Direct evidence for nitric oxide production by a nitric-oxide synthase-like protein from Bacillus subtilis.* J Biol Chem, 2002. **277**(18): p. 16167-71.
37. Sudhamsu, J. and B.R. Crane, *Bacterial nitric oxide synthases: what are they good for?* Trends Microbiol, 2009. **17**(5): p. 212-8.
38. Gusarov, I. and E. Nudler, *NO-mediated cytoprotection: instant adaptation to oxidative stress in bacteria.* Proc. Natl. Acad. Sci. U.S.A., 2005. **102**(39): p. 13855-60.
39. Gusarov, I., et al., *Endogenous nitric oxide protects bacteria against a wide spectrum of antibiotics.* Science, 2009. **325**(5946): p. 1380-4.
40. van Sorge, N.M., et al., *Methicillin-resistant Staphylococcus aureus bacterial nitric-oxide synthase affects antibiotic sensitivity and skin abscess development.* J Biol Chem, 2013. **288**(9): p. 6417-26.
41. Holden, J.K., et al., *Structural and biological studies on bacterial nitric oxide synthase inhibitors.* Proc Natl Acad Sci U S A, 2013. **110**(45): p. 18127-31.
42. Holden, J.K., et al., *Inhibitor Bound Crystal Structures of Bacterial Nitric Oxide Synthase.* Biochemistry, 2015. **54**(26): p. 4075-82.
43. Goldschmidt, L., et al., *Toward rational protein crystallization: A Web server for the design of crystallizable protein variants.* Protein Sci., 2007. **16**(8): p. 1569-76.
44. Holden, J.K., N. Lim, and T.L. Poulos, *Identification of redox partners and development of a novel chimeric bacterial nitric oxide synthase for structure activity analyses.* J Biol Chem, 2014. **289**(42): p. 29437-45.
45. Roman, L.J., et al., *High-level expression of functional rat neuronal nitric oxide synthase in Escherichia coli.* Proc. Natl. Acad. Sci. U.S.A., 1995. **92**(18): p. 8428-32.
46. Battye, T.G., et al., *iMOSFLM: a new graphical interface for diffraction-image processing with MOSFLM.* Acta Crystallogr D Biol Crystallogr, 2011. **67**(Pt 4): p. 271-81.
47. Kabsch, W., *Xds.* Acta Crystallogr D Biol Crystallogr, 2010. **66**(Pt 2): p. 125-32.

48. Evans, P., *Scaling and assessment of data quality.* Acta Crystallogr D Biol Crystallogr, 2006. **62**(Pt 1): p. 72-82.
49. Strong, M., et al., *Toward the structural genomics of complexes: crystal structure of a PE/PPE protein complex from Mycobacterium tuberculosis.* Proc. Natl. Acad. Sci. U.S.A., 2006. **103**(21): p. 8060-5.
50. Murshudov, G.N., A.A. Vagin, and E.J. Dodson, *Refinement of macromolecular structures by the maximum-likelihood method.* Acta. Crystallogr. D, 1997. **53**: p. 240-255.
51. Adams, P.D., et al., *PHENIX: a comprehensive Python-based system for macromolecular structure solution.* Acta Crystallogr D Biol Crystallogr, 2010. **66**(Pt 2): p. 213-21.
52. Emsley, P., et al., *Features and development of Coot.* Acta Crystallogr D Biol Crystallogr, 2010. **66**(Pt 4): p. 486-501.
53. Cinelli, M.A., et al., *Simplified 2-aminoquinoline-based scaffold for potent and selective neuronal nitric oxide synthase inhibition.* J. Med. Chem., 2014. **57**(4): p. 1513-30.
54. Rudner, B., *Process for aminating nitrogen-containing heterocyclic compounds.* US Patent 2892841 A, 1959.
55. Kaye, I.A., *2-Lepidyl Substituted Diamines.* J. Am. Chem. Soc., 1949. **71**(7): p. 2322-2325.
56. Stuehr, D.J., *Enzymes of the L-Arginine to Nitric Oxide Pathway.* The Journal of Nutrition, 2004. **134**(10): p. 2748S-2751S.
57. Kinkel, T.L., et al., *An essential role for bacterial nitric oxide synthase in Staphylococcus aureus electron transfer and colonization.* Nat Microbiol, 2016. **2**: p. 16224.
58. Kinkel, T.L., et al., *The Staphylococcus aureus SrrAB Two-Component System Promotes Resistance to Nitrosative Stress and Hypoxia.* mBio, 2013. **4**(6).
59. Poulos, T.L. and H. Li, *Structural basis for isoform-selective inhibition in nitric oxide synthase.* Acc Chem Res, 2013. **46**(2): p. 390-8.
60. Silverman, R.B., *Design of selective neuronal nitric oxide synthase inhibitors for the prevention and treatment of neurodegenerative diseases.* Acc. Chem. Res., 2009. **42**(3): p. 439-51.
61. Hevel, J.M. and M.A. Marletta, *Macrophage nitric oxide synthase: relationship between enzyme-bound tetrahydrobiopterin and synthase activity.* Biochemistry, 1992. **31**(31): p. 7160-7165.
62. Mayer, B., et al., *Brain nitric oxide synthase is a biopterin- and flavin-containing multi-functional oxido-reductase.* FEBS Letters, 1991. **288**(1-2): p. 187-191.
63. Holden, J.K., et al., *Targeting Bacterial Nitric Oxide Synthase with Aminoquinoline-Based Inhibitors.* Biochemistry, 2016. **55**(39): p. 5587-5594.
64. Takeshita, S., K. Kaji, and A. Kudo, *Identification and characterization of the new osteoclast progenitor with macrophage phenotypes being able to differentiate into mature osteoclasts.* J Bone Miner Res, 2000. **15**(8): p. 1477-88.
65. Griffith, O.W. and D.J. Stuehr, *Nitric oxide synthases: properties and catalytic mechanism.* Annu Rev Physiol, 1995. **57**: p. 707-36.
66. Shatalin, K., et al., *Bacillus anthracis-derived nitric oxide is essential for pathogen virulence and survival in macrophages.* Proc Natl Acad Sci U S A, 2008. **105**(3): p. 1009-13.
67. Hausladen, A., et al., *Assessment of nitric oxide signals by triiodide chemiluminescence.* Proc Natl Acad Sci U S A, 2007. **104**(7): p. 2157-62.
68. Lim, M.H., *Preparation of a copper-based fluorescent probe for nitric oxide and its use in mammalian cultured cells.* Nat Protoc, 2007. **2**(2): p. 408-15.
69. Lim, M.H., D. Xu, and S.J. Lippard, *Visualization of nitric oxide in living cells by a copper-based fluorescent probe.* Nat Chem Biol, 2006. **2**(7): p. 375-80.
70. McQuade, L.E. and S.J. Lippard, *Fluorescence-based nitric oxide sensing by Cu(II) complexes that can be trapped in living cells.* Inorg Chem, 2010. **49**(16): p. 7464-71.
71. Luhachack, L. and E. Nudler, *Bacterial gasotransmitters: an innate defense against antibiotics.* Curr Opin Microbiol, 2014. **21**: p. 13-7.
72. Collins, T.J., *ImageJ for microscopy.* Biotechniques, 2007. **43**(1 Suppl): p. 25-30.
73. Shatalin, K., et al., *H2S: a universal defense against antibiotics in bacteria.* Science, 2011. **334**(6058): p. 986-90.
74. Kabil, O. and R. Banerjee, *Redox biochemistry of hydrogen sulfide.* J Biol Chem, 2010. **285**(29): p. 21903-7.
75. Singh, S. and R. Banerjee, *PLP-dependent H(2)S biogenesis.* Biochim Biophys Acta, 2011. **1814**(11): p. 1518-27.

76. Alexander, F.W., et al., *Evolutionary relationships among pyridoxal-5'-phosphate-dependent enzymes. Regio-specific alpha, beta and gamma families.* Eur J Biochem, 1994. **219**(3): p. 953-60.
77. Benavides, G.A., et al., *Hydrogen sulfide mediates the vasoactivity of garlic.* Proc Natl Acad Sci U S A, 2007. **104**(46): p. 17977-82.
78. Mosharov, E., M.R. Cranford, and R. Banerjee, *The quantitatively important relationship between homocysteine metabolism and glutathione synthesis by the transsulfuration pathway and its regulation by redox changes.* Biochemistry, 2000. **39**(42): p. 13005-11.
79. Lo, R., et al., *Cystathionine gamma-lyase is a component of cystine-mediated oxidative defense in Lactobacillus reuteri BR11.* J Bacteriol, 2009. **191**(6): p. 1827-37.
80. Wang, J. and R.A. Hegele, *Genomic basis of cystathioninuria (MIM 219500) revealed by multiple mutations in cystathionine gamma-lyase (CTH).* Hum Genet, 2003. **112**(4): p. 404-8.
81. Abe, K. and H. Kimura, *The possible role of hydrogen sulfide as an endogenous neuromodulator.* J Neurosci, 1996. **16**(3): p. 1066-71.
82. Zhao, W., et al., *The vasorelaxant effect of H(2)S as a novel endogenous gaseous K(ATP) channel opener.* EMBO J, 2001. **20**(21): p. 6008-16.
83. Yang, G., et al., *H2S as a physiologic vasorelaxant: hypertension in mice with deletion of cystathionine gamma-lyase.* Science, 2008. **322**(5901): p. 587-90.
84. Koenitzer, J.R., et al., *Hydrogen sulfide mediates vasoactivity in an O2-dependent manner.* Am J Physiol Heart Circ Physiol, 2007. **292**(4): p. H1953-60.
85. Blackstone, E., M. Morrison, and M.B. Roth, *H2S induces a suspended animation-like state in mice.* Science, 2005. **308**(5721): p. 518.
86. Mustafa, A.K., et al., *H2S signals through protein S-sulfhydration.* Sci Signal, 2009. **2**(96): p. ra72.
87. Ida, T., et al., *Reactive cysteine persulfides and S-polythiolation regulate oxidative stress and redox signaling.* Proc Natl Acad Sci U S A, 2014. **111**(21): p. 7606-11.
88. Cooper, C.E. and G.C. Brown, *The inhibition of mitochondrial cytochrome oxidase by the gases carbon monoxide, nitric oxide, hydrogen cyanide and hydrogen sulfide: chemical mechanism and physiological significance.* J Bioenerg Biomembr, 2008. **40**(5): p. 533-9.
89. Cuevasanta, E., et al., *Reaction of Hydrogen Sulfide with Disulfide and Sulfenic Acid to Form the Strongly Nucleophilic Persulfide.* J Biol Chem, 2015. **290**(45): p. 26866-80.
90. Vazquez-Torres, A., *Redox active thiol sensors of oxidative and nitrosative stress.* Antioxid Redox Signal, 2012. **17**(9): p. 1201-14.
91. Pan, J. and K.S. Carroll, *Chemical biology approaches to study protein cysteine sulfenylation.* Biopolymers, 2014. **101**(2): p. 165-72.
92. Ono, K., et al., *Redox chemistry and chemical biology of H2S, hydropersulfides, and derived species: implications of their possible biological activity and utility.* Free Radic Biol Med, 2014. **77**: p. 82-94.
93. Chang, W., et al., *Global transcriptome analysis of Staphylococcus aureus response to hydrogen peroxide.* J Bacteriol, 2006. **188**(4): p. 1648-59.
94. Messerschmidt, A., et al., *Determinants of enzymatic specificity in the Cys-Met-metabolism PLP-dependent enzymes family: crystal structure of cystathionine gamma-lyase from yeast and intrafamiliar structure comparison.* Biol Chem, 2003. **384**(3): p. 373-86.
95. Sun, Q., et al., *Structural basis for the inhibition mechanism of human cystathionine gamma-lyase, an enzyme responsible for the production of H(2)S.* J Biol Chem, 2009. **284**(5): p. 3076-85.
96. Ejim, L.J., et al., *Inhibitors of bacterial cystathionine beta-lyase: leads for new antimicrobial agents and probes of enzyme structure and function.* J Med Chem, 2007. **50**(4): p. 755-64.
97. Kuehnert, M.J., et al., *Prevalence of Staphylococcus aureus nasal colonization in the United States, 2001-2002.* J Infect Dis, 2006. **193**(2): p. 172-9.
98. Wu, G., et al., *A Matter of Timing: Contrasting Effects of Hydrogen Sulfide on Oxidative Stress Response in Shewanella oneidensis.* J Bacteriol, 2015. **197**(22): p. 3563-72.
99. Giordana, L., et al., *Cystathionine gamma-lyase, an enzyme related to the reverse transsulfuration pathway, is functional in Leishmania spp.* J Eukaryot Microbiol, 2014. **61**(2): p. 204-13.
100. Romero, I., et al., *Upregulation of Cysteine Synthase and Cystathionine beta-Synthase Contributes to Leishmania braziliensis Survival under Oxidative Stress.* Antimicrob Agents Chemother, 2015. **59**(8): p. 4770-81.

101. Wheeler, P.R., et al., *Functional demonstration of reverse transsulfuration in the Mycobacterium tuberculosis complex reveals that methionine is the preferred sulfur source for pathogenic Mycobacteria.* J Biol Chem, 2005. **280**(9): p. 8069-78.
102. Beavers, W.N. and E.P. Skaar, *Neutrophil-generated oxidative stress and protein damage in Staphylococcus aureus.* Pathog Dis, 2016. **74**(6).
103. Jenkinson, C.P., W.W. Grody, and S.D. Cederbaum, *Comparative properties of arginases.* Comp Biochem Physiol B Biochem Mol Biol, 1996. **114**(1): p. 107-32.
104. Nakamura, H., T. Saheki, and S. Nakagawa, *Differential cellular localization of enzymes of L-arginine metabolism in the rat brain.* Brain Res, 1990. **530**(1): p. 108-12.
105. Xu, L., et al., *Arginase and autoimmune inflammation in the central nervous system.* Immunology, 2003. **110**(1): p. 141-8.
106. Cox, J.D., et al., *Mechanistic and metabolic inferences from the binding of substrate analogues and products to arginase.* Biochemistry, 2001. **40**(9): p. 2689-701.
107. Cox, J.D., et al., *Arginase-boronic acid complex highlights a physiological role in erectile function.* Nat Struct Biol, 1999. **6**(11): p. 1043-7.
108. Christianson, D.W., *Arginase: structure, mechanism, and physiological role in male and female sexual arousal.* Acc Chem Res, 2005. **38**(3): p. 191-201.
109. Cusumano, Z.T., M.E. Watson, Jr., and M.G. Caparon, *Streptococcus pyogenes arginine and citrulline catabolism promotes infection and modulates innate immunity.* Infect Immun, 2014. **82**(1): p. 233-42.
110. Nathan, C. and M.U. Shiloh, *Reactive oxygen and nitrogen intermediates in the relationship between mammalian hosts and microbial pathogens.* Proc Natl Acad Sci U S A, 2000. **97**(16): p. 8841-8.
111. Yu, J.J., et al., *Expression, purification, and biochemical properties of arginase from Bacillus subtilis 168.* J Microbiol, 2013. **51**(2): p. 222-8.
112. Das, P., et al., *Modulation of the arginase pathway in the context of microbial pathogenesis: a metabolic enzyme moonlighting as an immune modulator.* PLoS Pathog, 2010. **6**(6): p. e1000899.
113. Gobert, A.P., et al., *Helicobacter pylori induces macrophage apoptosis by activation of arginase II.* J Immunol, 2002. **168**(9): p. 4692-700.
114. Lewis, A.M., et al., *Examination of the Staphylococcus aureus nitric oxide reductase (saNOR) reveals its contribution to modulating intracellular NO levels and cellular respiration.* Mol Microbiol, 2015. **96**(3): p. 651-69.
115. Glaser, F., et al., *The ConSurf-HSSP database: the mapping of evolutionary conservation among homologs onto PDB structures.* Proteins, 2005. **58**(3): p. 610-7.
116. Ashkenazy, H., et al., *ConSurf 2010: calculating evolutionary conservation in sequence and structure of proteins and nucleic acids.* Nucleic Acids Res, 2010. **38**(Web Server issue): p. W529-33.
117. Ashkenazy, H., et al., *ConSurf 2016: an improved methodology to estimate and visualize evolutionary conservation in macromolecules.* Nucleic Acids Res, 2016. **44**(W1): p. W344-50.
118. Ben Chorin, A., et al., *ConSurf-DB: An accessible repository for the evolutionary conservation patterns of the majority of PDB proteins.* Protein Sci, 2020. **29**(1): p. 258-267.
119. Cinelli, M.A., et al., *Correction to Phenyl Ether- and Aniline-Containing 2-Aminoquinolines as Potent and Selective Inhibitors of Neuronal Nitric Oxide Synthase.* J Med Chem, 2016. **59**(3): p. 1246.